Graz University of Technology

Institute for Computer Graphics and Vision

Dissertation

SEGMENTATION OF 3D TUBULAR TREE STRUCTURES IN MEDICAL IMAGES

Christian Bauer

Graz, Austria, April 2010

Thesis supervisors

Prof. Dr. Horst Bischof, Graz University of Technology

Assistant Prof. Dr. Reinhard Beichel, The University of Iowa

Aaw! It’s so hard to get to 500 words.

Homer Simpson

Abstract

The segmentation of tubular tree structures like vessel systems in volumetric medical images is of vital interest for many medical applications. However, a diverse set of challenging objectives and problems is related to this task in different application domains. In this work, we develop and evaluate methods to address these issues.

To accomplish the segmentation of heavily branched structures in a robust manner, we propose a generally applicable three-step approach consisting of: (i) a bottom-up identification of tubular structures followed by (ii) a grouping and linkage of these tubular structures into tree structures that are (iii) used as a prior for the actual segmentation. This approach incorporates additional prior knowledge compared to conventional approaches: the individual tubular structures have to be connected with each other and – from a biological perspective – to be supplied. In this way, we achieve a high robustness regarding the structural correctness of the segmentation results.

We develop and investigate novel methods for each of these processing steps addressing the needs of different applications. In particular, we present a novel approach for detection of tubular objects using the Gradient Vector Flow to address limitations of the typically used Gaussian scale space. We propose two methods for grouping and linkage of sets of unconnected tubular structures into tubular tree structures. One enables an extraction of high quality centerlines in regions that deviate significantly from a typical tubular shape, while the other one allows for a separation of interwoven tubular tree structures as well as handling of various kinds of disturbances. To accurately segment the identified tubular structures two methods are developed. One solves the segmentation task in a globally optimal way using graph cuts, while the other one segments according to the edge closest to the centerline.

Based on these methods, different applications for segmentation of blood vessel trees (liver vasculature and coronary arteries) and airway trees in CT datasets are developed. The methods are evaluated on clinical datasets and compared to results achieved with other state-of-the-art methods developed for the same task. The results successfully demonstrate the benefits and strengths of the presented methods and underline the robustness achieved with the outlined three-step approach regarding the structural correctness.

Keywords. medical image analysis, tubular tree structure segmentation, vessel segmentation, airway segmentation, tube detection filter, vessel tree separation, liver vessel segmentation, coronary artery extraction

Kurzfassung

Die Segmentierung tubulärer baumartigen Strukturen wie Gefäßsystemen in volumetrischen medizinischen Bildern ist von wesentlichem Interesse für viele medizinische Anwendungen. Jedoch sind mit dieser Aufgabe verschiedene herausfordernde Zielsetzungen und Probleme in unterschiedlichen Anwendungsbereichen verbunden. In dieser Arbeit entwickeln und evaluieren wir Methoden die diese Punkte adressieren.

Um die Segmentierung solcher stark verzweigten Strukturen auf robuste Art zu bewerkstelligen, schlagen wir einen generell einsetzbaren drei-schrittigen Lösungsansatz vor: (i) Identifizieren tubulärer Strukturen gefolgt von (ii) Gruppieren/Verbinden in baumartige Strukturen die dann (iii) als Vorwissen für die tatsächliche Segmentierung verwendet werden. Gegenüber konventionellen Vorgehensweisen bezieht dieser Ansatz zusätzliches Vorwissen mit ein: Die einzelnen tubulären Strukturen müssen miteinander verbunden sein und – biologisch betrachtet – versorgt werden. Auf diese Weise erzielen wir eine hohe Robustheit im Bezug auf die strukturelle Korrektheit der Segmentierungsergebnisse.

Wir entwickeln und untersuchen Methoden für jeden Verarbeitungsschritt um die Anforderungen verschiedener Anwendungen zu adressieren. Im Besonderen präsentieren wir einen neuen Ansatz für die Detektion von tubulären Objekten mittels Gradienten Vektoren Fluss der Beschränkungen des üblicherweise verwendeten Gauß'schen Größenraumes überwindet. Wir stellen zwei Methoden zum Gruppieren/Verbinden unverbundener tubulären Strukturen auf. Eine erlaubt eine Extraktion qualitativer Mittelachsen in Bereichen die stark von der typischen tubulären Form abweichen, während die andere eine Separierung von ineinander verwobenen baumartigen Strukturen sowie eine Behandlung verschiedener Störungen erlaubt. Um genaue Segmentierungen der identifizierten baumartigen Strukturen zu erhalten werden zwei Methoden entwickelt. Eine löst die Segmentierungsaufgabe auf global optimale Weise mittels Graphenschnitten, während die andere entsprechend der innenliegendsten Kante segmentiert.

Basierend auf diesen Methoden werden unterschiedliche Anwendungen für die Segmentierung von Blutgefäßbäumen (Lebergefäße, Koronararterien) und Bronchialbäumen entwickelt. Die Methoden werden auf klinischen Datensätzen evaluiert und mit den Resultaten anderer anerkannter Methoden verglichen. Die Resultate zeigen erfolgreich die Vorteile und Stärken der präsentierten Methoden und unterstreichen die Robustheit die mit dem skizzierten drei-schrittigen Lösungsansatz erzielt wird.

Schlagwörter. medizinische Bildanalyse, Segmentierung tubulärer baumartiger Strukturen, Gefäßsementierung, Bronchialsegmentierung, Gefäßbaumseparierung, Lebergefäßsegmentierung, Koronararteriensegmentierung

Acknowledgements

I am deeply grateful for the support and encouragement I received from several people throughout all the years I have been working towards my PhD degree. Without their help this work would not have been possible. Here, I finally have the opportunity to thank all these people.

First of all, I want to express my gratitude to my supervisors Horst Bischof and Reinhard Beichel. They awakened my interest in medical image analysis, encouraged me in my research, provided the necessary scientific supervision, and were always available as competent discussion partners. They also enabled an eight month research stay at the University of Iowa where I had the chance to learn a lot professionally, but also about life in general.

I appreciate the good cooperation with all my fellows at the Institute for Computer Graphics and Vision but special thanks for several fruitful discussions go to Tom, Martin, Werner, Rene, Alex, Denis, Bernhard, Judith, and Christian.

For providing datasets, medical knowledge, and supporting evaluations I want to thank Erich Sorantin, Georgios Sarkas, and the organizers of the workshops on “Extraction of Airways from CT” and “Coronary Artery Tracking”. Financially, this work was supported by the Austrian Science Fund (FWF) under Grants P14897-N04, P17066-N04, and the doctoral program “Confluence of Vision and Graphics W1209” and the Austrian Marshall Plan Foundation.

Last but not least, I want to thank my family and my friends. They gave me the mental background necessary to pursue a PhD program. Especially my parents supported me throughout all my studies and encouraged me in working towards a PhD degree. For some distraction and helping me to relax in the evenings I thank my friends Markus, Wolfgang, Angela, and Johannes and – since my stay in Iowa – Simon, Willy, Monika, Karl, and Tim. Finally, I want to express my deep gratitude towards my girlfriend Shuo for her love and her contagious positive attitude towards life.

Deutsche Fassung:
Beschluss der Curricula-Kommission für Bachelor-, Master- und Diplomstudien vom 10.11.2008
Genehmigung des Senates am 1.12.2008

EIDESSTATTLICHE ERKLÄRUNG

Ich erkläre an Eides statt, dass ich die vorliegende Arbeit selbstständig verfasst, andere als die angegebenen Quellen/Hilfsmittel nicht benutzt, und die den benutzten Quellen wörtlich und inhaltlich entnommene Stellen als solche kenntlich gemacht habe.

Graz, am …………………………… ………………………………………………..
(Unterschrift)

Englische Fassung:

STATUTORY DECLARATION

I declare that I have authored this thesis independently, that I have not used other than the declared sources / resources, and that I have explicitly marked all material which has been quoted either literally or by content from the used sources.

…………………………… ………………………………………………..
date (signature)

Contents

List of Figures

List of Tables

Chapter 1

Introduction

Contents

Blood vessels and airway trees of the human body from dense tubular networks. They form tubular structures – elongated objects with an approximately circular cross section – that branch recursively. During branching the radius of the tubular structures steadily decreases, such that as a result they form tubular tree structures as those shown in Fig. 1.1.

With modern medical imaging techniques like (contrast enhanced) CT, MR, or 3D ultrasound, tubular tree structures can be depicted in great detail. Their identification and description in volumetric datasets is of vital interest for a variety of clinical applications as their analysis facilitates diagnosis, quantification, and monitoring of disease. The derived models are also utilized for visualization, interaction, registration, surgery planning, or simulation tasks such a blood flow simulation or training of surgery. However, deriving this information manually from datasets is infeasible in clinical practice due to their complexity and the required time effort. Doing it manually would additionally introduce observer variability that should be avoided. Therefore, automated and robust segmentation methods for these kinds of tasks are needed.

In this work, we deal with the segmentation of such tubular tree structures in volumetric medical datasets. The remainder of this chapter is structured as follows: In Section 1.0.1 we give an overview about general requirements and problems for such methods, in Section 1.0.2 we give an overview about representations utilized to describe tubular tree

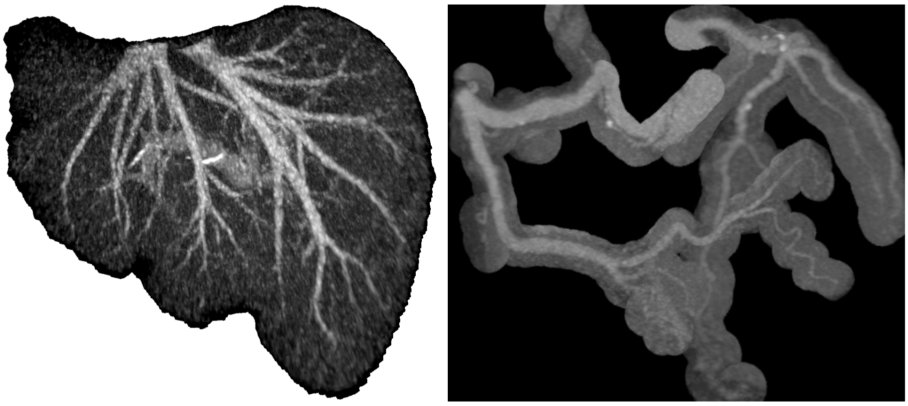

(a) Portal and hepatic vein trees of the liver.

(b) Coronary artery trees.

(c) Aorta.

(d) Airway tree.

(e) Lung vessels.

Figure 1.1: Examples of tubular tree structures in medical images.

structures, and in Section 1.0.3 we discuss issues related to the evaluation of tubular tree structure segmentation methods. In Section 1.1 we discuss related work that is concerned with similar objectives, in Section 1.2 we introduce a general concept for segmentation of tubular tree structures that forms the basis of this work, and in Section 1.3 we outline the main objectives and the organization of the rest of the work.

As a general remark, throughout this work we will use the terms blood vessel (tree), airway (tree), or more generally tubular (tree) structure interchangeably where appropriate to refer to the corresponding structure as all of them show very similar characteristic properties in the underlying images.

1.0.1 Requirements and Problems

The segmentation of tubular tree structures in medical datasets is a challenging problem. Not only acquisition-dependent parameters such as contrast, resolution, and imaging artifacts have to be considered, but in particular their complex structure and the potential small size of vessels/airways is problematic for segmentation methods. For the segmentation tasks, the requirements may vary for different applications regarding the type of extracted information, accuracy requirements, and the degree of automation. This has to be outlined for each application individually. However, a set of general requirements can be identified that typically have to be addresses by the methods in order to be clinically applicable:

- Deliver correct 3D reconstructions of the tubular tree structures in a volume of interest.
- Have the ability to segment thin tubular structures with low contrast.
- Differentiate tubular tree structures from other adjacent structures with the same gray values such as tumors or other tubular tree structures.
- Robustly handle cases where parts of the tubular tree structure are disturbed; e.g. due to imaging artifacts such as motion artifacts or beam hardening or due to disease such as tumors, calcifications, aneurysms, or stenosis where the appearance and geometry of the tubular structures is disturbed.
- Require only minimal or no user interaction.

1.0.2 Representations

Depending on the application, different informations can be of interest. Consequently, different kinds of descriptions/models at different abstraction levels are used for their representation. We distinguish between volume/surface-based representations of the segmentations, skeleton-based representations, and graph-based representations that can be utilized to describe the tubular tree structure. The different representations are illustrated in Fig. 1.2.

Volume/surface-based representations: The classical segmentation task is to assign each voxel of an image a label (object/background) describing its membership with a targeted object – a tubular tree structures in our case. Such segmentations represent

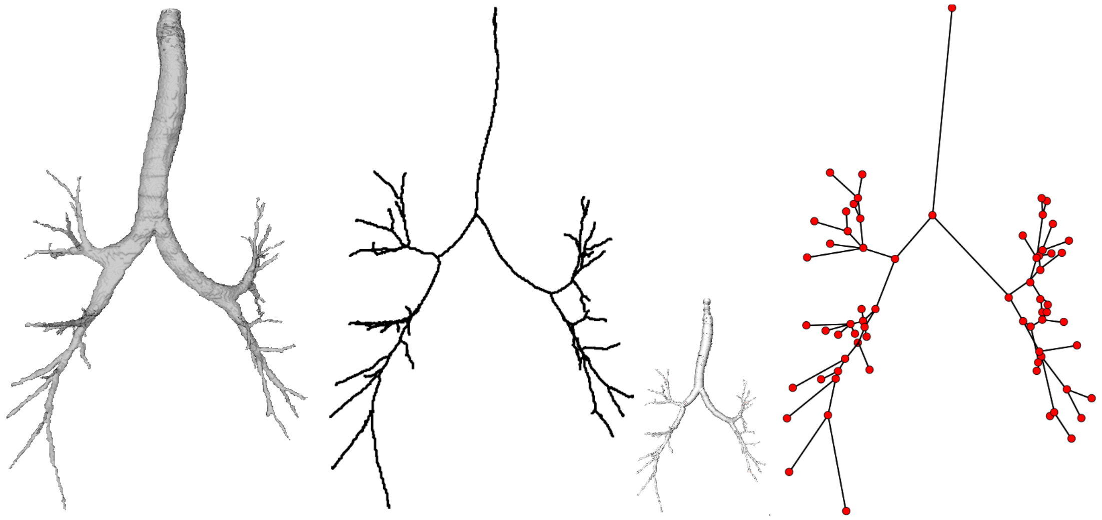

(a) Volume/surface-based representation describing surface.

(b) Curve skeleton describing structure (bottom right: with additional radius information).

(c) Graph-based structure representing topology.

Figure 1.2: Representations of tubular tree structures.

the surfaces of the tubular tree structures in an implicit way. The surfaces may also be represented explicitly using mesh representations for example. These volume or surface-based segmentations (Fig. 1.2(a)) allow for an accurate detailed representation of the targeted structure and its delineation from the background. In addition, they represent the most suitable representation for visualization purposes. However, with tubular tree structures often structural properties are of interest that are not well described with this kind of representations.

Skeleton-based representations: From a structural point of view, a tubular tree structure can be partitioned into individual branches that are connected at branch points. The structure of each of the branches may be roughly described by its centerline, while the centerlines of all branches together form a curve skeleton. Such centerlines/curve skeletons (Fig. 1.2(b)) are of primary interest for a variety of applications as they cover the structure of the the individual branches/the whole tubular tree structure well. Often additional information is assigned to each of the centerline points such as its tangent-direction or radius. Such an enriched representation may also be considered as a rough segmentation.

Graph-based representations: On an even higher level of abstraction, the skeleton can be represented as a graph-based structure (Fig. 1.2(c)), where each branch point or endpoint of the skeleton is represented as a node and the centerlines of the branches in between are represented as links between the branch points/endpoints. Such a representation captures the topology of the tubular tree structure – the connectivity information between the individual branches – well. This provides information about the child-parent relationship of the individual branches that encodes how each each vessel is supplied.

Of course the different kinds of representations are closely related to each other. Starting from a valid segmentation the other representations may be derived quite easily, using a skeletonization method to obtain the curve skeletons that can then be transformed into a graph-based representation. Note, that there are also other possibilities to extract the structural information directly from the datasets without the need to produce valid segmentations first as described later in this work.

1.0.3 Evaluation Issues

The evaluation of tubular tree structure segmentation methods is a difficult problem due to the complex topology of tubular systems (e.g. blood vessel trees).

Structure vs. accuracy: When evaluating tubular tree structure segmentation methods, structural properties have to be considered. These properties are not well captured with conventional segmentation performance measures such as average surface distance or volumetric error measures that target only segmentation accuracy aspects. An example illustrates this in Fig. 1.3 where three different segmentations with a comparable surface distance error are shown. While in case of Fig. 1.3(a) the surface is inaccurate, the reason in Fig. 1.3(b) and (c) are related to structural errors (missing branch, unconnected tubes). For evaluation one has to distinguish between structural correctness and surface/centerline accuracy. For assessment of structural correctness one has to investigate, whether all branches are correctly identified and correctly connected with each other. And only for those tubes with a correct structure, valid statements about the accuracy of their associated surface/centerline can be made.

Reference segmentations: Usually, reference segmentations are generated and utilized for evaluation of segmentation methods, but with complex interwoven tubular tree structures this is very time consuming as shown by some examples known from the literature

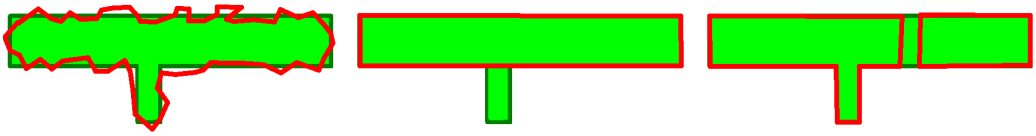

(a) Inaccurate surface. (b) Missing tube branch. (c) Unconnected tubes.

Figure 1.3: Various segmentations with comparable surface distance/volume error due to different reasons, showing the reference segmentation (green) and different segmentation results (red).

[88, 124]. Schaap et al. [124] annotated in 32 coronary datasets the centerlines of 4 arteries, which took three observers all together approximately 300 hours of work. Lo et al. [88] spend about 750 hours to obtain references of airway trees in 20 chest CT datasets using a semi-automated approach that only focused on structural correctness of the segmentation results, but not on surface accuracy aspects. In some application domains such as liver vasculature segmentation/separation or lung vessel segmentation/separation even more tubular structures must be identified and additionally a separation of multiple interwoven tubular tree structures is required, making it practically infeasible to produce reference segmentations in such application domains.

1.1 Related Work

Due to the importance of tubular structure segmentations, difficulties related to this task, as well as varying application requirements, many publications dealing with this problem can be found in the literature. Extensive surveys of existing vessel segmentation techniques can be found in the review of Kirbas and Queck [62] as well as in the recent work of Lesage et al. [79] who provide an excellent overview and classification of the techniques. For an overview of methods for extraction of airways from CT datasets we refer to the work of Sluimer et al. [132], while more recent approaches are described in Lo et al. [88].

Because of the large number of methods published, we refrain from highly detailed discussions of all approaches and refer to the above mentioned review papers. Instead, we provide a brief summary of related vessel/airway segmentation techniques following closely the classification and work of Lesage et al. [79]. In the following, we discuss some general aspects of these methods when applied to heavily branched tubular tree structures, and present the concept of vessel mining. Publications more closely related to parts of our work are discussed in appropriate chapters later in this work.

1.1.1 Models, Features, and Extraction Schemes

Lesage et al. [79] provide an excellent and up-to-date overview and classification of 3D vessel segmentation techniques that is also valid for airway segmentation techniques. The different methods known from the literature utilize many different image processing frameworks. In [79] the authors distinguish between three main characteristics of vessel segmentation techniques: models, features, and extraction schemes.

Models: Models are used to represent prior knowledge about the target vessel structures. In this context, one may distinguish between photometric and geometric properties of the vessels. Methods utilizing pure photometric models make assumptions about the expected luminance [1, 40, 117, 175] of the vessels and/or the background [40, 52, 93, 125, 126] as well as the image noise [52, 148] to distinguish between vessel structures and non-vessel structures. Methods utilizing geometric models make assumptions about a key characteristic of vessels, namely their specific shape. Therefore, the methods may encode information about their elongation, properties of their centerline [15, 42, 72], and/or their cross-section [26, 27, 42, 43, 150]. Photometric and geometric information are often combined into hybrid models, incorporating assumptions about the spatial appearance of vessels such as Gaussian- or bar-like cross section profiles [64, 70, 135, 166], appearance as a ridge in scale space [2, 12, 45], or template-based approaches [44, 48, 83]. The models typically focus solely on regular vessel segments, while models about bifurcations or anomalies can only be found rarely, although exceptions – typically adapted to specific kinds of disease – can be found [1, 42, 83, 159, 162].

As a general note, these models are often embedded implicitly in the features and extraction schemes discussed below.

Features: Features are the actual detectors/filters used to evaluate a vascular model on the image data. Therefor the methods utilize information about the basic image intensity, first order, and/or second order image derivatives to match against the expected model, often embedded in a Gaussian scale-space framework [84, 143] to account for tubular structures of varying size. Features used in the literature are isotropic features where no assumption about the directionality of the vessel is made [3, 74, 75, 138], features making use of the local geometry typically based on derivative features [1, 44, 73, 83, 89, 121] or model fitting [48, 72, 148, 166] with few other techniques. Another approach is utilizing features based on 2D cross-sectional measurements that require the orientation as an input parameter [2, 40, 41, 46, 64, 141, 162]. Similarly as with the different models, bifurcations or anomalies are often not considered explicitly. However, exceptions – typically adapted to specific diseases – can be found in [1, 45, 83].

Extraction Schemes: The extraction scheme represents the actual segmentation algorithm – they are based on the model assumptions and are guided by the extracted features. Lesage et al. [79] classify methods known from the literature into three general classes of extraction schemes as well as pre- and post-processing techniques.

For pre-processing, several vessel-specific methods can be found in the literature. Several of the features described above were originally presented as vessel enhancement filters [1, 44, 64, 70, 83, 121], while similar formulations may be incorporated into vessel-dedicated anisotropic diffusion schemes [66, 94, 140]. Other typical pre-processing tasks involve the generation of pre-segmentations such as generation of regions of interest based on prior knowledge [39, 111, 131] or based on thresholded potential maps derived from probability maps from appearance models or from vessel enhanced images [1, 23, 161, 167, 170]. To select sparse sets of vessel-candidate points robust maxima [138] or local maxima are used [39, 75].

For the actual extraction scheme one may distinguish between region-growing algorithms, active-contour based methods, and centerline based approaches. Region-growing or wave-propagation methods start from a seed point or region inside the vessel and merge neighboring voxels in a greedy way using various merging criteria [14, 19, 62, 117, 175]. More advanced techniques of this category adapt parameters during growing or analyze the local segmentation results to avoid segmentation errors [62, 93, 101, 117, 146, 175]. Active-contour based methods evolve an interface following external data-driven and internal model-driven forces, using explicit (classical snakes) [28, 42, 59, 96, 103] or implicit representations (level-sets) [60, 61, 90, 91, 106]. Within this category several vessel-specific adaptions have been presented in the literature to handle the complex topology of vascular systems (topology-adaptive snakes) [97, 98], to incorporate vessel-specific features exploiting the vessels direction (eigen-snakes, curves) [90, 144, 145], or they are based on curvature-based regularization [60, 155, 169]. The last category of extraction schemes are centerline based approaches, that in contrast to the other methods do not focus on detecting the vessels contour using pixel-wise criteria, but on extraction of the vessels centerlines directly from the image data. Therefore, direct centerline tracking methods [1, 2, 42, 45, 48, 141] have been presented that track starting from a seed along a vessel by iterative prediction and correction steps; increased robustness can be achieved by explicitly embedding geometric models into the tracking process. Another class of centerline based extraction methods is based on minimal path techniques with cost metrics related to some vessel-dedicated features [42, 51, 83, 163] or closely related formulations based on fuzzy connectedness [149] or ordered region-growing [21, 173]. These minimal-path techniques have issues like eccentric or even erroneous "shortcut" paths [81, 82]; However, this problem has been addressed in [82] by introducing an additional dimension corresponding to the vessel radius [82, 163]. A few stochastic frameworks have been introduced in the literature to increase the robustness of such extraction schemes [41, 78, 126] to the cost of a much higher computational effort. Only the multi-hypothesis tracking presented in [47, 48] is practically applicable.

Post-processing techniques address issues regarding missing or inaccurate surface information or topological considerations. To obtain/refine surface segmentations in case of a known centerline a few methods have been presented in the literature by segmenting either slice-by-slice in the 2D-cross sections [107, 108] or directly in 3D [42, 152, 165]. Another typical post-processing step is the other way around – obtaining centerlines/skeletons in case of given segmentations using a skeletonization method. Skeletonization has been addressed based on homotopic thinning [92, 109, 110] or distance transformations [101, 115, 116]. Gradient flux maximization [15, 16] or the use of minimal-path techniques [53, 54] are more recent approaches. As segmentations of vascular trees may be topologically erroneous, a few techniques have been presented to correct such errors. In case of isolated false positives/negatives or noisy contours, mathematical morphology [1, 156, 167] or formulations based on Markov random field techniques [23, 164] have been used. In case of leakage, competitive region growing [171], a hierarchical segmentation scheme [61], and fuzzy connectedness [77, 149] have been utilized to remove these areas. To clean up and reconnect segmentations a few methods have been proposed using graph based techniques (typically minimum spanning tree algorithms [39, 58, 118]) that exploit the intrinsic nature of tree structures [1, 75, 138, 173].

In practice, it is crucial to combine the appropriate models, features, and extraction schemes for specific task at hand. In particular, incorporation "of a priori knowledge on the geometry and appearance of the target vessel is crutial to the robustness and accuracy of a segmentation method" [79].

1.1.2 Discussion

The above presented techniques address the segmentation of vascular/airway structures in general, and not necessarily whole tubular tree structures. Considering these techniques with respect to the requirements and problems we aim at addressing in this work (Section 1.0.1), one gains insight into the challenges of this problem.

Identifying an appropriate vessel/airway model that is valid in all possible cases is a non-trivial task, in particular when one considers pathology like stonsis/aneurysms/calcifications or simple bifurcations where the appearance and/or geometry of the tubular structures is disturbed. Also cases of local disturbances such as imaging/motion artifacts or partly overlapping image structures with the same gray-value (e.g. adjacent tumors or multiple partly overlapping vessel trees) are difficult to model. For these reasons, it seems illusory to identify a model that is valid in all cases.

This becomes a problem when combined with the discussed extraction schemes. While the pre-processing methods are typically applied voxel-wise, an inadequate model leads to fragmented outputs, with false positive and false negative detections. The presented extraction schemes (region-growing, active-contour, and centerline-tracking methods) all require appropriate initializations and basically merge neighboring voxels or extend a known centerline according to the model. In case of conservative model assumptions this easily leads to premature termination of the (iterative) extension process, while in case of weak model assumptions the methods are prone to leakage. Methods based on minimal path-techniques show a higher robustness against such local failures of an inadequate model. However, they require appropriate start- and end-points for each vessel. For heavily branched tubular tree structures this is a practically infeasible task.

In case of failure, the segmentation errors (under/over segmentation) that result from local model-inadequateness may have a strong influence on the resulting structure/topology of the segmented tubular trees. This is problematic, since the structural information is of vital interest for several applications (Section 1.0.1).

1.1.3 Vessel Mining

To address some of the problems mentioned above, Beichel et al. [10] proposed a concept to enhance the robustness of vessel segmentation approaches against local disturbances. The idea behind the concept that they termed “vessel mining” is: “first identify all potential tubular structures in the search volume and then reconnect the found tube structures based on defined criteria like for example gray-value evidence” [10]. This approach was designed to avoid leakage into other structures and increase the robustness in cases of noise or anisotropic voxel size, compared to simpler methods like region growing. Beichel et al. presented a system based on this concept for liver portal vein tree segmentation that has been applied to a phantom dataset and to one routinely acquired liver CT dataset. A comparison to a simple region grower showed the increased robustness of their system. In later work of the same group [113, 114], the authors focused on refining parts of the approach for their main application – liver portal vein tree segmentation – where they improved the methods ability to identify vascular structures and where they increased the accuracy of the segmented vessel walls by utilizing the identified vascular structures as initialization of an intrinsic segmentation.

The general approach for segmentation of branched tubular networks as described in the next section is based on these seminal ideas of "vessel mining" as proposed by Beichel et al. [10, 113].

1.2 A General Approach for Segmentation of Branched Tubular Networks

3D tubular tree structures form sets of tubular structures that are connected with each other. Each of the tubular parts has its structure and surface delineating it from the background. To segment all kinds of branched tubular networks, the following general approach can be use (Fig. 1.4):

1. **Extraction of tubular structures:** Identify all tubular structures in a volume of interest and generate a structural representation for all of them. The resulting centerline-based representations describe already major parts of the branched tubular network, but they describe only the parts following the tube model, while in the branched tubular network parts may still be missing where the appearance strongly deviates from a typical tubular shape. This may be in case of branching areas, due to other cases where the shape of the vessels is severely perturbed such as stenosis, aneurysms, or tumors, due to other structures with similar gray in the image domain, or due to imaging artifacts.

2. **Grouping and linkage into connected networks:** Group the tubular structures belonging to the same tubular tree and link them together recovering the structures of the different branched tubular networks. The individual tubular structures of

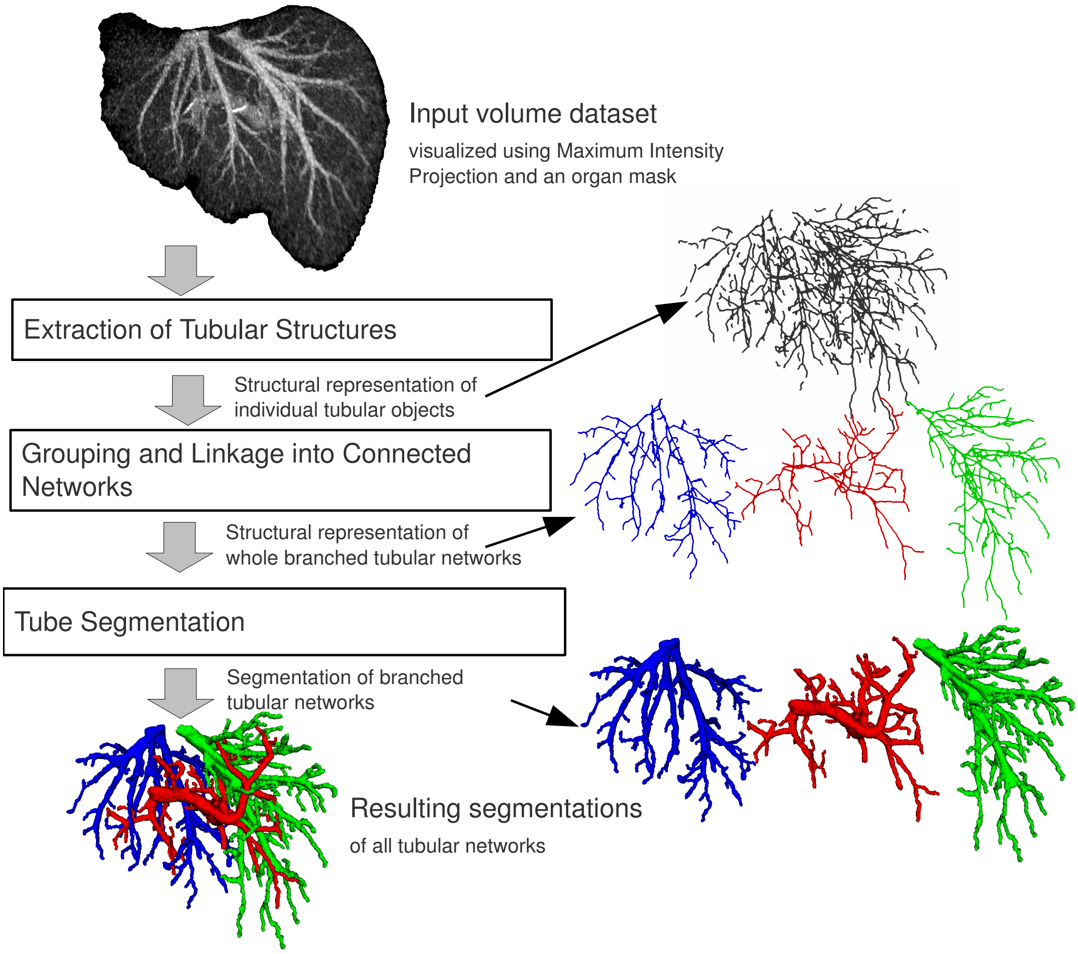

Figure 1.4: General concept for segmentation of branched tubular networks.

a branched tubular network are interconnected and from a biological perspective they have to be supplied somehow. Utilizing this fact, the structures of the whole branched tubular networks is recovered also in the disturbed regions. The resulting skeleton-based representations describe the complete structure of the branched tubular structures, but not their surface.

3. **Tube segmentation:** Segment the branched tubular networks utilizing their already know structures as prior knowledge. During this step the surfaces of the branched tubular networks are obtained and accurately delineated from the background.

With this approach we seek for a higher robustness to shortcoming of the tube model or disturbances compared to conventional extraction schemes as discussed in

Section 1.1.2. “Practically all currently used vessel [tubular tree structure] segmentation methods are based on a growth process emanating from an automatically- or user-defined start point” [47], which results in the problem that in case of larger deviations from the tube model or disturbances major parts of the tree structure may remain unidentified (Section 1.1.2). Contrary to that, with our approach initially tubular structures are identified in a bottom-up fashion such that also in cases where the assumptions of the tube model do not hold still major parts of the tree structure are identified. This information can be utilized in the following processing steps. Additionally, we incorporate the prior knowledge that the individual tubular structures of a branched tubular network are interconnected. This combination allows resolving cases, where typical assumptions of a vessel/airway model may be inadequate, such that the structure of the tubular tree structures can be obtained correctly and later on used for a more accurate segmentation.

The outlined approach is of general applicability. It has a strong focus on the structural correctness of the segmentation results, which is of importance for most applications dealing with tubular tree structure. In addition, handling of different kinds of disturbances is considered directly as part the approach. However, it is only an approach and not a specific method. It does not specify how to detect tubular structures, how to group and link them together, or how to utilize the so obtained information for the actual segmentation. And indeed, this may vary from application to application depending on its requirements.

Also, depending of the application's requirements, only parts of this approach may be necessary, e.g. in case only the structural information is of importance but not accurate segmentations, step three – the tube segmentation – can be skipped. But all typical requirements and representations needed in different applications are covered with this approach.

1.3 Overview and Contributions of the Work

In this work, we develop and evaluate methods for the segmentation of 3D tubular tree structures in medical images. The goal is to address the outlined requirements and problems found in different clinical applications and to provide suitable solutions. Thereby, we follow the proposed general concept for segmentation of tubular tree structures as outlined in the last section. We present several original contributions that resulted from the research on this topic and that have also been presented in several publications [4–9, 105, 119, 124]. A list of these publications can also be found in Appendix A.

The work is roughly organized in two parts, a general methods part and an applications part:

Methods: In the methods part, we are dealing with the development and evaluation of suitable methods for the individual building blocks of the proposed general approach [9] (Section 1.2) that forms the basis of our work. Depending on the applications, the requirements for the these building blocks may vary and therefore different methods for each building block are presented. The methods are compared to each other and properties of the different methods are analyzed.

In Chapter 2 we first review different methods for the detection/extraction of tubular structures from volumetric medical images known from the literature. We highlight a core problem of conventional tube detection approaches that is related with the utilized Gaussian scale space – diffusion of nearly image structures on larger scales – which may lead to false responses. To overcome this problem, we introduce a novel approach for detection of tubular objects [6] (Section 2.3) to address this issue by replacing the conventional multi-scale gradient vector computation by the Gradient Vector Flow (GVF) [168]. As shown in our experiments, this approach proofs to be beneficial in case of surface patches or other nearby image structures. Additionally, the method has the ability to cope with varying background conditions, an issue that can not be addressed using conventional Gaussian scale space based methods. This makes the presented GVF-based approach also applicable in areas where the utilization of tube detection filters has not been considered so far. Further, we present an efficient height ridge traversal for extraction of the tubular structures from the tube detection filter responses (Section 2.4).

In Chapter 3 we introduce two novel methods for grouping and linking identified tubular structures into complete tree structures. The first method [9] (Section 3.2) is based on structural properties of the identified tubular structures and enables a separation of interwoven tubular tree structures and handling of various kinds of disturbances – objectives that are typically not addressed in this level. The second method [5] (Section 3.3) utilizes properties of the GVF and enables an extraction of centered linkage paths in areas where the shape of the structures deviate strongly from a typical tubular shape such as stenosis, aneurysms, or branching areas. This allows extraction of high quality curve skeletons directly from the the gray scale image with an accuracy comparable to sophisticated skeletonization methods, what supersedes the need to deal with a segmentation problem and a skeletonization problem.

In Chapter 4 we present two novel methods for the segmentation of tubular objects associated with known tubular structures. Both aim at preserving the topology of the already known tubular tree structures. The first method [7] (Section 4.2) utilizes the same GVF field that can also be utilized for detection of tubular objects (Section 2.3). It performs the segmentation according to the first distinct edge closest to the centerline. The second method [9] (Section 4.3) on the other hand utilizes the obtained information as a shape prior and solves the segmentation task in a globally optimal manner using a Graph Cut algorithm. This makes the approach robust to various kinds of disturbances.

The presented set of methods allows building various applications for the segmentation of 3D tubular tree structures with different requirements.

Applications: In the applications part, we develop novel methods for specific application domains based on the proposed general approach for segmentation of tubular tree structures and the presented methods for the individual building blocks. The objectives and problems that are addressed in these application areas are very diverse and challenging. We evaluate the methods on clinical datasets with various kinds of disturbances and compare them to other state of the art methods with the same objectives.

In Chapter 5 we present a method for segmentation and separation of liver vascular trees in contrast CT datasets for surgery planning [9]. The method is evaluated on CT scans of a plastic phantom and clinical datasets based on the assessment by an experienced radiologist. The results show a high robustness of our approach against disturbances, the methods ability to successfully reconstruct, separate, and accurately segment multiple interwoven tubular tree structures in this application domain.

In Chapter 6 we present an automated method for extraction of the coronary artery trees centerlines in contrast CT datasets [4]. The method is evaluated on a publicly available database [124] and compared to other methods for this task. Compared with the other methods that have been evaluated on this database, only methods that utilized information about the endpoint of the coronary arteries – information not available in practice – performed better with respect to the extraction capability.

In Chapter 7 we present two automated methods for the extraction of airway trees from CT datasets. The two developed methods show different advantages [7, 8]. The first method (Section 7.2.1) produces immediately accurate segmentations and allows for an additional extraction of the associated curve skeleton in a straight forward manner. The second method (Section 7.2.2) allows handling of local disturbances and shows a higher robustness in case of disease. Both approaches are evaluated on a publicly available database [88] and compared to other methods for this task. Both methods perform about comparably well in practice, and are among the best performing methods known in the literature. Only one other method evaluated on the public database allows for an extraction of more airway branches while having a lower leakage volume, however to the cost of about one hour of manual user interaction.

Conclusion: Finally, in Chapter 8 conclusions are presented. We summarize the results achieved on the different applications and analyze the usefulness, general applicability, and advantages of the individual developed methods. The results successfully demonstrate the benefits and strengths of the presented methods and approaches, including the robustness achieved with our proposed general approach for segmentation of tubular tree structures as outlined in Section 1.2.

With our proposed general approach [9] we are seeking for a higher robustness regarding the structural correctness of the segmentation results compared to conventional approaches as these are prone to possible shortcomings of the utilized vessel/airway models as discussed in Section 1.1.2. To achieve this, we consider handling of different kinds of disturbances directly as part of the approach by combining an initial bottom-up extraction of tubular structures with a grouping and linkage step. This allows resolving cases where typical vessel/airway models are inadequate, such that the structure of the tubular tree structures can be obtained correctly and later on used for a more accurate segmentation. By comparing the results achieved with our methods – that are all based on the proposed general approach – to the results of other methods in the different applications, we conclude that this approach leads to a high robustness compared to conventional approaches. This conclusion can also be considered as one of the main contributions of the overall work.

Chapter 2

Extraction of Tubular Structures

Contents

2.1 Introduction

A tubular tree structure can be described as a set of tubular structures that are interconnected with each other such that there are no loops. In this chapter, we are concerned with the extraction of these tubular structures in medical images. Thereby, we aim at deriving structural representations for all tubular structures in a given volume of interest in a fully automated fashion.

In the literature, methods have been presented that enable extraction of structural representations (centerlines) of tubular structures directly from the gray-value images [2, 163]. However, these methods require an appropriate initialization for each single tubular structure. In contrast to these methods, tube detection filters (TDF) – a.k.a. vessel detection filters, lineness filters, or vessel enhancement filters (e.g. [44, 70, 123]) – do not require such an initialization, because they perform a shape analysis for each voxel in the image domain resulting in a kind of medialness measure or tube-likeliness. However, TDFs do not result in structural representations of the tubular objects. To extract such structural representations from TDF responses, a combination of hysteresis thresholding and local directional non-maximum suppression was used by Krissian et al. [68] while Steger et al. [135] utilized an efficient ridge tracking approach for processing 2D images. Therefore, to achieve the objectives for our fully autonomous bottom-up identification and extraction of tubular objects, the combination of a TDF with a centerline extraction based on a ridge traversal is the appropriate choice.

In the next sections, we review different TDFs known from the literature (Section 2.2), develop a novel approach for detection of tubular objects (Section 2.3), and present a 3D ridge traversal for extraction of structural representation from TDF responses (Section 2.4). In Section 2.5, the methods will be evaluated and compared with each other. Some well known TDFs are presented in more detail for two reasons. First, some of their ideas are utilized in the later part of this chapter where the novel TDF approach is developed. Second, some of the presented TDF methods are used in the applications part of this work.

2.2 Tube Detection Filters in Gaussian Scale Space

Most TDFs presented in the literature like [11, 44, 70, 89, 114, 123] are based on the assumption that the tubular objects can be specified by their local geometry and that they form bright structures surrounded by a darker homogeneous background. The radius of these structures varies, but using the concepts of scale-space theory [85], the tubular structures form height-ridges in the Gaussian scale space when the scale is adapted properly to the size of the objects. Based on these assumptions, conventional TDFs try to identify the tubular objects at different scales in the Gaussian scale space and combine all scale dependent responses into one multi-scale response. The response on a single scale is obtained by convolution of the initial image with a tube-likeliness function function $T^{\sigma}(\mathbf{x})$, where $\mathbf{x}$ is a point in 3D space and σ denotes the radius dependent scale of the measurement. In the literature also the terms vesselness or medialness function are utilized as it is related to medial axes. These single scale responses are obtained at various scales and combined into one multi-scale response $T(x)$ by selecting the maximum response over the range of all scales between σ_{min} and σ_{max}:

$$T(\mathbf{x}) = \max_{\sigma_{min} \leq \sigma \leq \sigma_{max}} \{T^{\sigma}(\mathbf{x})\} \quad . \tag{2.1}$$

The maximal response over all scales further indicates the associated radius r and tangent direction t of the tube.

The different tube detection methods presented in the literature differ from each other in the way the tube-likeliness measures are obtained on the different scales. Many approaches use the first order derivatives (gradient vectors), or second order derivatives (Hessian matrix), or a combination of both to identify the tubular objects at a specific scale. All of them use – directly or indirectly – properties of the gradient vector field. The reason is that tubular objects show characteristic gradient vector fields which can be used for detection. One such example is shown in Fig. 2.1. For a tubular object, all the gradient vectors point directly towards the centerline of the tube. At the centerlines of the tubular objects, the local vector field shows a large variance in two dimensions (the tubes cross section), and a low variance in the third dimension (the tubes tangent direction). The gradients magnitude is large at the tubes surface and decreases with increasing distance from the surface. Based on these properties, the different methods try to identify tubular structures.

In the following subsections we present three well known tube detection filters/vessel enhancement filters using different assumptions. The purpose of this study is to present the utilized assumptions and to investigate their behavior as well as their possibilities and limitations. Roughly, the medialness functions can be classified into central medialness functions and offset medialness functions. Central medialness functions only consider information at the center of the voxel for classification, while offset medialness functions also incorporate information away from the tubes center at a distance that is related to the tubes size. We follow this classification and present methods falling in each of these categories.

To make use of a common notation, we utilize following terms: I corresponds to the original image, $I^\sigma = G_\sigma \star I$ corresponds to the original image at scale σ, and $\mathcal{B}^\sigma(\mathbf{x}) = \sigma \nabla I^\sigma(\mathbf{x})$ and $\mathcal{H}^\sigma(\mathbf{x}) = \sigma^2 \left[\frac{\partial^2 I^\sigma(\mathbf{x})}{\partial_{x_i} \partial_{x_j}}\right]$ represent the normalized first and second order derivatives at location $\mathbf{x}$ at a given scale, respectively. The normalization is of importance to ensure invariance under scale [85].

2.2.1 Central Medialness Functions

Central medialness functions obtain a tube-likeliness measure considering only the information at the center of the voxel. Therefor, frequently the eigenvalues of the Hessian matrix are utilized. The Hessian matrix with it's associated eigenvalues $|e_1| \geq |e2| \geq |e_3|$

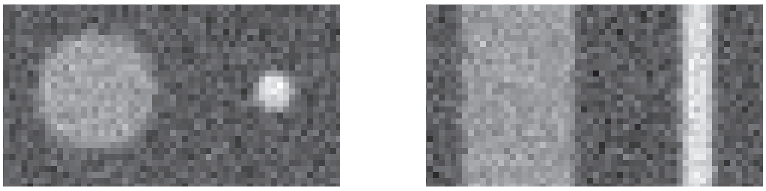

(a) Original image showing 2D cross sections of 3D tubular structures. Left: Cross section orthogonal to tubes tangent direction. Right: Cross section along the tubes tangent direction.

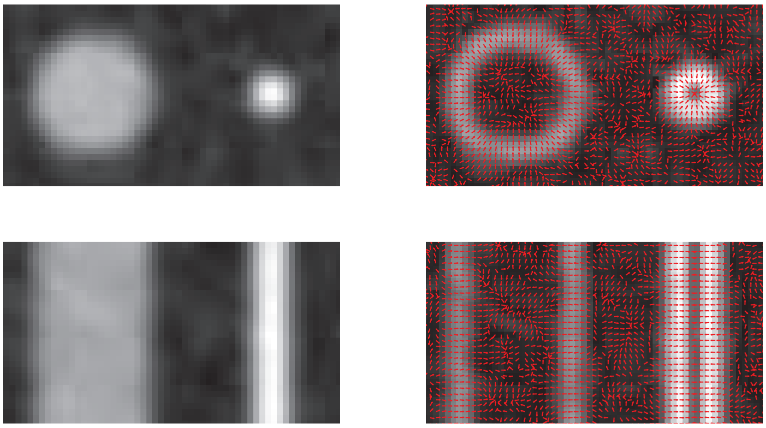

(b) Filtered image and corresponding gradient vectors (vector: direction, grayvalue: magnitude) on a small scale.

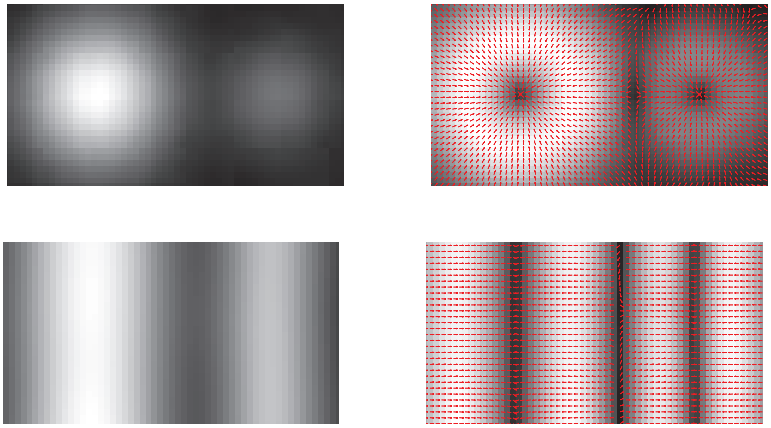

(c) Filtered image and corresponding gradient vectors (vector: direction, grayvalue: magnitude) on a large scale.

Figure 2.1: Tubular structures and derived gradient vectors in Gaussian scale space.

and eigenvectors $\mathbf{v}_1$, $\mathbf{v}_2$, and $\mathbf{v}_3$, encode information about the basic shape of image structures (blob, tube, or plane) as well as the polarity of the structures (brighter or darker than the surrounding). Based on this information, bright tubular structures can be identified as they require their two larger eigenvalues to be negative $e_1 < 0$ and $e_2 < 0$ and the third eigenvalue e_3 being close to zero. For those structures, the tangent direction is then indicated by $\mathbf{v}_3$.

Frangi et al. [44]: One method based on the eigenvalues of the Hessian matrix that has been utilized extensively in practice due to it's simple geometric interpretation is the method of Frangi et al. [44]:

$$T(\mathbf{x}) = \begin{cases} 0 & \text{if } e_1 > 0 \text{ or } e_2 > 0 \\ \big(1 - exp\big(-\frac{R_A^2}{2\alpha^2}\big)\big) exp\big(-\frac{R_B^2}{2\beta^2}\big)\big(1 - exp\big(-\frac{S^2}{2c^2}\big)\big) & otherwise \end{cases} \tag{2.2}$$

with $R_A = |e_3|/\sqrt{|e_1||e_2|}$ indicating blob-like structures, $R_B = |e_2|/|e_1|$ to distinguish between plate-like and line-like structures, and $S = \sqrt{e_1^2 + e_2^2 + e_3^2}$ for suppression of random noise effects. The parameters α, β, and c allow controlling the weighting of the measures R_A, R_B, and S, respectively. Frangi's suggested default values are $\alpha = 0.5$ and $\beta = 0.5$, while c depends on the expected contrast and setting it to half the value of the maximum Hessian norm in the image is suggested.

2.2.2 Offset Medialness Functions

Offset medialness functions incorporate information away from the tubes center at a distance that is related to the tubes size. It was shown by Krissian et al. [70] that such offset medialness functions allow for a greater robustness compared to central medialness functions. Krissian's approach utilizes the Hessian matrix solely for pre-selection of candidate tube points and to determine the tubes cross-section plane, while in a second step boundariness information b_i along a circle in this plane is sampled and combined into the actual tube-likeliness response as illustrated in Fig. 2.2. Considering the Hessian matrix, the eigenvectors associated with the two smaller eigenvalues provide estimates about the tubes cross-section plane spanned by the eigenvectors $\mathbf{v}_1$ and $\mathbf{v}_2$ as well as it's tangent direction given by $\mathbf{v}_3$.

In the following, we present two approaches based on this idea of estimating the tubes cross section plane using the Hessian matrix and afterwards sampling along the expected surface in this plane; the TDFs of Krissian et al. [70] and Pock et al. [9, 114].

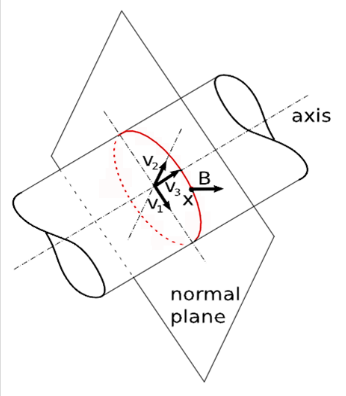

Figure 2.2: Cross-section plane spanned by eigenvectors $\mathbf{v}_1$ and $\mathbf{v}_2$ of the Hessian matrix and sampling of boundary information along a circle (red) in this plane.

Krissian et al. [70]: Krissian's TDF response $T^{\sigma_K}_{Krissian}(\mathbf{x})$ is obtained by averaging the individual boundariness samples $T^{\sigma_K}_{Krissian}(\mathbf{x}) = \frac{1}{N}\sum_{i=0}^{N-1} b_i$ that are computed at $N = \lfloor 2\pi r + 1 \rfloor$ discrete points with varying angle $\alpha_i = (2\pi i)/N$. The individual boundariness samples b_i measure the contribution of the boundary information in the radial direction of the circle $b_i = B(\mathbf{x} + \tau\sigma_K \mathbf{v}_{\alpha_i})\mathbf{v}_{\alpha_i}$, such that a matching with the expected tubular model is performed. One of the main contributions of Krissian et al. [70] was to derive mathematically the optimal relation between the radius r of the tube, the radius $\tau\sigma_K$ of the offset medialness function, and the scale σ_K to use for computation of the Hessian matrix and the boundary information, such that under the assumption of a single perfectly circular tubular object with known cross section profile the response at the center is maximized. Assuming Gaussian cross section profiles, $\sigma_K = r\sqrt{2}/2$ and $\tau = \sqrt{3}$ have to be used.

Pock et al. [9, 114]: The TDF of Pock $T^{\sigma_P}_{Pock}(\mathbf{x})$ also obtains boundariness samples $b_i = |B(\mathbf{x} + r\mathbf{v}_{\alpha_i})\mathbf{v}_{\alpha_i}|$ that are obtained at $N = \lfloor 2\pi r + 1 \rfloor$ discrete points with varying angle $\alpha_i = (2\pi i)/N$. However, in their approach the Hessian matrix $\mathcal{H}^{\sigma_P}(\mathbf{x})$ and the gradient information $\mathcal{B}^{\sigma_{P2}}(\mathbf{x})$ and are obtained on different scales, $\sigma_P = r$ and $\sigma_{P2} = r^{\eta}$ with $0.0 \leq \eta \leq 1.0$. The scale σ_P incorporates the whole structure for the tangent direction estimation, while σ_{P2} is smaller as it is only utilized to obtain boundary information. To combine the individual boundary responses into an offset medialness function, the authors also apply an averaging of the boundariness samples $\bar{b}(\mathbf{x}, r) = \frac{1}{N}\sum_{i=0}^{N-1} b_i$, but weight it with a parameter free symmetry criterion based on the variance $s^2(\mathbf{x}, r) = \frac{1}{N}\sum_{i=0}^{N-1}\left(b_i - \bar{b}\right)^2$: $T^{\sigma_P}_{Pock0}(\mathbf{x}) = \bar{b}(\mathbf{x}, r)(1 - s^2(\mathbf{x}, r)/\bar{b}(\mathbf{x}, r)^2)$. Additionally, an adaptive thresholding is applied to suppress responses away from the tubes centers where the gradient magnitude ideally vanishes such that the final TDF response is obtained as $T^{\sigma_P}_{Pock}(\mathbf{x}) = \max\{T^{\sigma_P}_{Pock0}(\mathbf{x}) - |\mathcal{B}^{\sigma_P}(\mathbf{x})|, 0\}$.

2.3 Tube Detection using Gradient Vector Flow

In the last section, we studied different popular TDFs. What they all had in common is that they utilized a linear (Gaussian) scale space to cope with the varying size of tubular objects. They all were based on the assumption that the tubular objects form bright structures in front of a homogeneous darker background without any other nearby image structures. These assumptions hold for some application domains, however, they limit the applicability of these TDFs in complex datasets where a variety of other image structures are present. In this section, we analyze the underlying problem that is related to the used Gaussian scale space and we develop a novel approach for detecting tubular structures that addresses this problem.

Figs. 2.3(a) and (f) show the aorta in a CT dataset with no contrast enhancement. The aorta is surrounded by a variety of different tissues and image structures and the contrast to the background varies. For example, the ascending aorta is separated from the heart chambers only by a thin darker structure, while in some areas even no boundary is visible. The descending aorta is on the one side adjacent to the much darker lung tissue, while on the other side it is tangented by the much brighter spine. Figs. 2.3(b)-(e) and (g)-(j) show the same image in the Gaussian scale space. As can be seen, on smaller scales the Gaussian smoothing solely leads to a reduction of the image noise, while on larger scales structures diffuse into each other. On very large scales even the individual parts of the spine diffuse into each other. Also close nearby smaller tubular structures may diffuse into tube-like structures on a larger scale, leading to false responses. This highlights the limitations of the Gaussian scale space and shows that it is generally not the appropriate choice for detection of blood vessels in such complex medical images.

As discussed above, TDFs in Gaussian scale space (Section 2.2) utilize – directly or indirectly – the first order spatial derivatives to identify tubular objects, because tubular objects show characteristic gradient vector fields which can be used for classification. Therefore, the whole tube detection process can be split into two parts: deriving an appropriate gradient vector field V from the given image I and a subsequent classification based on this vector field.

While for classification several methods have been studied in the literature – some

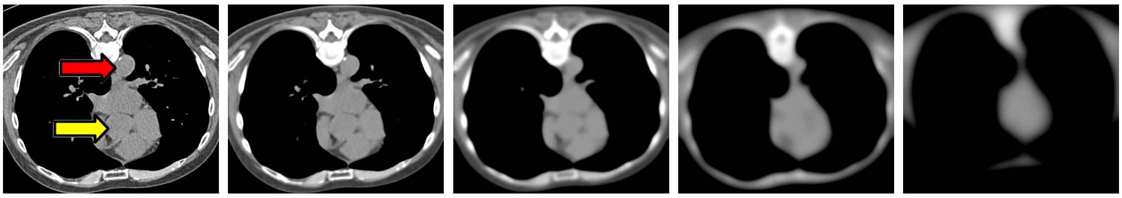

(a) Original (b) $\sigma = 1.0$ (c) $\sigma = 2.5$ (d) $\sigma = 5.0$ (e) $\sigma = 10.0$

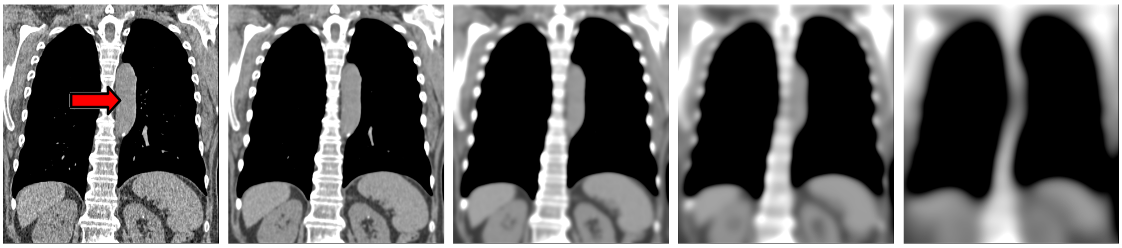

(f) Original (g) $\sigma = 1.0$ (h) $\sigma = 2.5$ (i) $\sigma = 5.0$ (j) $\sigma = 10.0$

Figure 2.3: Scale space of a non-contrast CT dataset showing ascending (yellow arrow) and descending aorta (red arrow). Top row: axial view. Bottom row: coronal view.

of them have been presented in Section 2.2 – they all relied on the computation of the gradient vector field at multiple scales. Given a specific scale σ, the gradient vector field V_σ is computed by convolution of the original image with a Gaussian filter kernel G_σ and computation of the local derivatives: $V_\sigma = \nabla(G_\sigma \star I)$ which equals $G_\sigma \star \nabla I$. This explicit formulation of the linearity points out that the computation of the gradients in the Gauss-smoothed image equals the Gauss-smoothing of the gradients obtained in the original image, what can also be interpreted as a distribution of gradient information over the image domain. When the scale is adapted appropriately to the size of the tube, the resulting vector field shows the typical characteristics of a tube at their centerlines (Fig. 2.4(b)). However, when the scale gets larger, nearby objects diffuse into one another and may produce vector fields that can also be interpreted as tubular objects (Fig. 2.4(c)). This behavior is inherent in the linear scale space, as Gaussian filtering is a non-feature-preserving isotropic diffusion process.

To avoid such a diffusion of image gradients over edges in the image, it is necessary to replace the Gaussian diffusion of the initial vector field F^n by a feature-preserving (edge-preserving) diffusion process. Feature-preserving diffusion of the original image does not solve the problem, because for tube detection it is necessary to distribute gradient

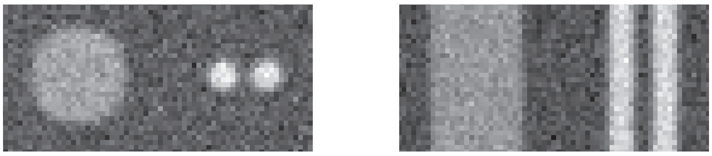

(a) Original image showing 2D cross sections of 3D tubular structure. Left: Cross section orthogonal to tubes tangent direction. Right: Cross section along the tubes tangent direction.

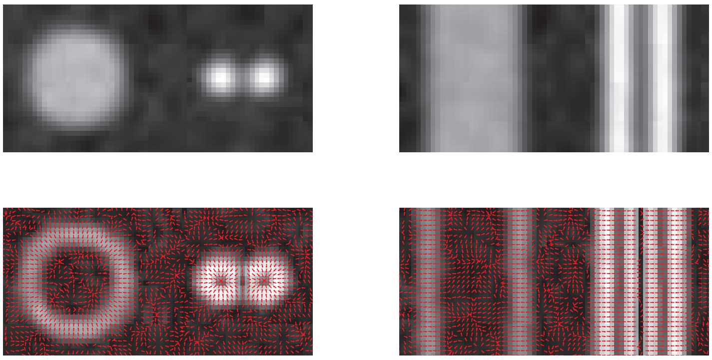

(b) Filtered image and corresponding gradient vectors (vector: direction, gray value: magnitude) on a small scale.

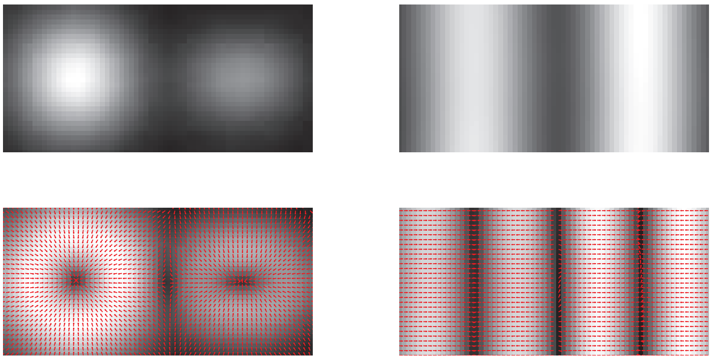

(c) Filtered image and corresponding gradient vectors (vector: direction, gray value: magnitude) on a large scale.

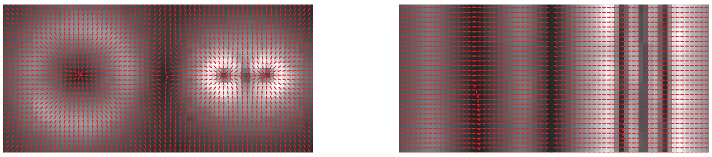

(d) Gradient Vector Flow result.

Figure 2.4: Comparison between gradient vectors obtained from Gaussian scale space and the Gradient Vector Flow.

information from the boundary of the tubular object towards its center. The key is to perform a feature preserving diffusion of the gradient information. A method that fulfills this requirement - edge-preserving diffusion of gradient information - is the GVF as presented by Xu and Prince [168]. Given an initial vector field $F^n(\mathbf{x})$, the GVF is defined as the vector field $V(\mathbf{x})$ that minimizes:

$$E(V) = \iiint_{\Omega} \mu|\nabla V(\mathbf{x})|^2 + |F^n(\mathbf{x})|^2|V(\mathbf{x}) - F^n I(\mathbf{x})|^2 d\mathbf{x}, \tag{2.3}$$

where $\mathbf{x} = (x, y, z)$, Ω represents the image domain, and μ is a regularization parameter that has to be adapted according to the amount of noise present in the image. The variational formulation of the GVF makes the result smooth where the initial vector magnitudes are small, while keeping vectors with high magnitude nearly equal. In practice, the GVF preserves even weak structures while being robust to large amounts of noise [168].

For tubular objects, applying the GVF to a vector field obtained from a small scale gradient vector computation results in the vector field shown in Fig. 2.4(d). Compared to the vector fields derived from the Gaussian scale space, the GVF has two different properties. First, the problem of the Gaussian scale space, diffusion of gradients over image boundaries, is avoided. Second, for tubular objects the GVF results in a vector field with similar characteristics as obtained with the multi-scale gradient computation when the scale is adapted appropriately to the tubes size. Similar to the gradient vectors computed at the appropriate scale in the Gaussian scale space, the gradients magnitude of the GVF fields vector decreases with increasing distance from the boundaries, and it vanishes towards the center of the tubular structures. This allows detection of tubular objects directly from the vector field produced by the GVF - without the need for a multi-scale analysis.

Because of these facts, the GVF can – to some extent – be used as a replacement of the multi-scale gradient vector computation performed by other tube TDFs, as the resulting vector field shows similar characteristics that are utilized by conventional approaches. In the following, we present combinations of the GVF with a (a) central medialness function and (b) an offset medialness function and show necessary adaptations when using the GVF field. While the combination with the central medialness function is faster to compute, the combination with the offset medialness function shows a higher selectivity and additionally provides radius estimates for the tubes.

2.3.1 Combination with Central Medialness Function

As discussed in Section 2.2.1, central medialness functions utilize the local gradient vector field to obtain a tube-likeliness measure. These methods utilize the fact that for tubular structures the gradient vectors point directly towards the centerline of the tube and that the vector field shows a large variance in two dimensions, and a low variance in the third dimension (see Fig. 2.4). Similar to methods based on the Hessian matrix, the derivate of the GVF field can be utilized for the classification. However, a normalization of the vectors is necessary because the vectors magnitude is not of importance: $V^n(\mathbf{x}) = V(\mathbf{x})/|V(\mathbf{x})|$. From the derivative of this vector field $H(\mathbf{x}) = \nabla V^n(\mathbf{x})$ and its eigenvalues $|\lambda_1| \leq |\lambda_2| \leq |\lambda_3|$, plate-like, blob-like, and tubular structures (brighter or darker than the background) can be distinguished similar to conventional central medilaness functions.

We combine the method with the tube-likeliness measure of Frangi et al. [44] (see equation (2.2)) and use default parameters $\alpha = 0.5$, $\beta = 0.5$, and $c = 100$. While with Frangi's method usually the parameter c has to be adapted depending on the expected noise level, here a fixed value can be utilized, as the noise suppression is already performed by the GVF. This combination of the GVF with Frangi's tube-likeliness measure allows the detection of tubular structures at their centerlines, independent of the tubes size and contrast.

2.3.2 Combination with Offset Medialness Function

As discussed in Section 2.2.2 on offset medialness functions, these methods utilize information away from the tubes center. Similarly to the method of Krissian et al. [70], we present a method that initially obtains an estimate of the tubes cross-sectional plane and performs a fitting of circles with varying size circle in this plane.

To obtain an estimate of the tubes cross-sectional plane, the derivate of the GVF field $H(\mathbf{x}) = \nabla V^n(\mathbf{x})$ and it's eigenvalues/eigenvectors are utilized, where the cross-sectional plane is spanned by the eigenvectors v_2 and v_3 associated with the two smaller eigenvalues. As can be seen from Fig. 2.4(d), the magnitude of the vectors vanishes toward the center of the tubular objects. Thus, candidate centerline points of tubular objects can be identified as local directional minima considering the magnitude of the GVF field vectors. This avoids the computation of the computationally expensive offset medialness function at undesired locations.

After determining the candidate centerline points and their cross-sectional plane, a tube-likeliness measure is obtained for these points by fitting a model to the GVF field.

The fitting term [70] is obtained as the mean flow through the circle and depends on the radius r: $T(\mathbf{x}, r) = \frac{1}{2r\Pi} \int_{\alpha=0}^{2\Pi} \langle V(\alpha, r), D(\alpha) \rangle \, \mathrm{d}\alpha$ [*]. $V(\alpha, r)$ represents the GVFs vector at the circle point and $D(\alpha)$ defines a normal vector on the circle pointing towards its center. For the circle fitting, the TDF response steadily increases with increasing radius until the circle touches an actual edge/surface of the object. Increasing r further results in a drop of $T(\mathbf{x}, r)$ as the magnitude of the vectors drop off. Thus, the fitting is performed for increasing radii as long as the fitting term increases. The best fit provides the tube-likeliness $T(\mathbf{x})$.

In this way a tube-likelness measure and a radius estimate are obtained for each potential centerline point.

2.3.3 Adaption to Varying Background Conditions

In the last sections we showed how the GVF field can be utilized for detection of tubular structures using conventional central or offset medialness functions. The basic requirement was an initial vector field $F^n(\mathbf{x})$ where at edge points the vectors have a larger magnitude than the noise regions and where the vectors point toward the center of the tubular object.

Depending on the expected background conditions, such an initial vector field can be obtained from the gray value image by computing image gradient vectors, using $F = \nabla I^\sigma$ for structures surrounded by darker tissue (e.g. angiography images) or $F = -\nabla I^\sigma$ for structures surrounded by brighter tissue (e.g. airways), or from a gradient magnitude map using $F = -\nabla |\nabla I^\sigma|$ in case of tubular structures that may be surrounded by arbitrary backgrounds. The resulting vectors fields for these three cases are are shown in Fig. 2.5. As can be seen from the results, in all cases the resulting vector fields show the characteristic properties necessary for the tube detection approaches. In contrast to conventional Gaussian scale space based TDFs, the gradient information can be obtained on a small scale that only accounts for image noise. The ability to cope with structures surrounded by arbitrary step edges is an issue that can not be addresses by conventional Gaussian scale space methods, and represents an advantage of our approach.

The tubular structures found in medical datasets may show a large variability of contrast. To account for this variability, a normalization of the initial gradient information can be used, treating all gradients with a minimum magnitude as definite edges: $F^n(\mathbf{x}) = F(\mathbf{x}) / |F(\mathbf{x})| * (min(|F(\mathbf{x})|, F_{max}) / F_{max})$ where $\mathbf{x} = (x, y, z)$. This normalization has the effect that the response for tubular structures primarily depends on the shape and

---

[*] The integral is approximated in practice by computing the sum over 32 discrete circle points.

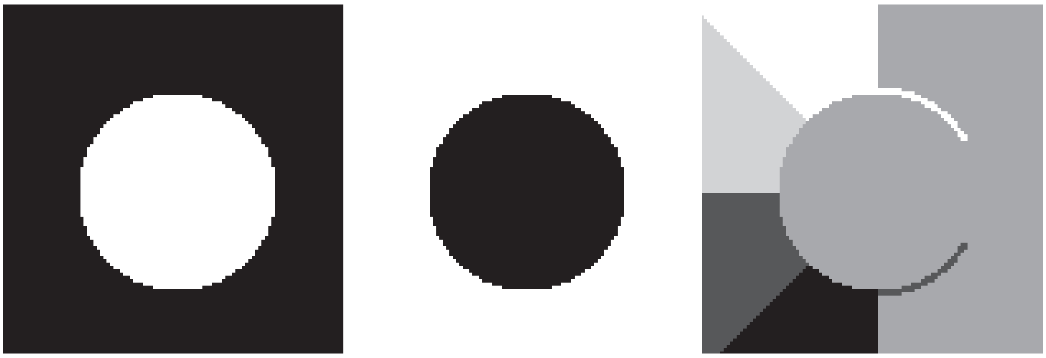

(a) Tubular objects with different background. From left to right: dark background, bright background, varying background.

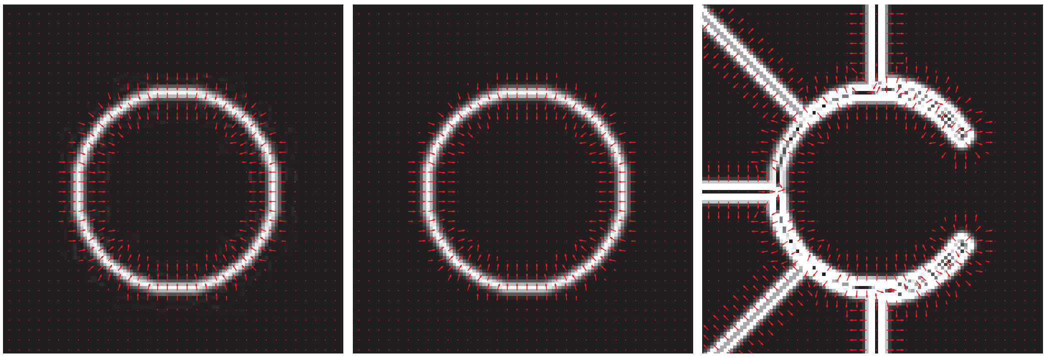

(b) Initial vector fields (vector: direction; grayvalue: magnitude) depending on expected background.

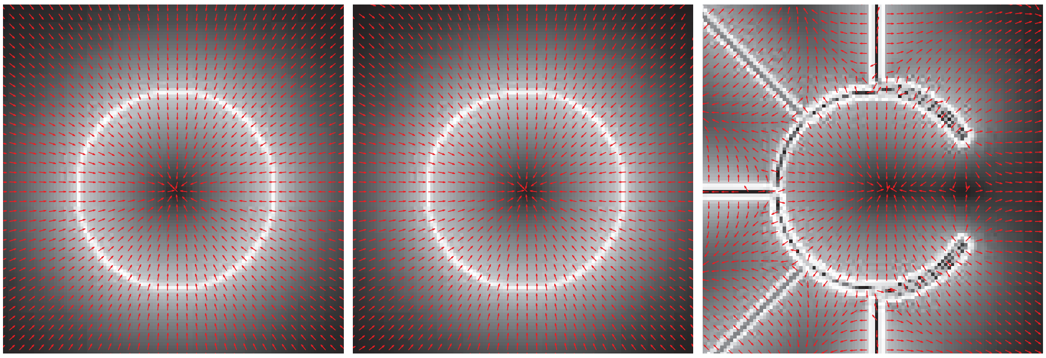

(c) Resulting Gradient Vector Flow fields (vector: direction; grayvalue: magnitude).

Figure 2.5: Initializing the GVF differently for different backgrounds conditions.

not on the contrast of the tubular structures. Additionally, it allows the use of a fixed regularization parameter μ for the GVF that is otherwise problematic to adapt in practice.

2.4 Centerline Extraction using Ridge Traversal

As outlined in the introduction, we are interested in extracting structural (centerline based) representations of all tubular objects in a given volume of interest. In the last sections, we presented various TDFs that allow a bottom-up detection of tubular objects by obtaining a tube-likeliness $T(\mathbf{x})$ for each voxel of an image. They all have in common, that the tube-likeliness (aka. medialness) increases towards the centers of the tubular objects and their response decreases at locations away from the tubes center or in case of other deviations from a tubular shape (e.g. junctions). Therefore, centerline based representations can be obtained from the tube-likeliness images by extracting those height ridges. In this section, we present an efficient procedure for this task based on traversing these height ridges. We combine the ridge traversal with a hysteresis thresholding with the upper threshold t_{high} and the lower threshold t_{low} to allow local variations from a perfectly tubular structure along the centerline. The algorithm is listed in Algorithm 1 and explained below.

The height ridge traversal method requires a starting point $\mathbf{x}_0$ on a height ridge and an estimate of the ridges tangent direction $t(\mathbf{x})$, as obtained with all the presented TDFs, to extract its associated centerline. Starting from $\mathbf{x}_0$ the height ridge is traversed independently into both directions $\mathbf{t}_0$ and $-\mathbf{t}_0$. For a current centerline point on the height ridge $\mathbf{x}_i$, all local neighbors $\mathbf{x}_i^n$ with $\overrightarrow{\mathbf{x}_i\mathbf{x}_i^n} \cdot \mathbf{t}_i > 0$ are considered, and the neighbor point with the highest medialness response is chosen as the next centerline point $\mathbf{x}_{i+1}$ on the height ridge. The tangent direction $\mathbf{t}_{i+1}$ of $\mathbf{x}_{i+1}$ is set to $\mathbf{t}_{i+1} = \text{sign}(\overrightarrow{\mathbf{x}_i\mathbf{x}_{i+1}} \cdot \mathbf{t}_{i+1})\mathbf{t}_{i+1}$ to maintain the direction during traversal and the procedure is repeated until a stopping criterion is met. The procedure is stopped when the tube-likeliness $T(\mathbf{x})$ falls below a given threshold t_{low} or an already processed centerlinepoint is reached. The second stop condition is necessary to avoid that the same height ridge is traversed several times. In this way the centerline associated with a height ridge is extracted.

To obtain a starting point for each height ridge following property of the TDFs can be used: the tube-likeliness increases for tubular structures and the response falls off in proximity of junctions. Thus, we can conclude that there is for each tubular structure at least one local maximum in the tube-likeliness image. Therefore, all local maxima in the tube-likeliness image with a value $T(\mathbf{x}) > t_{high}$ are considered as starting points for the height-ridge traversal. These starting points are processed in descending order of their associated tube-likeliness.

Using this ridge traversal in combination with the TDFs, centerline based structural representations of all tubular structures can be extracted. Additionally, one may assign each of these centerline points an associated gray value (from the original image), a radius estimate and a tangent-direction estimate (from the TDFs), which may also give useful information for further processing steps.

2.5 Experiments

In this section, we study the behavior of the previously presented Gaussian scale space based TDFs (Section 2.2) and the GVF-based approaches (Section 2.3) on synthetic and clinical datasets.

For all Gaussian scale space based approaches, the default parameters suggested by the authors were used, and the filter responses were obtained between the optimal scale for tubular structures with a radius of one voxel and the optimal scale for a tubular structure with a radius of 1.5 times the radius of largest interesting tubular structure. With Frangi's approach $\alpha = 0.5$, $\beta = 0.5$, and c equal to half of the maximum Hessian norm in a clearly identifiable vessel were used. With Krissian's approach $\sigma_K = r\sqrt{2}/2$ and $\tau = \sqrt{3}$ were used. Pock et al. [114] did not make any suggestions in their earlier work, however in [9] $\mu = 0.5$ was used on the synthetic datasets and we also used this parameter.

With both proposed GVF-based approaches the edge information was obtained at a scale of $\sigma = 1\ voxel$ (intra-slice resolution) and the normalization parameter F_{max} was adapted to the contrast of a clearly identifyable vessel in a similar manner as with Frangi's approach. The GVF itself was performed using default parameters of $\mu = 5$ and 500 iterations for the iterative computation scheme [168].

In order to visualize the datasets and to make the filter responses comparable, all images shown in the next sections were produced using a maximum intensity projection for visualization. The gray value ranges of the datasets were adapted for visualization to show the full data range.

Exceptions using other parameters or another visualized gray value range are mentioned explicitly.

2.5.1 Synthetical Datasets

In this section, we demonstrate the general behaviour of the presented TDFs under varying tube configurations, varying cross section profiles, varying contrast levels, and varying noise levels under controlled and reproducible conditions using synthetic datasets. Where available, public datasbases were used to make the results comparable with other methods. In these datasets, the tubular objects show different kinds of edge-types as they appear in medical datasets: perfect step edges, slightly blurred step edges (due to partial voluming), and tubes with Gaussian cross-section profiles.

Varying tube configurations: The public database of Krissian and Farneback[†] [69, 71] (Fig. 2.6(a)), shows standard situations of tubular objects, as they occur in vascular systems. One of the most obvious differences between the Gaussian Scale Space based methods and our proposed GVF-based methods is that the GVF-Based methods only produce responses near the centers of the tubular structures, while the other methods also produce responses away from the tube center. For junctions of tubular objects with largely varying diameters, the response of most methods falls off slightly with all approaches as these parts are not really tubular; However, as pointed out by Bennink et al. [11], this behavior may be assumed as correct for pure lineness filters. In case of the tube with the varying diameter, all methods allow for extraction of the correct centerline, but as the structure of this tube becomes more blob-like the response of Frangis's method, Pock's method, and our proposed method falls off slightly. The response of Krissian's approach on the other hand is wider than the tubular object itself. The datasets with the tangenting tubes and the helix highlight the problem of the linear scale space analysis. All the Gaussian scale space based methods produce high responses outside the tubular objects, because on a larger scale these structures diffuse into one another. A separation is not possible anymore. In contrast, the response of our GVF-based methods is insensitive to influences outside the tubular objects and they respond only at the correct centerline of the tubes.

Varying cross section profiles: Fig. 2.7(a) shows 3D tubular structures with varying cross section profiles (shape and edge type) representing typical situations as they occur in clinical datasets. The used cross section profiles represent (from left to right) two perfectly circular tubular structures with step edges and different contrast, a step edge convolved

---

[†] http://lmi.bwh.harvard.edu/research/vascular/SyntheticVessels/SyntheticVesselImages.html

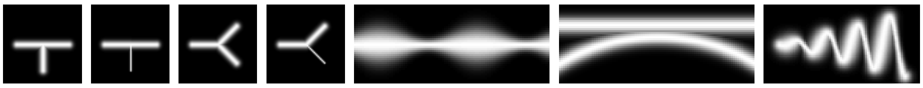

(a) Datasets from the public database of of Krissian and Farneback [69, 71].

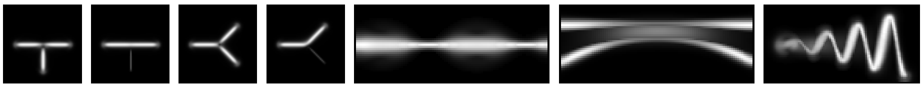

(b) Response of Frangi's method [44].

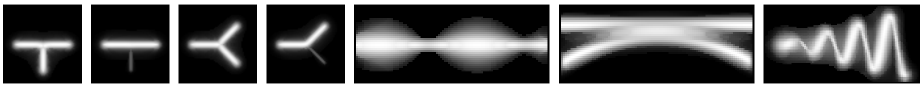

(c) Response of Krissian's method [70].

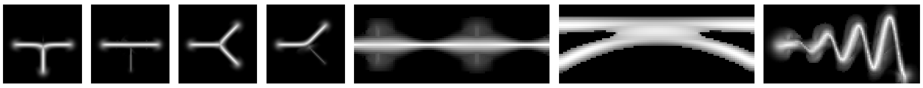

(d) Response of Pock's method [114].

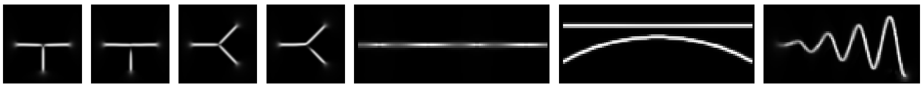

(e) Response of the GVF-based approach with the central medialness function (Section 2.3.1).

(f) Response of the GVF-based approach with the offset medialness function (Section 2.3.2).

Figure 2.6: 3D tubular objects in varying configurations and responses of the different TDFs. From left to right: T-junction with constant diameter, T-junction with varying diameter, Y-junction with constant diameter, Y-junction with varying diameter, tube with varying diameter, tangenting tubes, helix.

with a Gaussian, a pure Gaussian cross section profile, a cross section with an ellipsoidal shape, two large closely tangenting perfectly tubular objects, a thinner tubular structure, two thinner closely tangenting tubular objects, and another non-tubular structure that represents a slightly curved surface path.

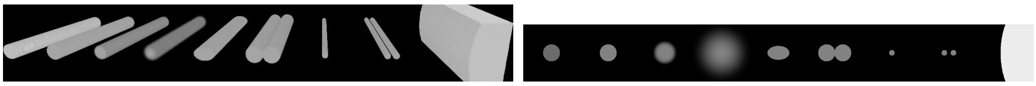

(a) 3d volume rendering.

(b) 2d cross sections of 3d objects.

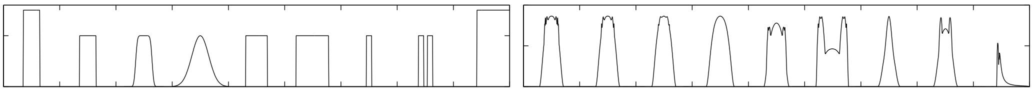

(c) 1d cross sections of 3d objects.

(d) Response of Frangi's method [44].

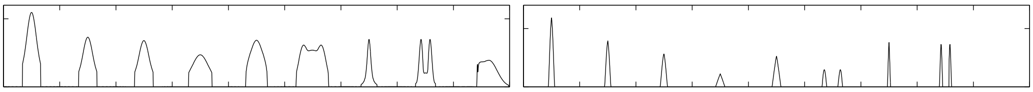

(e) Response of Krissian's method [70].

(f) Response of Pock's method [114] using typical parameter $\eta = 0.5$. For variations of η see Fig. 2.8.

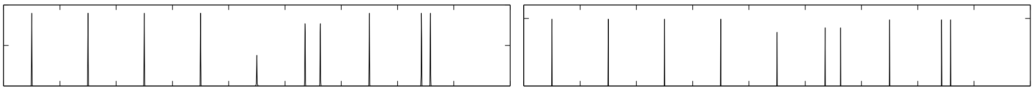

(g) Response of GVF-based tube detection with central medialness (Section 2.3.1).

(h) Response of GVF-based tube detection with offset medialness (Section 2.3.2).

Figure 2.7: Tubular structures with varying cross section profile representing situations found in typical CT datasets and responses of different TDFs. The x-axis indicates the location and the y-axis the contrast/response.

Fig. 2.7(d)-(h) show the responses of the different TDFs. With all the approaches the responses descreases with increasing deviation from the expected cross section profiles (ellipse) or in case of other nearby image structures (e.g. another closely tangenting tube). In case of the TDFs of Krissian and Pock the response is also correlated with the edge-type (blurred edges, or Gaussian cross section profile), while with the method of Frangi and the GVF-based approaches the responses do not decrease in these cases. The TDFs of Frangi and Krissian also produced quite strong responses for the surface patch like structure and between the closely tangenting tubular objects. The GVF-based approaches do not produce responses between the closely tangenting tubular objects as we have already seen in the experiments of the varying tube configurations (see Fig. 2.6).

However, the approach of Krissian does not produce any response between these closely tangenting tubular objects in Fig. 2.7(e), in contrast to the example in Fig. 2.6(d) where it did.

This behavior deserves a closer investigation and explanation. With Pock's approach two different scale spaces are utilized where the scale at which the boundary information is obtained depends on a parameter η. Moreover, the relation between the radius of the tubular objects and the boundary information is non-linear ($\sigma_{P2} = r^{\eta}$ with $0.0 \leq \eta \leq 1.0$ as explained in Section 2.2.2), meaning that the response also depends on the size of the tubular objects explaining the different results between the two figures. The approach of Pock addresses the problem of the pure Gaussian scale space methods (Frangi, Krissian), by computing the boundary information on a smaller scale. However, this computation of the boundary information on a smaller scale represents a tradeoff with this method as illustrated in Fig. 2.8. Computing the boundary information on a too large scale, the method shows the same problems as Krissians approach and produces responses between the tubular objects (Fig. 2.8(a)), while computing the boundary information on a too small scale, the method can not account for deviations from a perfectly circular cross section (e.g. ellipsoidal) (Fig. 2.8(b)).

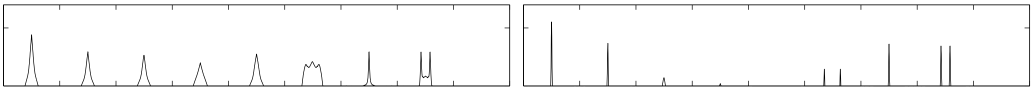

(a) Response of Pock's method [114] using very large $\eta = 1.0$.

(b) Response of Pock's method [114] using very small $\eta = 0.0$.

Figure 2.8: Influence of η on the TDF response with Pock's method [114] for the tubular structures shown in Fig. 2.7(a).

With the GVF-based approaches this tradeoff does not exist. The edge information is computed on a very small scale and the GVF diffuses the gradient information, thus making it still possible to produce reasonable responses to slight variations from a perfectly circular cross section profile (ellipsoid). The method of Pock and the GVF-based approaches do not produce any response for surface patches contrary to the methods of Frangi and Krissian.

Varying contrast level: In Fig. 2.9 the effect of varying contrast is shown. For the TDF of Frangi and the GVF-based methods the parameters were adapted accordingly to the contrast indicated by the dotted line, while the methods of Krissian and Pock do not have a parameter that can be adapted to the expected contrast. As shown from the results, with the methods of Krissian and Pock the responses depend linearly on the contrast, while with the other approaches the response saturates above the expected contrast and starts decreasing with lower contrast than the expected one. One may argue that the methods of Krissian and Pock do not require an adaption to the expected contrast, however, on the other side this implies that for extraction of the tubular structures it is necessary to adapt thresholds on the TDF response appropriately to achieve a discrimination from noise responses. Morover, because of this behavior the methods of Krissian and Pock also produce strong responses to structures with a strong contrast, even in case the structure itself strongly deviates from a tubular shape. In contrast to that, the method of Frangi and the GVF-based method produce normalized results allowing to use the same set of parameters for extraction of the actual tubular structures.

Varying noise level: The datasets provided by Aylward et al.[‡] [2], see Fig. 2.10, contains a tortuous, branching, tubular object with vanishing radius. The contrast between the tubular object and the background ranges from 100 at the center of the tube to 50 at the tube's edge. The datasets were corrupted with additive Gaussian noise with increasing standard deviations η of 10, 20, 40 and 80. "The $\eta = 20$ data is representative of the noise level in MR and CT data. The $\eta = 40$ data more closely resembles the noise magnitude of ultrasound data. [...] The $\eta = 80$ images are well beyond any worst case number [...] for any clinically acceptable MRA, CT, or ultrasound data."[2].

For Frangi's method and the GVF-based methods, the noise-sensitivity parameters, c and F_{max}, respectively, were adapted on the low noise dataset ($\eta = 10$). As already mentioned above, the methods of Krissian and Pock do not allow controlling the influence of contrast on the filter response. As a result, with these methods the response to image noise increases with an increasing noise level. The GVF-based approaches produce clean responses at the centers of the tubular objects even under high (clinically acceptable) noise levels ($\eta = 10$, 20, and 40), although for noise reduction only a Gaussian smoothing with a very small variance ($\sigma = 1.0$) was used. This shows that in practice only a Gaussian smoothing with a very small variance is necessary. Computation of gradient information on a large scale as done by the Gaussian scale space based methods is not necessary to account for image noise. However, in case of insufficient noise suppression the GVF-based method with the central medialness function produces unsatisfying results, while the GVF-based method with the offset medialness function shows a slightly better behavior, as shown in

---

[‡] http://ij.itk.org/midas/item/view/1065

(a) 3d volume rendering

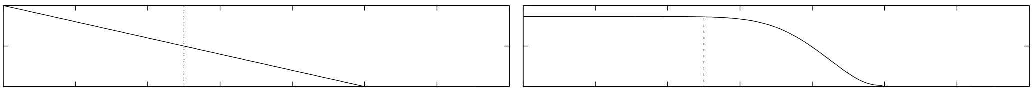

(b) 1d cross section showing contrast

(c) Response of Frangi's method [44].

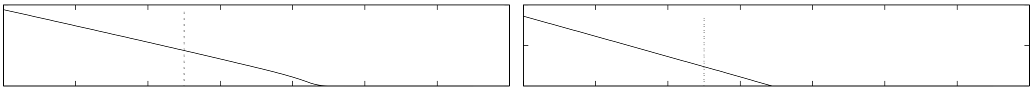

(d) Response of Krissian's method [70]

(e) Response of Pock's method [114].

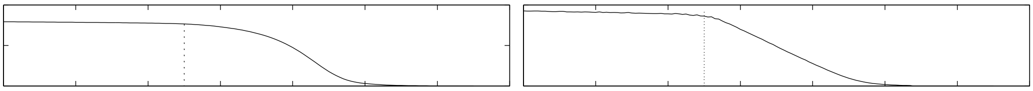

(f) Response of GVF-based tube detection with central medialness (Section 2.3.2).

(g) Response of GVF-based tube detection with offset medialness (Section 2.3.2).

Figure 2.9: Tubular structure with vanishing contrast and responses of different TDFs. The x-axis indicates the location and the y-axis the contrast/response. The dotted line in (b) indicates the contrast for which the parameters were adapted.

Figs. 2.10(e) and (f) on the very right.

2.5.2 Clinical Datasets

In this section, we apply the three methods to three medical volume datasets and show the impact of the results obtained on the synthetic datasets on clinical datasets.

CT angiography: In the top row of Fig. 2.11, a CT angiography image and enlarged subregions of challenging areas are shown. The main problems for TDFs with this kind of dataset are the detection of very thin low contrast vessels, diffuse edges, and closely adjacent vessels. Note that Frangi's and Krissian's methods were specifically designed for angiography images.

The overview image of the whole dataset (leftmost column) shows that our approach works similarly well for wide tubes with bar-like cross-section profiles and for very thin tubular objects with Gaussian cross-section profiles. The magnified subregion showing the tangenting tubes (second column), verifies the results of the synthetic datasets. The Gaussian scale space based approaches diffuse the closely adjacent structures into one another, making an extraction of height ridges as suggested by Krissian et al. [71] for centerline extraction impossible. Our approach allows a clear separation of both. The magnified subregion shows some very thin low contrast vessels (third column). As the responses of Frangi's and Krissian's methods decrease with decreasing contrast (see Fig. 2.9), the response to low contrast vessels also decreases. This makes a separation from the background difficult (e.g. based a single threshold as suggested by Krissian et al. [71]). Our approach is insensitive to changing contrast situations and finding a single threshold for extraction of the centerlines is easier. The magnified subregion on the very right column shows another example of very thin tubular structures. The vessels overlap completely in the image because of the partial volume effect. None of the methods is able to separate them because they work on voxel level.

Contrast enhanced CT of the liver: In Figs. 2.12(a) and (b) a contrast enhanced liver CT dataset is shown. For TDFs the main problems with these kinds of datasets are the complex surrounding of the liver (other orangs, bones, etc.), the tumor that forms a blob like structure and the low contrast to noise ratio for the thinner blood vessels. The method of Pock [9, 114] was specifically developed for this kind of datasets.

As the results of the TDF responses show (Figs. 2.12(c)-(g)), the methods of Frangi and Krissian produce strong responses inside the liver at the transitions to other nearby organs with a lower density (e.g. the transition to the lung). Contrary to that, the method of Pock and the GVF-based methods do not show this behavior. The methods of Frangi, Pock, and the GVF-based methods are also capable of suppressing the blob-like tumorous image structure, showing the ability to identify tubular structures and to discriminate them from other structures. On the other hand, the methods also do not respond to the blood vessel adjacent to the tumor. The response with all approaches also decreases considerably or breaks up completely at branching areas, as these parts of the vascular structures deviate significantly from a typical tubular shape.

CT of the aorta: To demonstrate the performance of the different methods in a more complex environment, the methods have been applied to a CT dataset without contrast enhancement of the abdomen showing ascending aorta, descending aorta and the aortic arch (see Figs. 2.13(a) and (b)). The aorta is surrounded by multiple different tissues, parts of the background are brighter (the spine), some parts of the background are darker (the lung), and in some areas a discrimination from ascending image structures is difficult (inside the heart). These situations are problematic for conventional TDFs. With our approach, the GVF-flow was initialized to cope with varying step edges (Section 2.3.3). The results of the Gaussian scale space based methods on this dataset (Figs. 2.13(c)-(e)) reveal the drawback of the linear scale space very clearly: the close proximity of spine and aorta disturbs the detection of the aorta when applying Franig's, Krissian's, or Pock's method. These methods produce undesired responses to several structures in the image, making a valid extraction of the aorta impossible. In Gaussian scale space, one may consider the whole spine as a tubular object at a large scale, but this disturbs the detection of smaller vessels in its close proximity. With the GVF-based approaches on the other hand (Figs. 2.13(f) and (g)), the detection of the aorta is not influenced by any surrounding structures, allowing for an extraction of the aorta (Fig. 2.13(h)).

2.6 Discussion and Conclusion

In this chapter, we were concerned with the extraction of tubular structures from medical images. We presented a novel approach for detection of tubular structures based on the GVF (Section 2.3) and compared it to several TDFs known from the literature (Section 2.2). In Section 2.5 we studied these TDFs on synthetic and clinical datasets showing some of their properties in different situations. For the extraction of the centerlines of the tubular structures from the TDF responses, the combination with a height ridge traversal procedure (Section 2.4) was presented, which allows for a fully automated bottom-up extraction of the interesting structures.

As shown from the examples, the GVF-based approach addresses a core problem of the Gaussian scale space based methods – the diffusion of nearby structures into one another on larger scales – what may lead to false responses. We showed that this can be avoided by using the GVF field as a replacement for the conventional multi-scale gradient vector computation. The resulting GVF-based methods proofed beneficial in case of surface patches or other nearby image structures and allow for a more selective extraction of tubular structures. Additionally, the method has the ability to cope with varying background conditions, an issue that can not be addressed using conventional Gaussian scale space based methods. This makes the presented GVF-based approach applicable in areas where the utilization of TDFs has not been considered so far.

However, as the GVF-based approaches only respond at the center of the tubular structures, these methods are not so suitable for visualization tasks where the TDFs are utilized for vessel enhancement, as is the case with Frangi's method. Also, the response of the GVF-based methods falls off completely in case a minimum contrast-to-noise ratio in the initial vector field is not given, while with the approaches of Krissian and Pock the response only decreases. Therefore, it may be necessary for some applications to use combinations of the GVF-based approach for sufficiently contrasted tubes and a conventional TDF computed only on a very small scale for the identification of thinner low contrast tubular structures in noisy datasets.

TDFs compute a tube-likeliness measure independently for each voxel of the image domain. This makes them ideally suited for GPU implementations and thus allows achieving low computation times. The Gaussian scale space based methods obtain a tube-likeliness measure for each voxel at multiple scales, meaning that their computation time depends linearly on the number of voxels and the number of used scales. With the GVF-based approach on the other hand, the tube-likeliness has to be computed only once for each voxel while the main computation time is on behalf of the GVF that has to be computed only once; the GVF is also easily parallelizeable and can be implemented on the GPU. Using such GPU based implementations of the TDFs, the computation times on typical volume datasets remain in the range of seconds to maybe few minutes on large datasets. E.g. on a CT dataset with an axis aligned bounding box surrounding only the liver ($380 \times 425 \times 210$ voxels), the computation time for the TDF of Pock et al. [114] is about 10 seconds when computed on 10 scales and the computation time for the GVF-based approach with the offset medialness function (Section 2.3.2) is about 15 seconds, using an NVIDIA GeForce 8800 GTX in both cases.

All TDFs have in common that the output (the tube-likeliness measure) decreases due to deviations from the assumptions about the tubular structures or decreasing contrast. In addition, the methods may also show some slight response to noise. Extracting tubular structures from the tube-likeliness images requires appropriate thresholding of this tube-likeliness. However, in particular in regions of the tubular trees that strongly deviate from a typical tube shape (e.g. junctions, stenosis) the tube-likeliness is as low or lower as in the noise image regions such that a discrimination of these cases based on thresholding is not possible. The presented height-ridge traversal with the incorporated hysteresis thresholding accounts for this problem to some extend and tolerates slight variations from a tubular structure. As a result of these issues only the tubular parts of tubular tree structures that don't deviate strongly from a perfectly tubular shape can be extracted with these methods.

Algorithm 1 Centerline extraction using ridge traversal.

```
input: Tube likeliness image $T(x)$ with tangent directions $t(x)$
input: thresholds $t_{high}$ and $t_{low}$ for double-thresholding

set $CL \leftarrow \{\}$ /* set of extracted centerlines */
image $C(x) \leftarrow false$ /* auxiliary centerline image */

/* obtain starting points */
queue M;
for each voxel $x \in T$ do
  if $T(x) > t_{high}$ and $T(x) \geq max_{y \in Adj26(x)} T(y)$ then
    $M \leftarrow M \cup \{x\}$
  end if
end for

/* traverse ridges */
while $M \neq \{\}$ do
  $x_0 \leftarrow$ extract($M$)
  if $C(x_0) = false$ then
    list $cl$ /* centerline associated with starting point $x_0$ */
    /* traverse in first direction $t(x_0)$ */
    point $x \leftarrow x_0$
    direction $t \leftarrow t(x_0)$
    repeat
      $cl \leftarrow pushFront(cl, x)$
      $C(x) \leftarrow true$
      point $x_n = argmax_{y \in Adj26(x)} T(y) sign(\overrightarrow{xy} \cdot t)$
      direction $t_n = t(x_n) sign(\overrightarrow{xx_n} \cdot t(x_n))$
      $x \leftarrow x_n$, $t \leftarrow t_n$
    until $T(x) < t_{low}$ or $C(x) = false$
    $cl \leftarrow popBack(cl)$ /* remove such that $x_0$ is only once in cl */
    /* traverse in second direction $-t(x_0)$ */
    point $x \leftarrow x_0$
    direction $t \leftarrow -t(x_0)$
    repeat
      $cl \leftarrow pushBack(cl, x)$
      $C(x) \leftarrow true$
      point $x_n = argmax_{y \in Adj26(x)} T(y) sign(\overrightarrow{xy} \cdot t)$
      direction $t_n = t(x_n) sign(\overrightarrow{xx_n} \cdot t(x_n))$
      $x \leftarrow x_n$, $t \leftarrow t_n$
    until $T(x) < t_{low}$ or $C(x) = false$
    $CL \leftarrow CL \cup cl$
  end if
end while

output: extracted centerlines CL
```

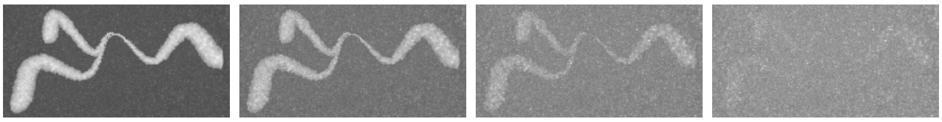

(a) Datasets from the public database of of Aylward et al. [2].

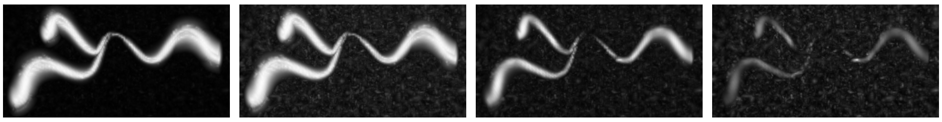

(b) Response of Frangi's method [44].

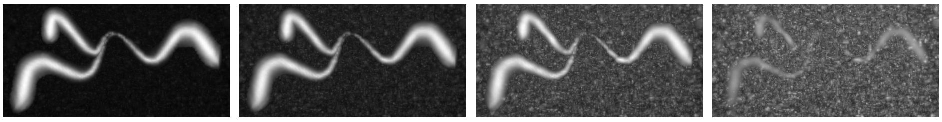

(c) Response of Krissian's method [70].

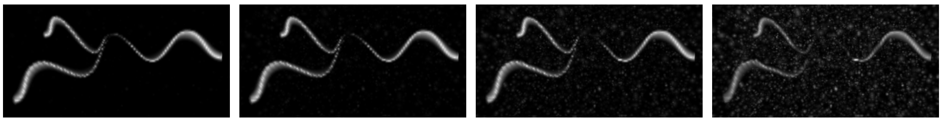

(d) Response of Pock's method [114].

(e) Response of the GVF-based approach with the central medialness function (Section 2.3.1).

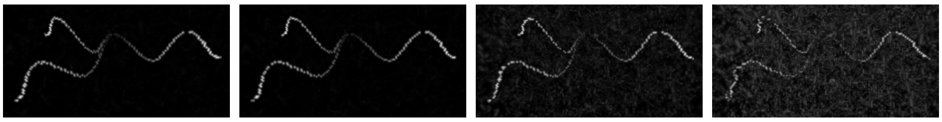

(f) Response of the GVF-based approach with the offset medialness function (Section 2.3.2).

Figure 2.10: Tubes with varying noise levels and responses of the different methods. From left to right: increasing noise level using additive Gaussian noise with standard deviations η of 10, 20, 40, and 80.

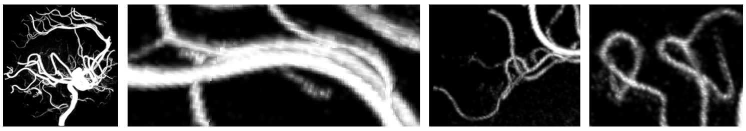

(a) Original dataset (left) and enlarged subwindows.

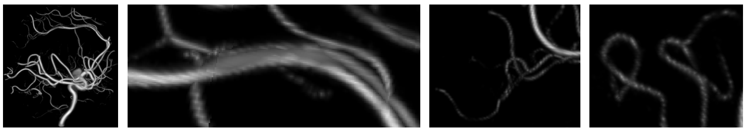

(b) Response of Frangi's method [44].

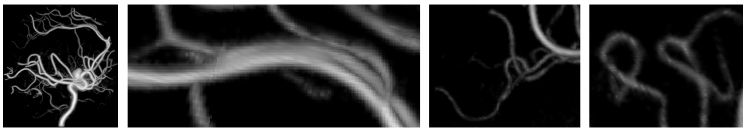

(c) Response of Krissian's method [70].

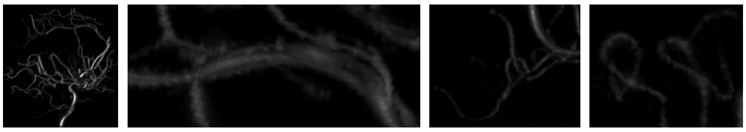

(d) Response of Pock's method [114].

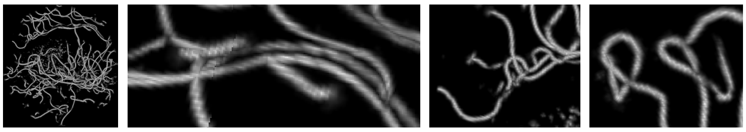

(e) Response of the GVF-based approach with the central medialness function (Section 2.3.1).

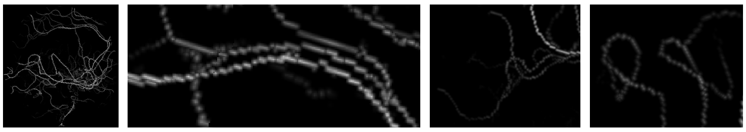

(f) Response of the GVF-based approach with the offset medialness function (Section 2.3.2).

Figure 2.11: CT angiography image and responses of the different methods. From left to right: overview of the whole dataset, closely tangenting vessels, thin vessels, overlapping vessels.

(a) Image slice of original dataset with adapted gray value range.

(b) Original dataset.

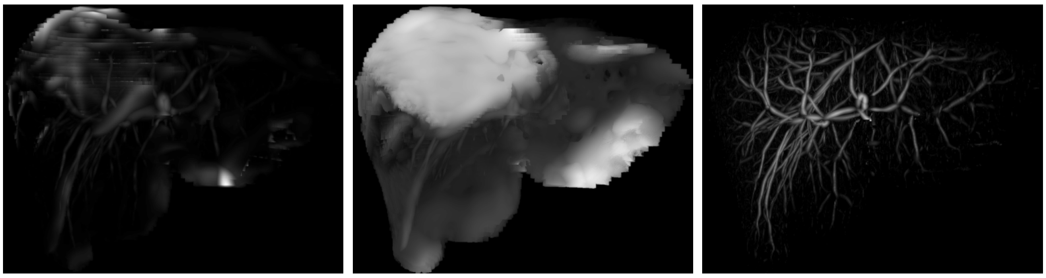

(c) Response of Frangi's method [44].

(d) Response of Krissian's method [70].

(e) Response of Pock's method [114].

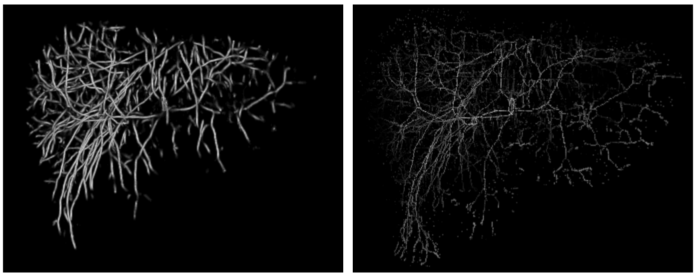

(f) Response of the GVF-based approach with the central medialness function (Section 2.3.1).

(g) Response of the GVF-based approach with the offset medialness function (Section 2.3.2).

Figure 2.12: TDF responses on contrast CT dataset of a diseased liver with a tumor visualized using liver mask.

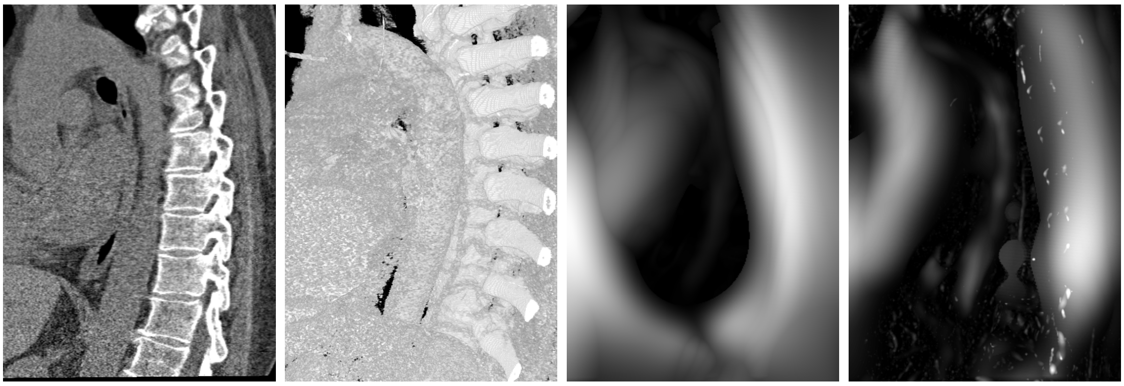

(a) Image slice of original dataset with adapted gray value range.

(b) Alpha blending of original dataset.

(c) Response of Frangi's method [44].

(d) Response of Krissian's method [70].

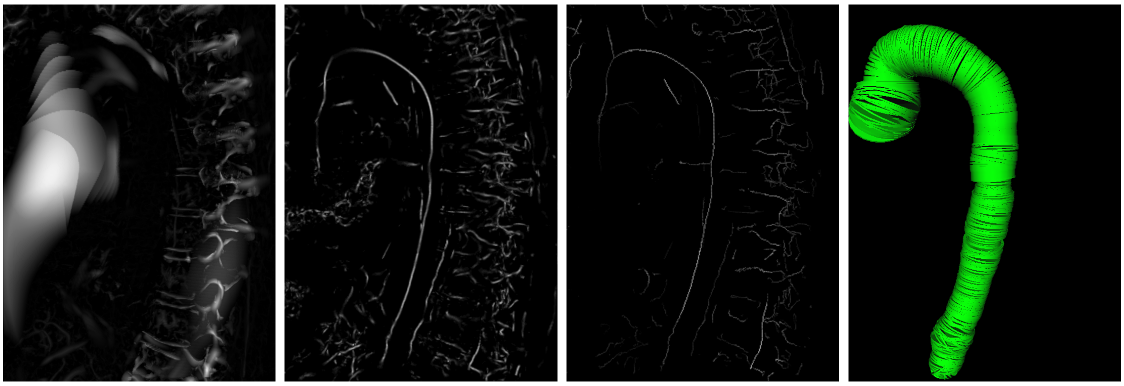

(e) Response of Pock's method [114].

(f) Response of the GVF-based approach with the central medialness function (Section 2.3.1).

(g) Response of the GVF-based approach with the offset medialness function (Section 2.3.2).

(h) Aorta extracted with the GVF-based approach with the offset medialness function.

Figure 2.13: TDF responses on CT of the abdomen showing the aorta in proximity to the spine.

Chapter 3

Grouping and Linkage into Connected Networks

Contents

3.1 Introduction

In the last chapter we presented different methods for the identification and extraction of tubular objects from medical images. With these methods major parts of tubular tree structures can be already described. However, the methods are not capable of coping with branching areas or other areas where the appearance of the vessels/airways strongly deviates from the typical tube shape. This may be because of stenosis, aneurysms, or tumors where the shape of the vessels/airways is perturbed, or in case of imaging artifacts or adjacent structures within the same gray value range. Due to these cases the tubular structures extracted with methods as the ones presented in the last chapter are unconnected. A second issue not addressed with TDFs is that they identify all tubular structures in a given volume of interest and they do not distinguish between multiple potentially interwoven tubular tree structures. Consequently, such structures need to be separated in an additional processing step.

In this chapter, we are concerned with the reconstruction of the complete tree structures from identified unconnected tubular structures. This requires, that the tubular structures belonging to the same tree have to be grouped and linked together. In this context, we refer to grouping as identifying which tubular structures are connected and are a part of the same tubular tree structure, and to linkage as finding a connecting path between the identified tubular structures.

In the literature only a few methods can be found that are addressing these issues. They are based on image information and/or structural information. Methods utilizing primarily image information make use of shortest path techniques and cost images typically derived from the image gray values [10, 24, 29, 114]. These methods suffer from shortcuttings; this induces that the linkage path may drift away from the center and/or that there may be wrong connections. Such methods are also not able to avoid misconnections between multiple overlapping tubular tree structures within the same gray value range. Methods utilizing primarily structural information make use of distance, radius, and/or blending angle between the identified tubular objects to obtain a connection confidence [18, 39, 58, 75, 138]. These confidence measures are typically utilized in a minimum spanning tree algorithm together with some centerline interpolation method to obtain connected skeletons of a tree structure. To the best of our knowledge, only one method has addressed the simultaneous reconstruction and separation of multiple interwoven tree structures from identified tubular objects. In this work Agam et al. [1] presented a method that is especially tailored to lung vasculature and imposes constraints that are only valid for this specific application. The separation of multiple overlapping tree structures is usually addressed based on the analysis of connected skeletons derived from existing segmentations utilizing radius information (e.g. [130]) or additionally angle information (e.g. [134]). However, such approaches based on skeletonization of segmentation results are sensitive to segmentation errors, especially to missing parts or leakage where the topology of the extracted centerlines is incorrect. Of course, combinations of image information and structural information are also used; e.g. verifying the interpolated linkage path determined by a structural connection method based on gray value evidence.

As can be seen from this literature review, two issues have not been addressed by other authors so far. Except in the lung case, no method has addressed the grouping/separation of unconnected tubular structures in case of multiple interwoven tree structures. No method is capable of extracting a linkage path that stays centered in regions where the shape strongly deviates from a typical tubular shape, thus resulting in a high quality curve skeleton. In the next two sections, we present two methods addressing these issues, using a structure based approach (Section 3.2) for the grouping/separation of tubular structures in case of multiple interwoven tree structures, and an image based approach (Section 3.3) for extraction of centered linkage paths.

3.2 Structure Based Approach

Biological tubular tree structures such as blood vessel trees or the airway tree show characteristic structural properties regarding their branching behavior (branching angle, radius). In this section, we present a method that addresses the reconstruction and separation of multiple potentially interwoven tubular tree structures based on such structural properties. The method incorporates distance information, radius information, and branching angle information in order to group unconnected tubular structures into biologically reasonable trees and to separate multiple interwoven tree structures from one another. Incorporation of branching angle information is in particular of importance in case of multiple interwoven tree structures where tube elements tangent each other and seem to overlap due to partial volume effects. Considering an afferent vessel system, the following characteristics can be observed. Starting from a root element, blood flows into a recursively branching vessel tree. The diameters of the vessels decrease and the direction does not change abruptly. Our reconstruction strategy tries to preserve this “flow” in the trees by taking geometrical properties into account. Starting from given root elements of the trees with known flow direction, tube elements are grouped and connected iteratively using a confidence function. This strategy allows the separation of the different interwoven trees and the reconstruction of valid skeletons for the individual trees by closing gaps between the individual tubular structures which separate parts of the trees. During this process, high-level structural representations of the whole trees are derived which describe the parent-child relationships between the tube elements.

Structural representation of the trees: The structural representation of the different trees is based on a directed acyclic graph. All trees together form a forest. The nodes in this graph represent branchpoints of the trees and the edges correspond to tube elements connecting these branchpoints. For all tubular structures $l^j = \{\mathbf{x}_i^j\}_{i=1}^{o}$ the centerline points $\mathbf{x}_i^j$ with associated tangent direction $\mathbf{t}_i^j$, radius r_i^j, and the flow direction in the tubular structure $d^j \in \{+1, -1\}$ are known. If the flow direction is from the first centerline point of the tube element to the last, we set $d^j = +1$; otherwise $d^j = -1$. In addition, for every tube element the average radius r^j and gray-value I^j is known.

Tree reconstruction and separation: Starting from given tube elements that represent the roots of the different tree structures, the corresponding trees are reconstructed and separated from each other by iteratively merging unconnected tube elements. Therefor, the endpoints of unconnected tube elements $\mathbf{x}_i^j$ are considered as candidates for connection to one of the centerline points $\mathbf{x}_k^l$ of the known trees. Based on geometric properties, possible connections are identified and preferences based on a confidence function are computed and the connection with the highest confidence is inserted into the graph. The procedure is repeated as long as the highest connection confidence stays above a threshold c_{min}. Determination of the set of possible connections and the confidence for a connection are based on above stated flow preservation constraint and primarily utilizes the distance $d = \max\big(0, |\overrightarrow{\mathbf{x}_k^l \mathbf{x}_i^j}| - r_k^l\big)$ and the angles $\alpha^l = \angle\big(\overrightarrow{\mathbf{x}_k^l \mathbf{x}_i^j}, d^l t_k^l\big)$ and $\alpha^j = \angle\big(\overrightarrow{\mathbf{x}_k^l \mathbf{x}_i^j}, d^j t_i^j\big)$ (Fig. 3.1). The following hard constraints have to be fulfilled to form biological reasonable tree structures, and therefore, to determine the set of possible connections:

1. There must not be sharp turns in the flow direction: $\alpha^j \leq \gamma_a$ and $\alpha^l \leq \gamma_a$.
2. The radius must not increase: $r^{path} \leq \gamma_r r^l$, where r^{path} is the smallest radius on the whole path from the root.
3. The connection distance must not be too large: $d \leq \gamma_d r^j$. Incorporation the radius r^j as an additional factor makes the formulation independent of the scale of the actual application domain (e.g. airways of men or animals).

To yield correct connections in case of tangenting or overlapping tubular structures, a combination of distance and angle is used to compute the connection confidence for all possible connections:

$$\mathrm{conf}(\mathbf{x}_i^j, \mathbf{x}_k^l) = e^{-\frac{\alpha^j}{2\rho^2}} \frac{1}{1 + \frac{1}{r^j} d} \tag{3.1}$$

The pair of points $\mathbf{x}_i^j$ and $\mathbf{x}_k^l$ with the highest connection confidence is determined and a linkage path in the image domain is obtained using linear interpolation. The tube element is connected to the corresponding tree and the structural forest description is updated. During this step the flow direction of the newly added tube element of the tree is determined, dependent on the endpoint of the tube element that is connected.

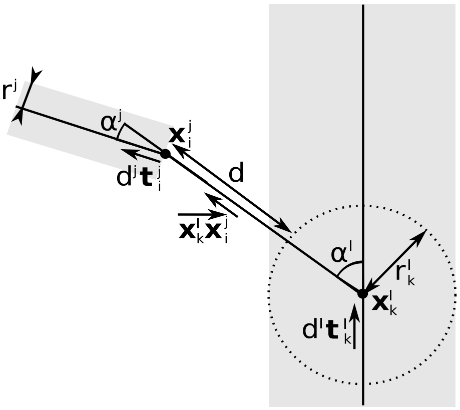

Figure 3.1: Information used for calculation of the confidence function for structural tree reconstruction.

As a note, we want to point that an iterative optimization scheme is utilized here and not a globally optimal optimization method due to the high computational complexity of the resulting problem, such that a globally optimal optimization is generally not applicable. However, Agam et al. [1] were able to solve a similar problem on lung vascular trees in a globally optimal way. But in their application they were able to utilize additional assumptions based on prior knowledge about the lung anatomy.

Linkage path verification: Depending on the application it may be desirable to verify the plausibility of the linkage based on gray value evidence, while for some applications such a verification may not be necessary or even counterproductive (e.g. occluding structures separating parts of a tubular tree structure). In case such a gray value based verification is desired, the gray values of the pixels along the determined path are analyzed to verify the correctness of the link. Therefor, the maximal gray value difference between the path points and the average gray value of the considered tubular structures is determined: $\text{diff} = \max_{\mathbf{x} \in \text{path}} |I(\mathbf{x}) - (I^j + I^l)/2|$. A linkage path with a too large deviation $\text{diff} > \gamma_{\text{diff}}$ may be assumed invalid and discarded. Note, that this step only serves to verify the plausibility of the connection, while the structural information is the main factor for the grouping.

3.3 Image Based Approach

In this section, we present a method for grouping/linkage of identified tubular objects based on image information by utilizing image gradient information and the GVF field obtained from this image gradient information. We used the GVF field already for identification of tubular objects as a replacement for the multi-scale gradient vector computation for detection of tubular structures (Section 2.3). In combination with a tube likeliness measure based on central or offset-medialness functions, the overall approach allows detection of tubular objects at their centerlines showing several advantages compared to conventional multi-scale TDFs. But similar to other TDFs, the method does not produce valid centerline paths in the proximity of junctions or diseases like stenosis where the objects shapes strongly deviates from the typical tubular shape. However, the GVF shows another property that can be used to solve this problem and that has been used for extraction of curve skeletons (CS) from binary segmentations by the skeletonization approach of Hassouna and Farag [53, 54]. In contrast to skeletonization approaches that are based on the distance transformation, the magnitude of the GVF always decreases towards the medial curves independent of the object's shape. This property of the GVF enables the extraction of the centerlines also in case of junctions or plate like structures.

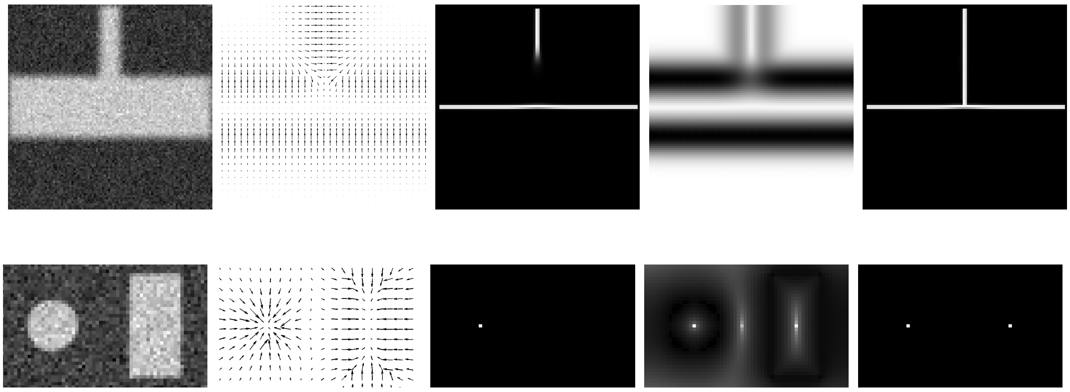
(a) (b) (c) (d) (e)

Figure 3.2: Illustration of the basic idea on 2D cross section profiles of some 3D structures. Top row: cross section T-junction of a tubular object; bottom row: structures with a circular cross section (left) and a strong deviation from a circular cross section (right). From left to right: original dataset, GVF, derived tube-likeliness, derived medialness $\lambda(\mathbf{x})$, extracted CS.

Fig. 3.2 illustrates this property and the basic idea for our image based grouping/linkage on some 2D cross sections of 3D structures. In these images the GVF field, the TDF response (using the central medialness function as described in Section 2.3.1), and the derived medialness measure based on the GVF magnitude that can be utilized for the grouping/linkage in regions with significant deviation from a typical tubular shape, is shown. As a measure of medialness Hassouna and Farag [53, 54] applied the following weighting of the GVF magnitude $|V(\mathbf{x})|$:

$$\lambda(\mathbf{x}) = \mathbf{1.0} - \left(\frac{|\mathbf{V}(\mathbf{x})| - \mathbf{min}|\mathbf{V}(\mathbf{x})|}{\mathbf{max}|\mathbf{V}(\mathbf{x})| - \mathbf{min}|\mathbf{V}(\mathbf{x})|} \right)^{\mathbf{q}} \tag{3.2}$$

with $0.0 < q < 1.0$ in combination with their levelset based skeletonization approach. As can be seen from the medialness images, the GVF magnitude decreases with increasing distance from the surfaces of the structures. This property is independent of the size of the structures and it is also preserved in areas where the tubes do not show a circular cross-section. For our purpose, we utilized the weighting of the GVF magnitude as applied by Hassouna and Farag only for visualization in Fig. 3.2(d), while for the actual extraction a similar but simpler medialness measure is used: $M(\mathbf{x}) = \mathbf{1} - |\mathbf{V}(\mathbf{x})|$. From the medialness images, the medial curves can be extracted as the height-ridges using the ridge traversal procedure presented in Section 2.4.

For our image based grouping and linkage, we search for connecting paths between the identified tubular structures in the medialness map $M(\mathbf{x})$. Therefor, starting from each endpoint of each tubular structure the associated height-ridge in the medialness map is traversed in the direction pointing away from the tubular structure into the direction where the shape strongly deviates from the typical tube shape. The traversal is stopped when the medialness falls below a given threshold m_{min} or a centerline point of a tubular structure is found. The extracted traversal path is analyzed if it forms a valid connection/linkage path and added as a link between the tubular structures if it is valid. A traversal path in the medialness map is assumed as a valid link if the traversal ends at another tubular object and if the gray values along the linkage path do not change too much; therefor the maximal gray value difference $\mathrm{d} = \max_{\mathbf{x} \in \mathrm{path}} |I(\mathbf{x}) - I_{tube}|$ between the linkage path points and the average gray value I_{tube} of the considered tubular structure has to stay below a given threshold $\mathrm{d} < \gamma_{\mathrm{diff}}$.

In this way the tubular structures are grouped and linked together based on image information. The overall approach allows for extraction of complete CSs from tubular networks directly from gray value images by utilizing the same GVF field two-fold, for a bottom-up identification of tubular structures and for an extraction of medial curves also in the regions that strongly deviate from the typical tubular shape.

3.4 Experiments

In this section, we study the behavior of the previously presented grouping and linkage methods (Section 3.2 and 3.3) with respect to the structural correctness of the tubular tree structures and with respect to the accuracy of the extracted curve skeletons.

3.4.1 Structural Correctness

To study properties of the method's abilities to obtain the correct structure, both methods were applied for the task of airway tree reconstruction and liver vascular tree reconstruction/separation (Figs. 3.3 and 3.4). The tubular structures were obtained from the datasets using the GVF-based TDF with the offset medialness function as presented in Section 2.3.2. Organ masks were utilized to discard tubular structures in the datasets. For the structural tree reconstruction method (Section 3.2), the required root elements were selected manually.

Ability to separate multiple interwoven tubular tree structures: Fig. 3.3 show the results on a contrast enhanced liver CT dataset. Fig. 3.3(a) and (b) show the original dataset and the extracted tubular structures respectively. The dataset contains the portal vein tree and the hepatic vein trees. Both of them have a comparable gray value in the datasets, and both appear overlapping in some areas due to partial voluming. The dataset further shows a tumorous region adjacent to one of the vessels. As can be seen from the extracted tubular structures, the TDF was able to suppress the tumorous region, however, also the vessel adjacent to the tumor was not identified. Additionally, the centerlines between the tubular structures break up in some areas (e.g. branching areas). Fig. 3.3(c) and (d) show the results of the image based and the structure based approach, respectively, showing all tubular structures identified as part of the portal vein tree in blue. As can be seen, the image based approach was able to close the gap in proximity of the tumor, but it was not able to distinguish between the two vascular tree structures as both overlap in the image domain. Using the presented structure based approach avoids this problem and allows for a correct reconstruction and separation of the vascular trees.

Impact of flow direction information on structural correctness: Contrary to other structure based approaches that perform a grouping of unconnected tubular structures into complete tree structures, our method incorporates flow direction information (Section 3.2). To assess the impact of this additional information on robustness, we re-

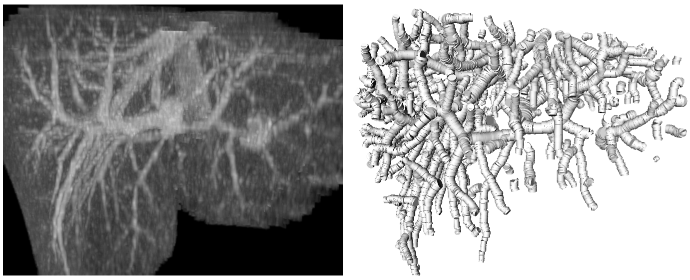

(a) MIP of dataset.

(b) Extracted tubular structures.

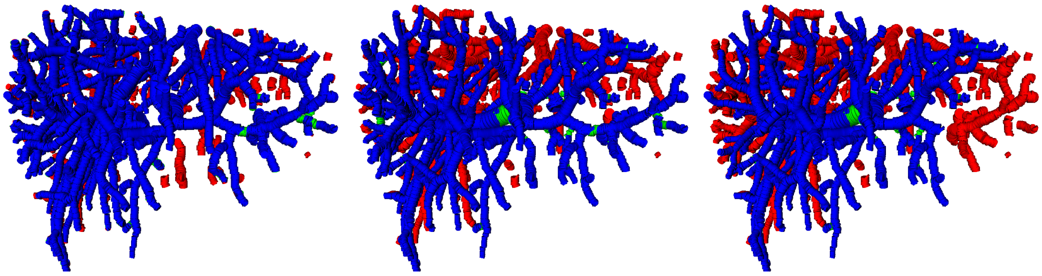

(c) Image based grouping/linkage.

(d) Structure based grouping/linkage.

(e) Structure based grouping/linkage without angle information.

Figure 3.3: Grouping and linkage of tubular structures applied to a liver CT containing multiple interwoven tubular tree structures. Top row: dataset and identified tubular structures. Bottom row: grouping and linkage result for the two methods showing linkage paths (green), identified tubes connected to the portal vein tree by the grouping (blue), and identified tubes not connected to the portal vein tree (red).

moved all part of the structural approach that utilizes flow direction (angle) information. A result of applying this simpler algorithm on this dataset is shown in Fig. 3.3(e), where also misconnections between the vascular trees can be observed resulting in a grouping of major part of the portal vein tree as part of a hepatic vein tree. An evaluation of this simpler structure based approach and the approach as presented in Section 3.2 on 5 clinical liver CT datasets showed, that the number of misconnections can be reduced significantly by utilizing flow direction information. Without using flow direction information 23 misconnections occurred, while when using flow direction information only one misconnection occurred. As a basis for these claims, we used evaluated segmentation results that were verified by a trained radiologist (see Section 5.3.2). Thus, utilizing flow direction information in the structural approach enhances the robustness in case of multiple overlapping tubular tree structures considerably.

Behavior in case of disturbances and significant deviations from a typical tubular shape: Fig. 3.4 shows an airway tree containing a large tumor that infiltrates the airways. The tumor blocks the connection to one of the airway branches completely and leads to a stenosis in another airway branch (Fig. 3.4(a) and (b)). As can be seen from the extracted tubular structures (Fig. 3.4(c)) both parts were not identified by the TDF. The result of applying the structure based and the image based grouping/linkage approaches on this datasets results in the extracted structures shown in Fig. 3.4(d) and (e). The image based approach was able to extract a valid link in case of the stenosis. However, it was not able to identify a connection to the completely blocked airway branch. The structure based approach on the other hand was able to cope with all these severe disturbances.

3.4.2 Centerline Accuracy

In this section, we study the achievable centerline accuracy with previously presented grouping and linkage methods. We present results achieved on clinical datasets and compare them quantitatively and qualitatively to other methods with similar objectives. We will show two things. First, our presented image based approach that utilizes the properties of the GVF (Section 3.3) is able to extract medial curves that stay centered in complicated cases where conventional TDFs and non-image based linkage strategies have problems. We do this by comparing the results achieved with the GVF-based approach to results achieved with the structure based approach and to the results achieved with another approach by Krissian et al. [18, 70] that extracts medial curves directly from the gray value images . Second, the accuracy of the centerlines extracted with the GVF-based approach is comparable to those achieved with pure skeletonization approaches from accurate segmentations. We do this by comparing the results of our GVF-based approach to the skeletons extracted with three different skeletonization approaches [15, 53, 110] from known gold standards (available segmentations of the interesting structures).

Datasets and methods: The two clinical datasets we use for evaluation show an airway tree (see Fig. 3.5) and a contrast CT of an aorta containing a severe stenosis due to calcification (see Fig. 3.6). Segmentations of the bronchial tree and the aorta were available. The segmentation of the aorta follows the interior of the aorta excluding the calcifications.

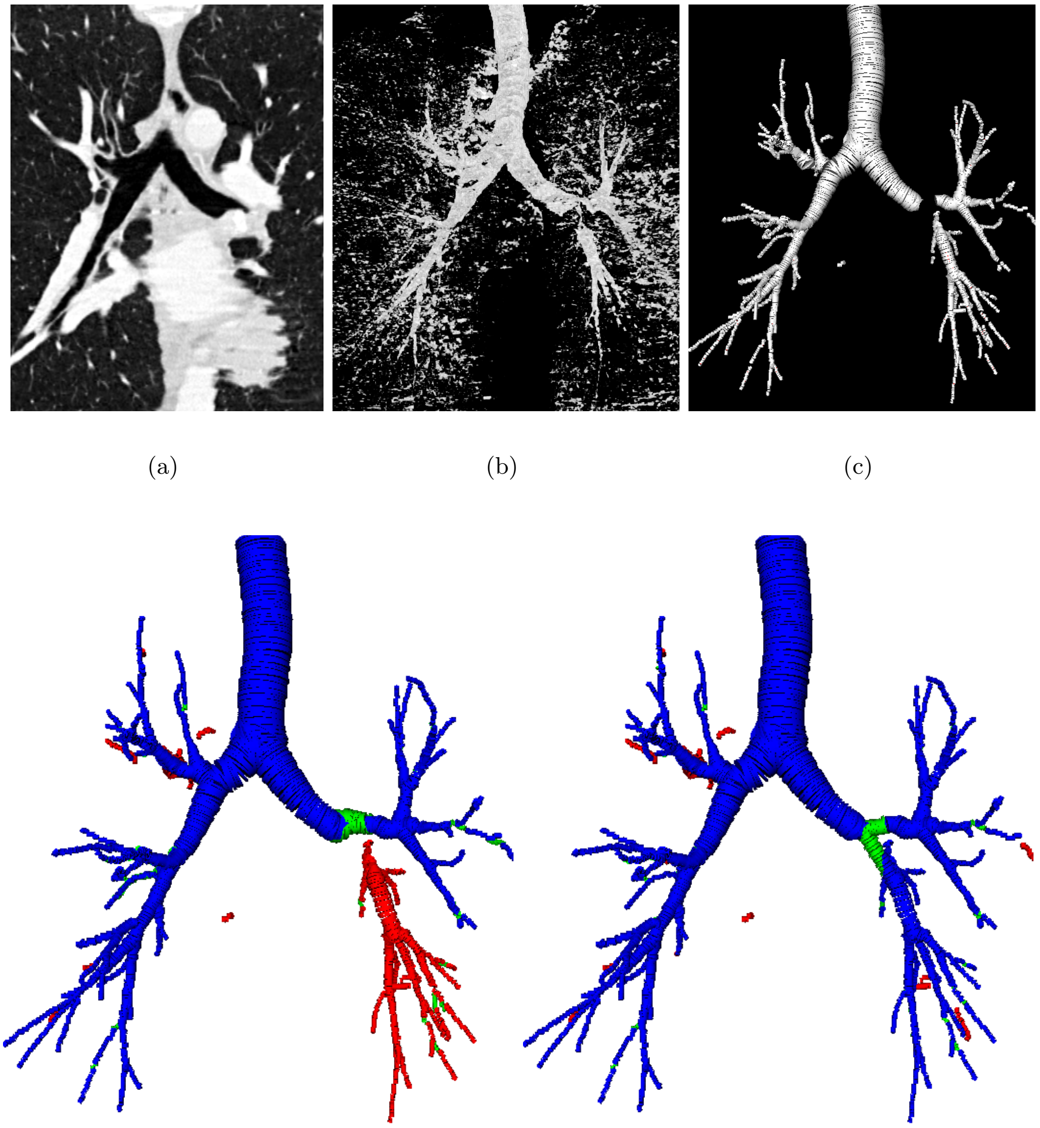

(a) (b) (c)

(d) Image based grouping/linkage. (e) Structure based grouping/linkage.

Figure 3.4: Grouping and linkage of tubular structures from an airway tree containing a tumor that infiltrates one airway branch completely. Note the gap between the airway branches at the tumor region. Top row: dataset and identified tubular structures. Bottom row: grouping and linkage result for the two methods showing linkage paths (green), identified tubes connected to the trachea by the grouping (blue), and identified tubes not connected to the trachea (red).

The approaches we used for comparison are three sophisticated skeletonization approaches (using binary segmentations) and one method that derives the medial curves

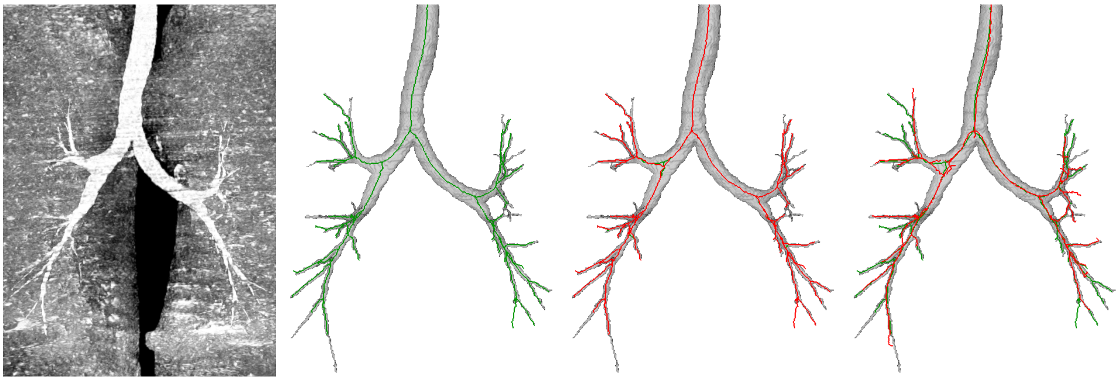

(a) Volume rendering of dataset.

(b) GVF-based grouping and linkage (Section 3.3).

(c) Structure based grouping and linkage (Section 3.2).

(d) Mutliscale tube detection and simple linkage.

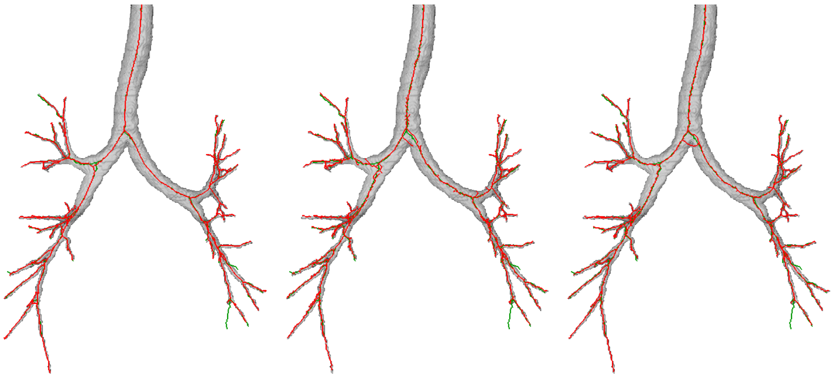

(e) Hassouna's skeletonization approach.

(f) Bouix's skeletonization approach.

(g) Palagyi's skeletonization approach.

Figure 3.5: Curve skeletons of an airway tree. Green: Result of GVF-based grouping and linkage (Section 3.3). Red: Other approaches.

directly from the gray value image. The skeletonization approaches are that of Hassouna et al. [53–55], Bouix et al. [15], and Palagyi et al. [110]. Hassouna's approach also uses the GVF similarly to our approach; the other two methods were specifically developed for tubular objects. As an alternative method that tries to extract centerlines directly from gray value images we decided to use a combination of the methods of Krissian et al. [70] (for a bottom-up detection of tubular structures) and Bullitt et al. [18] (for grouping the single tubular objects into tree structures and an extraction of the complete CS). For all approaches the authors default parameters were used. For our grouping/linkage meth-

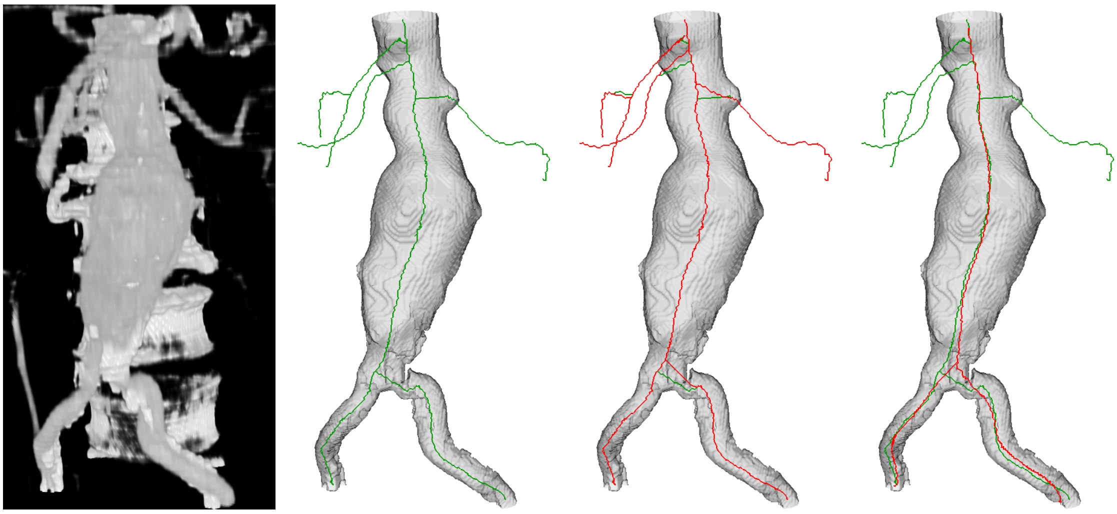

(a) Volume rendering of dataset.

(b) GVF-based grouping and linkage (Section 3.3).

(c) Structure based grouping and linkage (Section 3.2).

(d) Mutliscale tube detection and simple linkage.

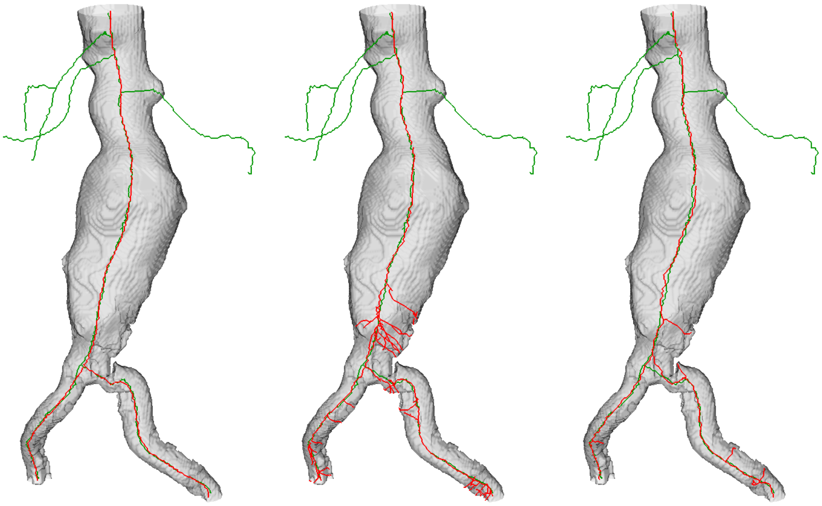

(e) Hassouna's skeletonization approach.

(f) Bouix's skeletonization approach.

(g) Palagyi's skeletonization approach.

Figure 3.6: Curve skeletons of an aorta containing a severe stenosis due to calcification. Green: Result of GVF-based grouping and linkage (Section 3.3). Red: Other approaches.

ods, the tubular structures were obtained from the datasets using the GVF-based TDF with the offset medialness function as presented in Section 2.3.2. For the structural tree reconstruction method (Section 3.2) the required root elements were selected manually.

Qualitative Results: In Figs. 3.5 and 3.6, the results achieved with our methods and the other methods on the clinical datasets are shown. Enlarged subwindows in regions around a junction and stenosis are shown in Figs. 3.7 and 3.8, respectively.

The airway dataset (Figs. 3.5 and 3.7) demonstrates that the results of the different methods in the case of a single perfectly tubular structure are almost identical. Only the method utilizing the multi-scale tube detection filter shows some deviation. But at one of the junctions that shows a larger variation from the typical shape (it becomes more plate like) some approaches had problems to produce valid centerlines. In particular, the combined approach of Krissian and Bullit had problems since this combination does not guarantee centered paths in junction areas. Both our grouping/linkage methods show a reasonable behavior in this case and the centerlines overlap in the tubular parts completely as both are based on the same extracted tubular structures. Thus, the results only deviate in the branching areas. The completeness of the resulting CS regarding the structure of the trees achieved with the GVF-based approach is also comparable to that of the gold standard segmentation.

(a) GVF-based grouping and linkage.

(b) Structure based grouping and linkage (Section 3.3).

(c) Mutliscale tube detection and simple linkage (Section 3.2).

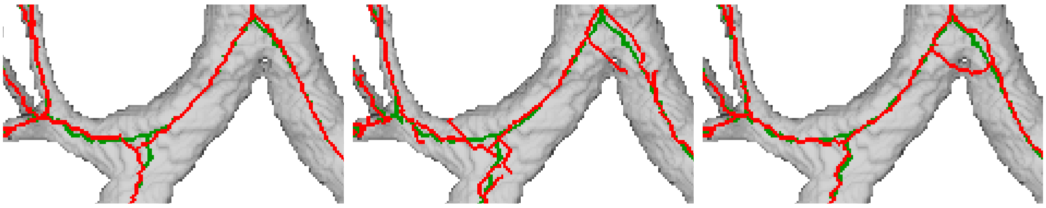

(d) Hassouna's skeletonization approach.

(e) Bouix's skeletonization approach.

(f) Palagyi's skeletonization approach.

Figure 3.7: Enlarged subwindow showing curve skeletons of an airway tree. Green: Result of GVF-based grouping and linkage (Section 3.3). Red: Other approaches.

On the aorta dataset (Fig. 3.6), the different methods show major differences at the junction with the stenotic area (Fig. 3.8). Krissian's multi-scale TDF was influenced by the calcification and thus the resulting centerline moved far away from the desired position. The GVF-based TDFs on the other hand are not sensitive to such kinds of disturbances. In proximity of the stenosis where the TDF filter was not able to identify a tubular structure, the GVF-based grouping/linkage was able to extract a medial curve that stayed centered with a quality comparable to that of the skeletonization approaches. The simpler structure-based grouping/linkage methods on the other hand closed the gap between the tubular structures along a straight line, showing a large deviation from a high quality skeleton. The skeletonization approaches of Bouix and Palagyi showed some sensitivity to surface noise in the gold standard segmentation and produced additional centerlines. The authors themselves mention this behavior and these spurious branches can be removed by appropriate pruning strategies.

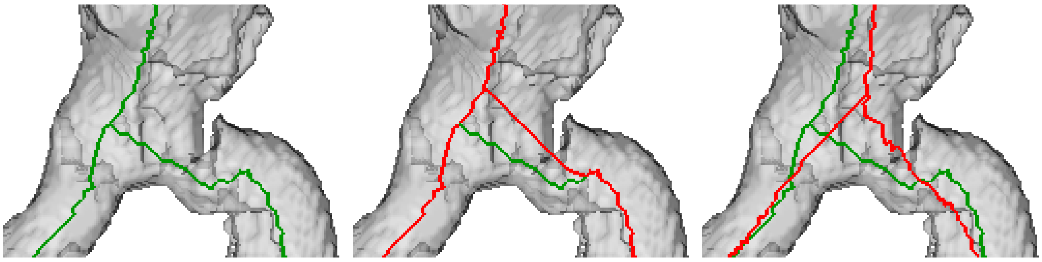

(a) GVF-based grouping and linkage (Section 3.3).

(b) Structure based grouping and linkage (Section 3.2).

(c) Mutliscale tube detection and simple linkage.

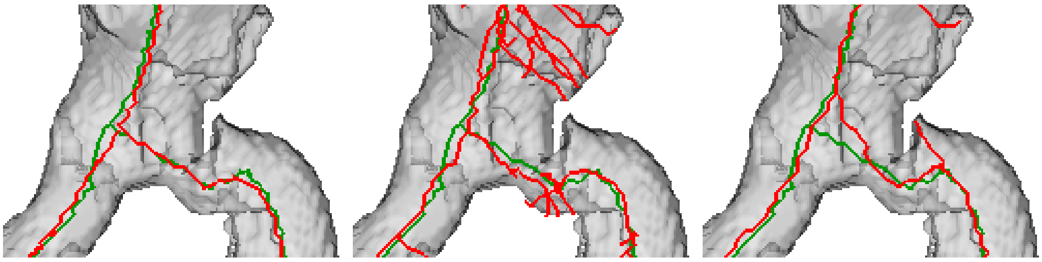

(d) Hassouna's skeletonization approach.

(e) Bouix's skeletonization approach.

(f) Palagyi's skeletonization approach.

Figure 3.8: Enlarged subwindow showing curve skeletons of an aorta containing a severe stenosis due to calcification. Green: Result of GVF-based grouping and linkage (Section 3.3). Red: Other approaches.

Quantitative Results: The quantitative comparison of the centerline accuracy is based on the average centerline distances between the different methods. To make the CSs comparable, the skeletons obtained with the methods of Bouix and Palagyi were pruned and only branches detected by all methods (the segmentation methods and the TDF methods) were considered. Tables 3.1 and 3.2 summarize the average centerline distances between the different methods for the two datasets. All the methods are quite comparable (except the results achieved with the combined approach of Krissian and Bullitt). Our two grouping/linkage methods utilized the same tubular structures, thus only showing small differences. But also notable is the small difference between our GVF-based method and Hassouna's approach on the airway tree, but this may be explained since this method is also based on the GVF. As these results show, the achieved centerline accuracy of our GVF-based tube detection and grouping/linkage method is comparable to the variation found between different skeletonization approaches. Note that all the skeletonization approaches use the same binary segmentations while our method does not know this gold standard. This shows that our approach is able to extract CSs of comparable quality directly from the gray value images.

Table 3.1: Average centerline distances in voxels (aorta).

		M1	M2	M3	M4	M5	M6
GVF TDF + GVF linkage	M1	–	0.01	0.66	0.62	0.79	1.49
GVF TDF + structure linkage	M2	0.03	–	0.69	0.58	0.81	1.38
Hassouna	M3	0.63	0.68	–	0.60	0.72	1.14
Bouix	M4	0.59	0.58	0.63	–	0.78	1.58
Palagyi	M5	0.78	0.81	0.75	0.80	–	1.53
Krissian + Bullitt	M6	1.61	1.45	1.17	1.70	1.60	–

Table 3.2: Average centerline distances in voxels (bronchial tree).

		M1	M2	M3	M4	M5	M6
GVF TDF + GVF linkage	M1	–	0.08	0.24	0.41	0.40	0.58
GVF TDF + structure linkage	M2	0.04	–	0.24	0.44	0.40	0.66
Hassouna	M3	0.22	0.23	–	0.37	0.34	0.72
Bouix	M4	0.47	0.42	0.36	–	0.45	0.67
Palagyi	M5	0.44	0.47	0.33	0.44	–	0.70
Krissian	M6	0.59	0.67	0.53	0.57	0.66	–

3.5 Dicussion and Conclusion

In this chapter, we were concerned with the grouping and linkage of tubular structures into complete tree structures. Therefor, two methods have been presented: (a) a structure-based approach has been presented (Section 3.2) that is capable of grouping/separating tubular structures in case of multiple interwoven tree structures into valid tree structures and (b) an image based methods has been presented (Section 3.3) for extraction of centered linkage paths. In Section 3.4 we studied these two methods in several examples showing some of their properties.

As shown by these examples, the GVF-based approach for identification of tubular objects and for extraction of linkage paths between these tubular objects allows us to extract high quality curve skeletons directly from gray value images. This approach combines the advantages of a bottom-up tube detection filter with the GVF's ability for extraction of medial curves, also in cases where the tube detection is perturbed due to larger deviations from the typical tube shape such as furcations, stenosis, or aneurysms. The presented image based linkage approach allows for extraction of medial curves also in these areas. We showed that the accuracy of the resulting centerlines is comparable to that achieved with state of the art skeletonization approaches that are all based on the same known segmentations. Thus, the resulting CSs are directly applicable for tasks requiring high quality skeletons and this supersedes the need to deal with segmentations and skeletonizations in these applications.

However, as shown in the experiments, pure image based methods are not capable of handling disturbances such as overlapping tubular tree structures or cases where parts of the tubular tree structure are not identifiable in the image domain (e.g. the tumor in case of the airway tree; see Fig. 3.4). In such a case, only some kind of centerline interpolation can be utilized as done with our structure based approach. As we showed in the experiments, the presented structure based approach allows a separation of interwoven overlapping tubular tree structures and handling of various kinds of disturbances, but it cannot guarantee a centered path in these disturbed regions.

Also a combination of the two approaches could be applied, using the image based linkage path extraction in cases of deviations from a tubular shape and a linear centerline interpolation in case of imaging artifacts or partly overlapping tubular tree structures. Therefor the validity of the centerline paths extracted with the image based method should be verified based on structural properties and additional linear centerline paths added in case the structure based method requires a link between two tubular structures. This would combine the advantages of both approaches.

Chapter 4

Tube Segmentation

Contents

4.1 Introduction

In the last two chapters, we presented methods for the extraction of structural representations of tubular tree structures. The derived representations consist of centerlines/skeletons usually associated with a radius and tangent direction estimate for each centerline point. Such a representation can be seen as a segmentation result [18, 68], however, this information does not accurately represent the actual surfaces of the tubular objects. The known structures could be utilized as a good initialization for a segmentation method (e.g., levelsets) to obtain more accurate segmentations. However, most segmentation methods do not necessarily preserve the topology of the already known tree structure as the methods may still show leakage (additional branches in the tree) or holes/gaps in the segmentation results (unconnected branches in the tree). In this chapter, we are concerned with methods to obtain accurate segmentations related to already known tubular structures that make use of the already known information in such a way that the topology is preserved.

Only a few methods in the literature have addressed the issue of utilizing known structural information to obtain accurate segmentations of tubular tree structures in a topology preserving way. Deformable models are the most common approach [43, 103, 104, 151, 165, 172]. In very recent works, approaches based on graph-cuts [127] and optimal surface finding [32] were applied.

In the last few chapters, we presented methods utilizing properties of the GVF for detection of tubular objects (Section 2.3) and for grouping/linkage of tubular objects into tree structures (Section 3.3). However, the GVF was originally presented to guide snake based segmentations [168]. But properties of the GVF (or similar gradient diffusion methods) have also been used to generate voxel accurate 2D and 3D segmentations without using snakes [22, 82, 129, 174]. For example, Li et al. [80] used a gradient flow tracking in the GVF field in combination with a locally adaptive thresholding scheme based on gray value statistics to segment blob like 3D structures. But to our knowledge, none of the so far presented methods is directly applicable for segmentation of tubular structures.

In the next two sections, we present two different methods to obtain accurate segmentations associated with already known tubular structures that preserve the topology. Therefor, two methods are presented. The first utilizes the same GVF field as utilized for the tube detection approach (Section 2.3) and the second utilizes a graph cut based approach that performs a segmentation in a globally optimal fashion.

4.2 Inverse Gradient Vector Flow Tracking

To achieve an accurate segmentation of the tubular structures identified in a GVF field by using the approach from Section 2.3, we present in this section a method that can be directly applied to the same already obtained GVF field. As we have seen in Section 2.3.3, the GVF-based approach may be adapted to varying background conditions. In case of varying background conditions and arbitrary edge types, the initial vector field is obtained from a gradient magnitude image, while for tubular structures surrounded by the dark/bright background the initial vector field for the GVF is obtained directly from the gray value images. For the tube segmentation method presented in this section, we also have to distinguish between these two cases.

Considering the GVF field $V(\mathbf{x})$ of a tubular structure as illustrated in Fig. 4.1, all the vectors flow towards the centers of the tubular structures, which correspond to the extracted centerlines of the tubular structures (in case of tubular objects). By following the direction $V^n(\mathbf{x}) = V(\mathbf{x})/|V(\mathbf{x})|$ of the vectors, each voxel can be assigned to a neighboring voxel and a path can be tracked for each voxel of the tubular structure to its centerline. Based on this assignment, the voxels of tubular structures associated with the individual centerlines can be segmented by following the gradient flow tracking path in the inverse direction. In case the GVF field was obtained from a gradient magnitude image, it is sufficient to track all these paths until their end, because at the boundaries the vectors point into the opposing direction (Fig. 4.1(f)). However, in case the GVF field was obtained directly from the gray value image, an additional criterion is necessary. The magnitude of the GVF $M(\mathbf{x}) = |V(\mathbf{x})|$ increases until the actual boundary is reached (Fig. 4.1(c)) from where on it starts decreasing.

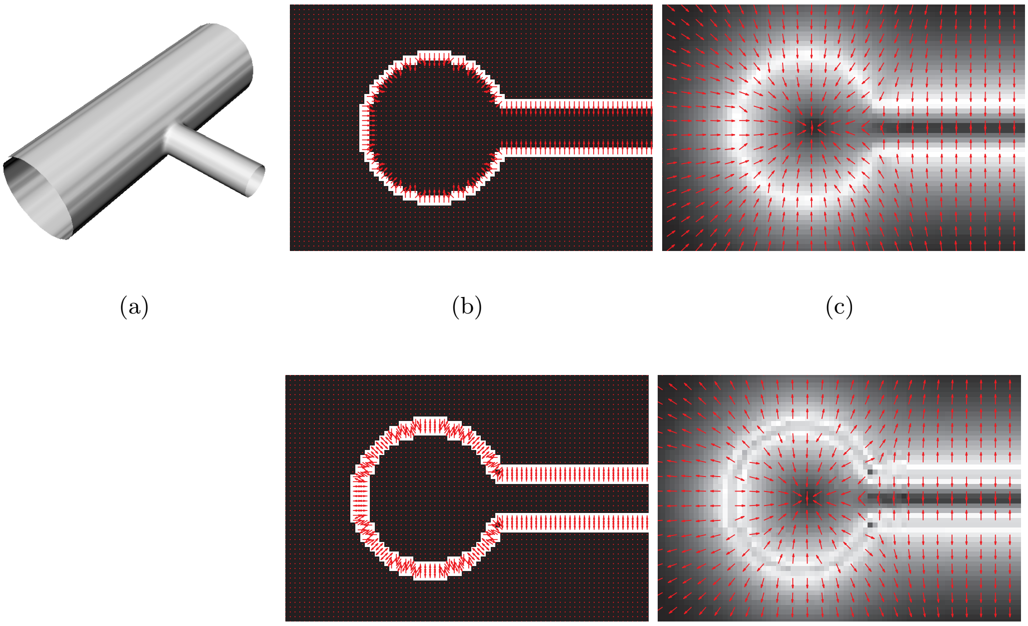

(a) (b) (c)

(e) (f)

Figure 4.1: Illustration of properties of the GVF using a 2D cross section of a 3D branching tubular structure. Top row: vector fields for bright/dark structures. Bottom row: vector fields based on gradient magnitude image. (a) Branching 3D tubular structure. (b) and (e) Initial vector fields $F^n(\mathbf{x})$ (gray-value: vector magnitude; arrow: vector direction). (c) and (f) Resulting GVF fields $V(\mathbf{x})$ (gray-value: vector magnitude; arrow: vector direction).

Based on these properties of the GVF, the tubular structures are segmented. Therefor, starting from the points at the tubes center, neighboring voxels fulfilling above criteria are merged iteratively to generate a segmentation, using Algorithm 2 in case the GVF was obtained directly from the gray value image, and using Algorithm 3 in case the GVF was obtained from a gradient magnitude image. In this way, the voxels associated with the centerline of a tubular structure are segmented.

Algorithm 2 Inverse gradient flow tracking tube segmentation for GVF obtained from gray value image.

```
input: GVF field $V(x)$ with direction $V^n(x)$ and magnitude $M(x)$
input: centerline points $C = \{x_1, x_2, \ldots, x_n\}$
set $S \leftarrow C$
queue $Q \leftarrow C$
while $Q \neq \{\}$ do
  $x \leftarrow$ extract($Q$)
  for each voxel $y \in Adj26(x)$ do
    if $y \notin S$ and $M(y) > M(x)$ and $argmin_{z \in Adj26(y)} \langle V^n(y), \overrightarrow{yz} \rangle = x$ then
      $S \leftarrow S \cup \{x\}$
      $Q \leftarrow Q \cup \{y\}$
    end if
  end for
end while
output: segmented tube voxels $S$
```

Algorithm 3 Inverse gradient flow tracking tube segmentation for GVF obtained from gradient magnitude image.

```
input: GVF field $V(x)$ with direction $V^n(x)$ and magnitude $M(x)$
input: centerline points $C = \{x_1, x_2, \ldots, x_n\}$
set $S \leftarrow C$
queue $Q \leftarrow C$
while $Q \neq \{\}$ do
  $x \leftarrow$ extract($Q$)
  for each voxel $y \in Adj26(x)$ do
    if $y \notin S$ and $argmin_{z \in Adj26(y)} \langle V^n(y), \overrightarrow{yz} \rangle = x$ then
      $S \leftarrow S \cup \{x\}$
      $Q \leftarrow Q \cup \{y\}$
    end if
  end for
end while
output: segmented tube voxels $S$
```

4.3 Graph Cut Based Tree Segmentation

In this section, we present an approach to accurately delineate the boundary of tree structures in a globally optimal manner using a graph cut segmentation approach [17]. The method incorporates the gathered information about structure (skeleton and estimated radius) as a shape prior to guide the segmentation process.

The actual segmentation is constrained to an image region in proximity of the expected surface by defining object and background seed regions as shown in Fig. 4.2. Therefore, the information about centerline point locations $\mathbf{x}_i^j$ and associated radii r_i^j are used to calculate the signed distance to the shape prior (tube) surface $D_{surface}(\mathbf{x})$ and the distance to the closest centerline point $D_{centerline}(\mathbf{x})$. Both distance maps are computed using a fast marching method which is an efficient way to solve the Eikonal equation $|\nabla T(\mathbf{x})|F = 1$, where $T(\mathbf{x})$ is the arrival time at point $\mathbf{x}$ of a front moving with speed F. Assuming that the front starts at the centerline points $\mathbf{x}_i^j$ at time $T_0(\mathbf{x}_i^j) = -r_i^j$ and the speed is constant (i.e. $F = 1$), the solution gives the required distance map $D_{surface}(\mathbf{x})$, whose zero level set represents the estimated surface. All points inside the tube are assigned negative values, all points outside the tube positive values. Similarly, the distance map of the centerlines, $D_{centerline}$ is calculated by using $T_0(\mathbf{x}_i^j) = 0$. Based on the so obtained distance maps $D_{surface}(\mathbf{x})$ and $D_{centerline}(\mathbf{x})$, the object ($D_{surface}(\mathbf{x}) < -d_m$ or $D_{centerline}(\mathbf{x}) < d_{min}$) and background seed regions ($D_{surface}(\mathbf{x}) > d_m$) are defined.

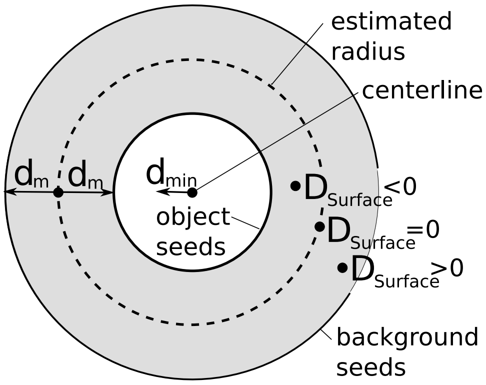

Figure 4.2: Shape prior for the constrained graph cut segmentation.

The objective of the graph cut segmentation step is to find the optimal surface that separates the object from the background seed regions. This is done by finding a closed surface S in between, whose associated energy $E(S) = \oint_S g(\mathbf{x})d\mathbf{x}$ is minimized. The term g with $g \geq \epsilon > 0$ represents the costs and is based on edge information. A globally optimal solution to a discretized formulation of this minimization problem is determined using the graph cut algorithm [17]. Therefore, the voxels of an image are represented as nodes of a graph. Nodes representing adjacent voxels in the image are connected by an edge with associated costs $g(\mathbf{x})$ (the costs are computed as the average costs of the values computed at the discrete voxels). The utilized cost term $g(\mathbf{x})$ incorporates the gradient magnitude $|\nabla G_\sigma \star I|$ and a soft shape prior based on $D_{surface}$ that emphasizes edge information in proximity of the expected tube surface:

$$g(\mathbf{x}) = e^{-\frac{|\nabla G_\sigma \star I(\mathbf{x})|^2}{2\sigma_{edge}^2}} \left(1 - \alpha e^{-\frac{D_{surface}(\mathbf{x})^2}{2\sigma_{shape}^2}}\right) \tag{4.1}$$

where $0 \leq \alpha \leq 1$ can be used to control the influence of the shape prior. σ depends on the image noise level, while σ_{edge} depends on the contrast and is application specific. The value of σ_{shape} depends on the maximally expected variation from a perfectly tubular shape.

4.4 Experiments

In this section we study the behavior of our previously presented tube segmentation methods with respect to their robustness against variations from a standard cylindrical tubular shape and disturbances in the image. Therefor we present qualitative and quantitative results achieved on clinical datasets showing such variations.

Datasets and methods: The datasets we use for evaluation are an airway tree (Fig. 4.3 and 4.5) and four pathological abdominal aortas in contrast enhanced CT datasets (Fig. 4.4). The aortas had stenosis or aneurysms, as well as calcifications (Fig. 4.4(a)), thus their shape deviated significantly from a standard tubular shape. For each of these abdominal aorta datasets, two semi-automatically generated reference segmentations in image regions around the aneurysms/stenosis were available; one segmentation following the inner aorta wall including the calcifications and one segmentation that excludes the calcifications. The reference segmentations only contain the three branches around the main bifurcation of the abdominal aorta.

The structural representations required for the segmentation methods were obtained using the GVF-based TDF with the offset medialness function (Section 2.3.2) and the GVF-based grouping and linkage method (Section 3.3). However, as the reference segmentations of the aortas only contain the three main branches of the abdominal aorta, the corresponding branches from the structural representations were selected manually and the others were discarded, such that the structures of the resulting segmentations are comparable. For comparison, we also show the shape priors reconstructed from these structural representations by using inverse distance transformations based on the centerlinepoints and radius estimates.

Qualitative results: The airway tree segmentations were obtained for the whole tree structure (Figs. 4.3(d)-(f)) and also for a selected path starting from the trachea leading to one of the distal ends of the airway tree (Fig. 4.3(c) and the green part in Figs. 4.3(d)-(f)). As can be seen from Figs. 4.3(d)-(f), the segmentations associated with the selected path do not leak severely into the side branches of the airway tree. Note that in these areas no edge information is present. With the graph cut based method this is not very surprising as the method utilizes a hard shape prior that avoids leakage, however, the GVF-based method also shows a comparable behavior and no hard shape prior is utilized. This shows some robustness of the GVF-based approach against leakage.

In Fig. 4.5 the segmentation results are shown in axial image slices along the selected path from Fig. 4.3(c). As can be seen, the shape of the airway tree shows larger deviations from a tubular shape and the cross section profiles deviate significantly from a perfectly circular or purely convex shape. While the shape prior still deviates significantly from the actual airway shape, the segmented surfaces obtained with the graph cut and GVF-based methods both show a good correspondence with the image data.

In Fig. 4.4 the segmentation of one of the diseased abdominal aorta datasets is shown. The dataset shows an aneurysm and a severe stenosis due to calcification. The segmentation results for our presented methods are shown in Fig. 4.4(c) and (d), showing a qualitative difference between the two methods. The segmentation result of the graph cut based method seems smoother and includes the calcifications, while the GVF-based method on the other hand excludes the calcifications. With such calcifications two distinct edges can be observed in proximity of the shape prior and the graph cut based method chooses between the two possible edges in a globally optimal way based on the preference given by the soft shape prior. The GVF-based method on the other hand evolves a front from the centerline outwards until the first distinct edge is reached, thus showing a more local segmentation behavior.

We also want to point out that the TDFs were capable of coping with these deviations from a perfectly cylindrical tube shape, although these conditions deviate from the assumptions of the TDFs. This shows that these assumptions are not too restrictive to cope with the deviations found in clinical practice.

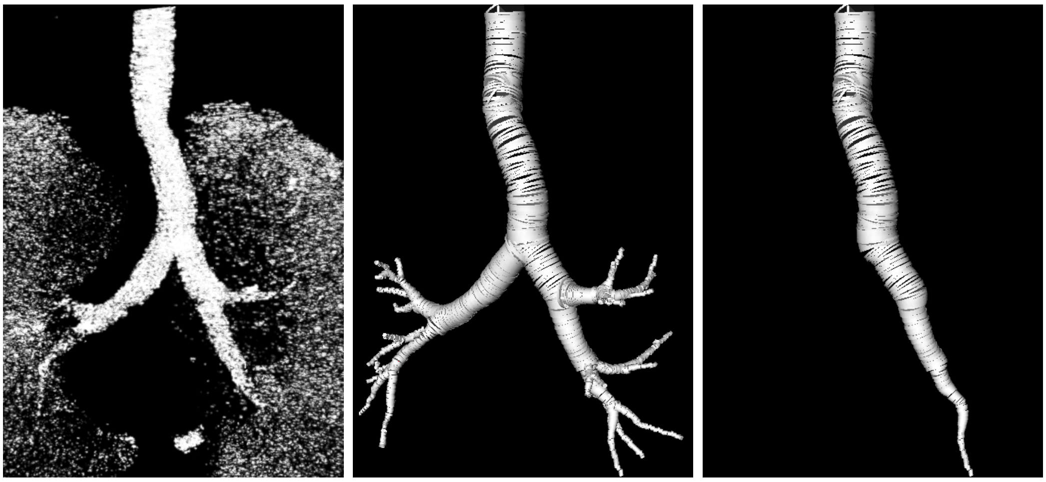

(a) Volume rendering of dataset.

(b) Structure of the whole airway tree.

(c) Structure of a selected centerline path.

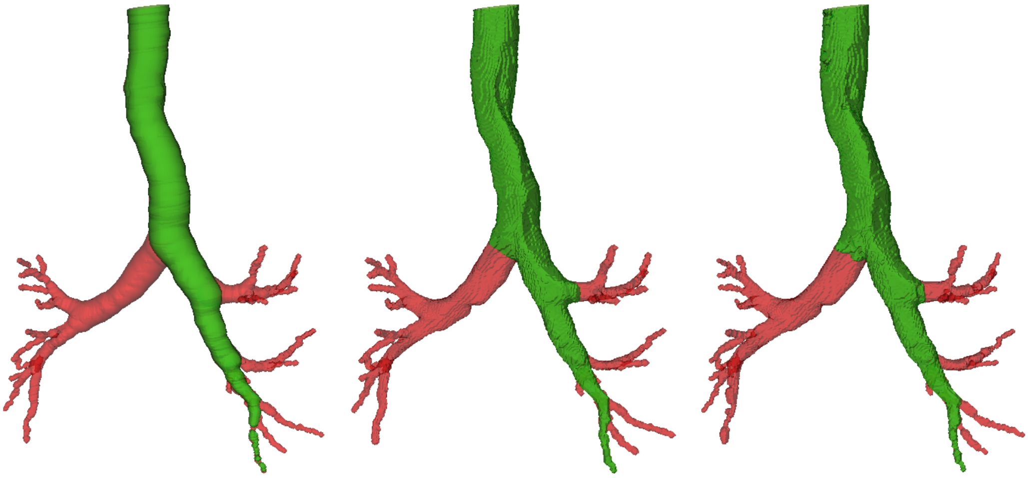

(d) Shape prior based on centerlinepoints and radius estimates.

(e) Graph cut segmentation.

(f) GVF-based segmentation.

Figure 4.3: Segmentation of an airway tree in CT data. Top row: Dataset, reconstructred tree, and a selected centerline path. Bottom row: Segmentations showing the segmentation of the whole tree (red) and the segmentation associated with the selected centerline path (green).

Quantitative results: For quantitative evaluation, the segmentation results were compared with the reference segmentations and some well known segmentation performance measures were obtained. As the graph cut segmentation and the GVF-based method

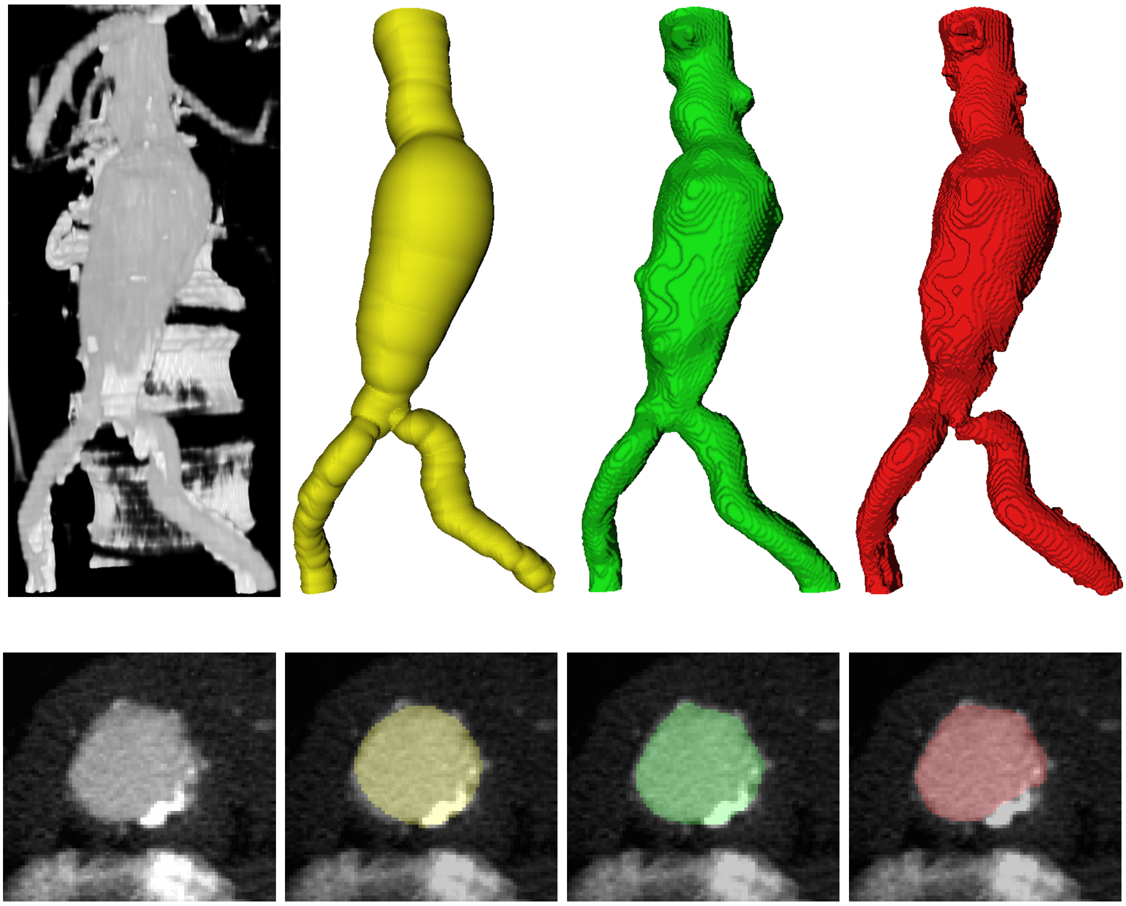

(a) Original dataset.

(b) Shape prior.

(c) Graph cut segmentation.

(d) GVF-based segmentation.

Figure 4.4: Segmentation of a diseased abdominal aorta. Tow row: 3D visualization. Bottom row: slice based visualization.

show a qualitative difference – the graph cut segmentation includes calcifications while the GVF-based method does not – the segmentation results were also compared to reference segmentations including/excluding calcifications. As segmentation performance measures, the segmentation overlap, the unsigned volume error, and the unsigned surface distance are used. Given the segmentation result S and the reference segmentation R, the segmentation overlap Φ is defined as $\Phi = 2V(S \in R)/(V(S)+V(R))$ where V corresponds to the volume, the unsigned volume error Υ is $\Upsilon = |V(S) - V(R)|/V(R)$, and the mean unsigned surface distance error μ_d is the average distance of all surface points of S to the closest point on the surface R. The results on the four datasets are summarized in

Table 4.1. The performance measures seem to be slightly better with the graph cut based segmentation method. However, with both of the methods an average unsigned surface distance of $0.5 \pm 0.1mm$ and $0.6 \pm 0.1mm$, respectively, is achieved, which is lower than the average intra-slice resolution of these datasets.

Table 4.1: Segmentation performance on diseased abdominal aorta datasets.

Error measure	Graph cut segmentation $mean \pm std.dev.$	GVF based segmentation $mean \pm std.dev.$
Segmentation overlap Φ	$95.1 \pm 0.9\%$	$93.5 \pm 0.5\%$
Mean unsigned volume error Υ	$2.1 \pm 1.8\%$	$7.6 \pm 1.6\%$
Mean unsigned surface distance μ_d	$0.5 \pm 0.1mm$	$0.6 \pm 0.1mm$

4.5 Discussion and Conclusion

In this chapter, we were concerned with the segmentation of tubular structures in case of a given rough shape prior. We presented a graph cut based method utilizing a shape prior (Section 4.3) and a GVF-based segmentation method (Section 4.2). In Section 4.4 we studied the robustness and behavior of both methods showing some of their properties.

Both methods were capable of handling cases of abnormal tubular shapes and produced voxel-accurate segmentations in these cases showing a good correspondence with the expected results. Both methods showed robustness against major leakage due to the used shape prior or properties of the GVF, respectively. The main difference between both approaches is that the graph cut segmentation solves the segmentation in a globally optimal way, while the GVF-based approach segments according to the first distinct edge closest to the centerline. Which of the two different behaviors is desired may vary depending on the application.

Regarding computation time, both approaches are computationally inexpensive. The GVF-based segmentation method (Section 4.2) shows similar characteristics as a conventional region grower. With the graph cut based method (Section 4.3) also only image regions in proximity of the tubular structures are considered for computation of the signed distances and the graph cut algorithm itself.

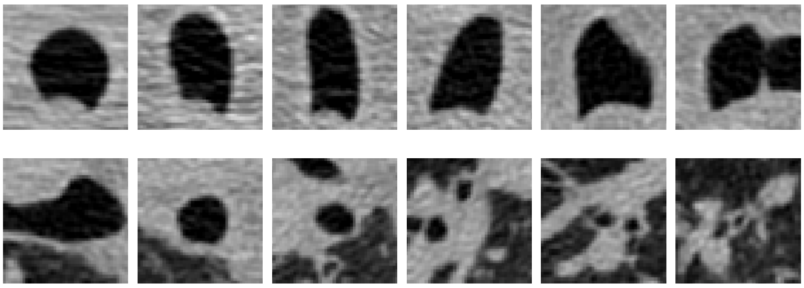

(a) Original data.

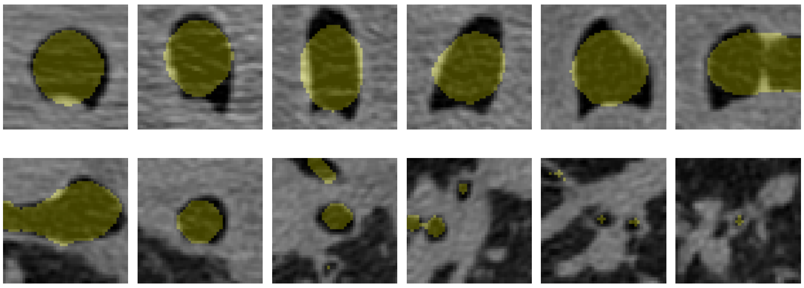

(b) Shape prior based on centerlinepoints and radius estimates.

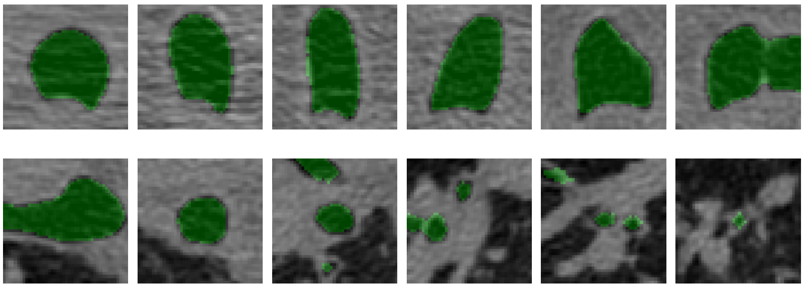

(c) Graph cut segmentation.

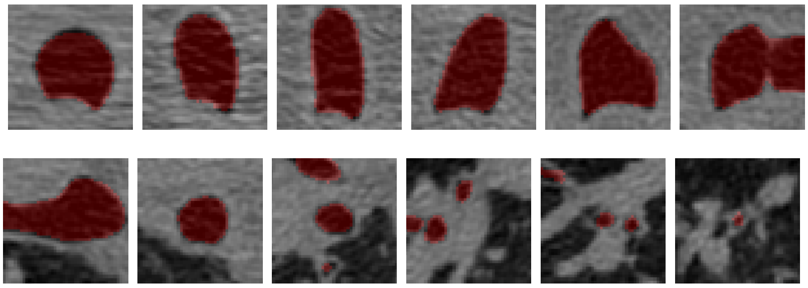

(d) GVF-based segmentation.

Figure 4.5: Segmentation of an airway tree showing segmentations in the axial slices along the centerline path (Fig. 4.3(c)) from the trachea to a distal end of the airway tree.

Chapter 5

Liver Vascular Tree Segmentation

Contents

5.1 Introduction

Planning of liver surgery requires the segmentation and analysis of the livers vascular trees [120] (Fig. 5.1). Basically, the liver has three vessel systems consisting of portal veins, hepatic veins, and hepatic arteries. A segmentation method for surgery planning has to be able to correctly reconstruct and separate these blood vessels trees that can appear overlapping in the image domain due to partial volume effects. The task also requires a segmentation of thin low contrast vessels as this is necessary for an accurate determination of the volume of liver segments [130] and the methods have to cope with tumorous regions and other kinds of disturbances (e.g. imaging artifacts). All this with a minimal amount of user interaction.

Depending on the used imaging protocol, different parts of the liver vasculature can be visible due to contrast enhancement, and some methods in the literature only consider the case where the portal vein tree is contrast enhanced [31, 33, 99], while the task of handling and separating multiple liver vessel trees is only addressed by few authors. Selle et al. [130]

presented a refined region growing approach with an automatic threshold determination as a stopping criterion with a method for separation of overlapping vessel trees based on the analysis of skeletons after segmentation. The authors did not present a performance analysis, but mentioned the need to manually adapt parameters for each dataset. In addition, they utilized a tool to correct errors in the tree separation. Soler et al. [133, 134] presented a combined approach for the segmentation of blood vessels and tumorous regions inside the liver with an additional postprocessing for the separation of the blood vessels trees based on a skeletonization. Both approaches require liver masks for preprocessing or analysis of the dataset, respectively, and both systems approach the separation of the blood vessels trees based on the analysis of extracted skeletons after the actual segmentation step. However, such approaches are sensitive to segmentation errors, especially to missing parts or leakage where the topology of the extracted centerlines is incorrect.

In this chapter, we present an approach that addresses the simultaneous separation and segmentation of different tubular tree structures for the task of liver vasculature segmentation. The method has been evaluated on phantom and clinical datasets, regarding the structural correctness and the surface accuracy of the segmentations. Results are reported, qualitative properties and limits of the method are shown on clinical datasets, and a comparison to results achieved with other methods is provided.

5.2 Method

Our method follows our general approach for segmentation of branched tubular networks as outlined in Section 1.2 to achieve a high robustness against disturbances. It combines three main processing steps to obtain a segmentation and separation of the individual liver vessel trees: a detection and extraction of tubular structures, a tree reconstruction and separation, and a constrained segmentation. An exemplary dataset with intermediate processing results is shown in Fig. 5.1.

Extraction of tubular structures: The TDF of Pock et al. [113] as described in Section 2.2.2 was specifically developed for detection of blood vessels in contrast CT datasets and it showed excellent results in our experiments as shown in Section 2.5.2. Therefore, for extraction of tubular structures, the TDF of Pock et al. [113] is utilized in combination with the height-ridge traversal with hysteresis-thresholding for centerline extraction as described in Section 2.4. To discard short spurious responses of the tube detection filter (noise), all centerlines with an accumulated tube likeliness below t_{conf} are discarded.

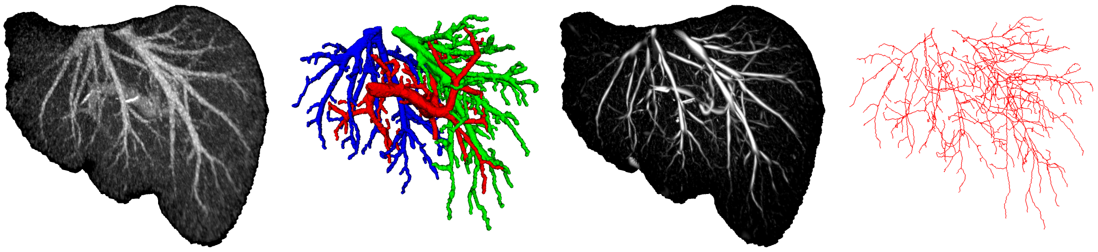

(a) MIP of the dataset using a liver mask.

(b) Final segmentation of all trees.

(c) TDF response.

(d) Extracted tubular structures.

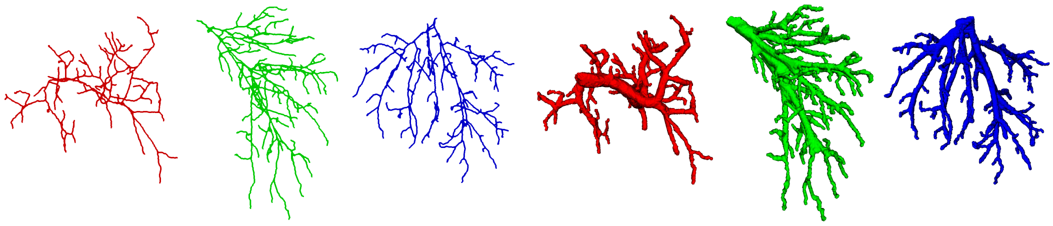

(e) Reconstructed tree structures.

(f) Segmented trees.

Figure 5.1: Segmentation of liver vasculature trees from a contrast CT dataset with intermediate processing results.

The results of the TDF response and the so extracted tubular structures are shown in Fig. 5.1(c) and (d), respectively. The method allows extraction of all tubular objects without false positives due to image noise. However, the centerlines break up at junction areas and the method can not distinguish between parts of the different vessel trees.

Grouping and linkage: To separate the different vessel trees and to close gaps between the individual tubular structures, the structure based grouping and linkage method with the verification of the connection path based on gray value information as presented in Section 3.2 is used. The method requires a seed point for each of the vessels trees at the root of the tubular tree structure as well as the flow direction of each tree. To obtain such seed points in case of a liver masks following observation can be used to specify the tree roots fully automatically. The tubular tree structures enter the organ and branch recursively, whereby their radius decreases and they never exit the organ. Therefore, all tubular structures in the dataset that pass through the surface of the provided organ mask are roots of trees. However, in case such an organ mask is not provided, the roots of the tubular tree structures have to be selected manually. The results of the reconstructed and separated vessel trees are shown for each of the trees in Fig. 5.1(e).

Tube segmentation: To obtain accurate segmentations of the individual blood vessel trees, the graph cut based approach as presented in Section 4.3 is used that utilizes shape priors based on inverse distance transformations of the tubes centerline/radius. This method is slightly adapted to guarantee non-overlapping segmentation results in case of multiple partly overlapping tubular tree structures. The signed distance $D_{surface}(\mathbf{x})$ that is computed based on a fast marching method is obtained for all tubular tree structures simultaneously and $D_{surface}(\mathbf{x})$ determines the assignment of the individual voxels to the different trees. Examplary results of final liver vasculature tree segmentations are shown in Fig. 5.1(f) separately for each tree and in Fig 5.1(b) for all trees together.

Parameters: Following set of parameters is used to process the datasets. The tube detection is performed on 9 radius steps on a linear scale between radii 0.5 mm and 8.5 mm with $\eta = 0.7$; $t_{high} = 5$, $t_{low} = 3$, and $t_{conf} = 300$ for the centerline extraction; $\rho = 0.5$, $\gamma_a = 90°$, $\gamma_r = 1.3$, $\gamma_d = 3.0$, and $c_{min} = 0.1$ for the tree reconstruction and separation; and $\sigma = 2.0$ mm, $\alpha = 0.5$, $d_m = 3.0$ mm, and $d_{min} = 0.5$ mm for the segmentation.

5.3 Evaluation and Results

Producing reference segmentations for evaluation of our method is practically infeasible for this task due to the reasons discussed in Section 1.0.3. To overcome this problem, our evaluation is based on two parts, each of them evaluating different aspects of our method with respect to structural correctness and surface accuracy. The first part is based on CT scans of a plastic phantom. Using a digital model of the plastic phantom as ground truth, we quantify the methods tube detection performance and segmentation accuracy under varying imaging conditions. The second part of our evaluation is based on clinical contrast liver CT datasets containing multiple interwoven vessel trees. Based on an assessment by a radiologist, we quantify the ability of our method to correctly obtain the structure of the different trees. In addition, the segmentation accuracy is evaluated based on a qualitative scoring scheme. Finally, a qualitative comparison to results achieved with other methods is presented.

5.3.1 Phantom Vessel Tree

To evaluate the performance of our approach under the influence of varying noise levels, scan resolutions, contrast situations, and tube diameters, we produced a plastic phantom “vessel tree” with known digital ground truth. The design of the “vessel tree” (Fig. 5.2(a)), that was manufactured with a rapid prototyping machine, is inspired by the branching pattern of the human portal vein tree of the liver and consists of about 600 cylindrical branches with varying orientation and diameter (1 mm to 16 mm). The phantom was scanned with a Siemens Somatom Sensation 64 CT scanner with various resolutions to produce different noise levels, partial volume effects, and image reconstruction artifacts. To generate different contrast situations, different “backgrounds” were used: water and water enriched with contrast agent (Fig. 5.2(c) and (d)). In Table 5.1, estimates for the contrast (gray value difference between homogeneous regions inside the phantom and the background) and the noise level (standard deviation in a homogeneous background region) are summarized. With decreasing resolution, the noise level decreases due to the averaging effect of the larger volume of a single voxel. For some datasets, the noise level is almost as high as the contrast difference.

Table 5.1: Measured contrast difference between phantom and background and standard deviation of the noise for different background types and scan resolutions.

Resolution	**Background**			
	water		water & contrast agent	
	contrast [HU]	noise [HU]	contrast [HU]	noise [HU]
$0.59 \times 0.59 \times 0.5$ mm	-44.03	40.31	-55.83	39.68
$0.59 \times 0.59 \times 1.5$ mm	-43.28	17.25	-55.51	19.60
$0.59 \times 0.59 \times 3.0$ mm	-42.62	13.11	-55.57	14.77

All CT scans of the phantom were segmented with the proposed method after adaption of the parameters on one single dataset (the high resolution dataset with water as background). The parameters are listed at the end of Section 5.2.

The surfaces of the resulting segmentations were registered to the ground truth (rigid transformation) before error measures were calculated. The error measures are based on the centerline descriptions of the ground truth and on the binary segmented volumes. To establish a relationship between an arbitrary point $\mathbf{x}$ of the segmentation and a centerline point $\mathbf{x}_i^j$ of the known ground truth, $\mathbf{x}$ is assigned to the point that minimizes $|\overrightarrow{\mathbf{x}\mathbf{x}_i^j}| - r_i^j$. This allows a correct assignment in proximity of branch points. For the computation of average errors, tubes with similar diameter were grouped together into discrete diameter

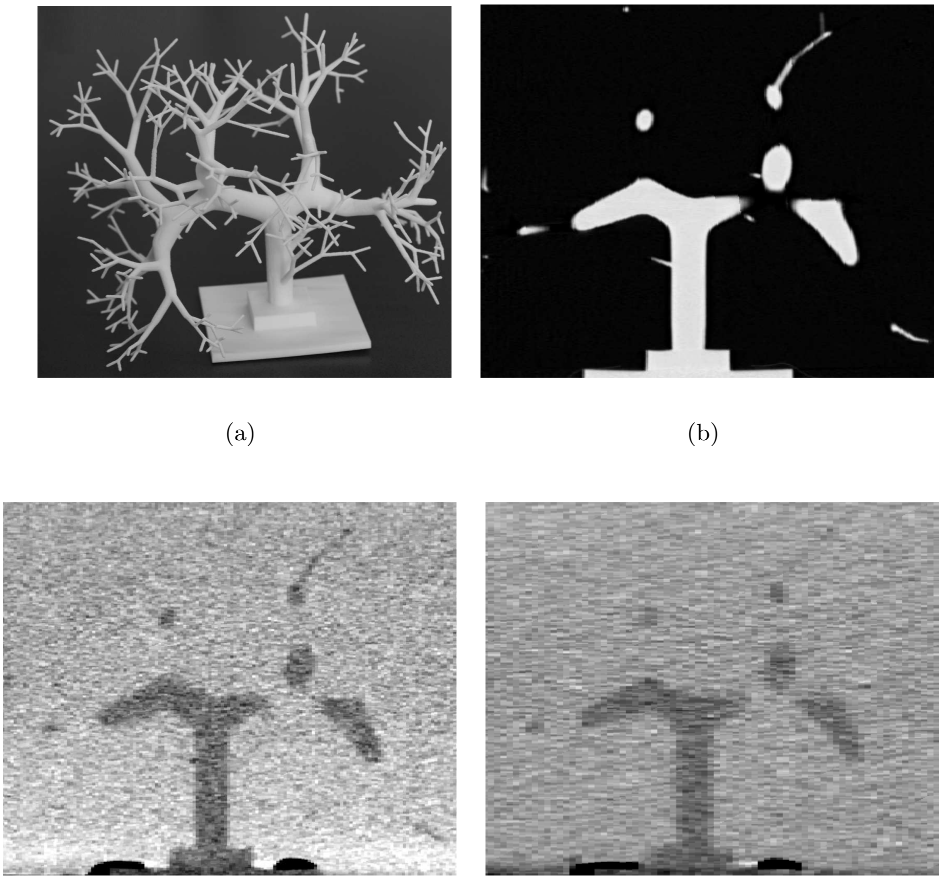

(a) (b)

(c) (d)

Figure 5.2: Rigid plastic “vessel” tree and image slices of the resulting phantom datasets for varying backgrounds and scanning resolutions. (a) The plastic “vessel” tree. (b) Ground truth of the phantom vessel tree showing thin branches that are not visible in some of the CT scans. (c) Background: water & contrast agent. Resolution: 0.59 × 0.59 × 1.5 mm. (e) Background: water. Resolution: 0.59 × 0.59 × 3.0 mm.

bins.

Tube detection: Based on the centerline description and the registered segmentations, tubes of the reference model were classified as detected or undetected, and the false negative rate and the false positive rate were calculated. We counted a ground truth tube as detected, if at least 80% of its centerline points have a corresponding centerline point in the result within a maximal distance of 2 mm. This formulation is necessary to tolerate inaccuracies of the centerline description that result from the not uniquely defined centerline descriptions in proximity of furcations. Fig. 5.3 summarizes the percentages of undetected tubes for the varying contrast situations, scan resolutions, and tube diameters. In all datasets, all tubes with a diameter above or equal to 3 mm were detected. As expected, the detection rate decreases with decreasing contrast and scan resolution, but even some of the very thin tubes can be detected in cases of low contrast and low inter-slice resolution. We also tested for false positive responses of the tubular structure extraction, but none were found.

Segmentation accuracy For quantification of the segmentation accuracy, the relative tube diameter error is used, because typical volume- or distance-based segmentation accuracy measures would be influenced by the remaining registration error. For computation of the tube diameter, every voxel of the final segmentation was assigned to its corresponding centerline point in the ground truth. Based on the volume of the tube elements and the lengths of the centerlines, the diameter d_m was calculated for every detected tube under the assumption of a perfect cylindrical shape. Based on d_m, the relative diameter error $|d_m - d_k|/d_k$ was calculated, where d_k denotes the known (true) tube diameter. Fig. 5.4 summarizes the results for varying contrast, tube diameter, and scan resolution, averaged over all tubes with a similar diameter. As can be seen, the segmentation error decreases with increasing scan resolution. For very thin tubular objects, performance seems to be slightly better for the datasets with water as background (Fig. 5.4(a)). However, only very few tubes were detected (Fig. 5.3(a)) and consequently the resulting statistic is not very meaningful. In absolute numbers, the largest diameter error found over all datasets was 1.24 mm for a tube with a diameter of 3 mm scanned at a voxel resolution of $0.59 \times 0.59 \times 3.0$ mm with water as background.

5.3.2 Clinical Datasets

In this section, an evaluation of our approach on clinically acquired contrast enhanced liver CT datasets is presented. The main focus of this evaluation was to assess, if all liver vessels are detected and if the structures of the different vascular trees is correct. In addition, the vessel segmentation quality was also assessed in terms of suitability for clinical application (e.g., planning of surgery) by using a scoring scheme.

For evaluation of our methods ability to separate multiple interwoven vessel trees, 15 clinical contrast CT datasets that show at least portal and hepatic veins were used. In 10 out of the 15 cases, livers included tumors or metastases. In one case, the right liver

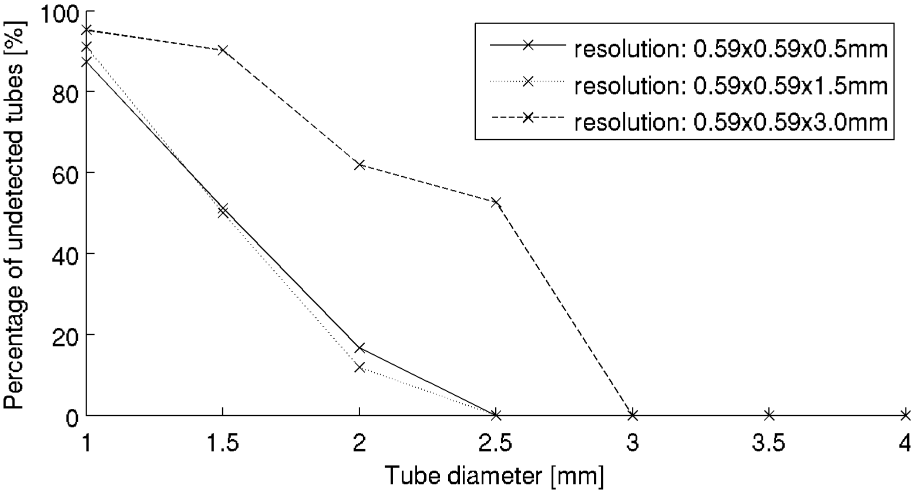

(a) Background: water.

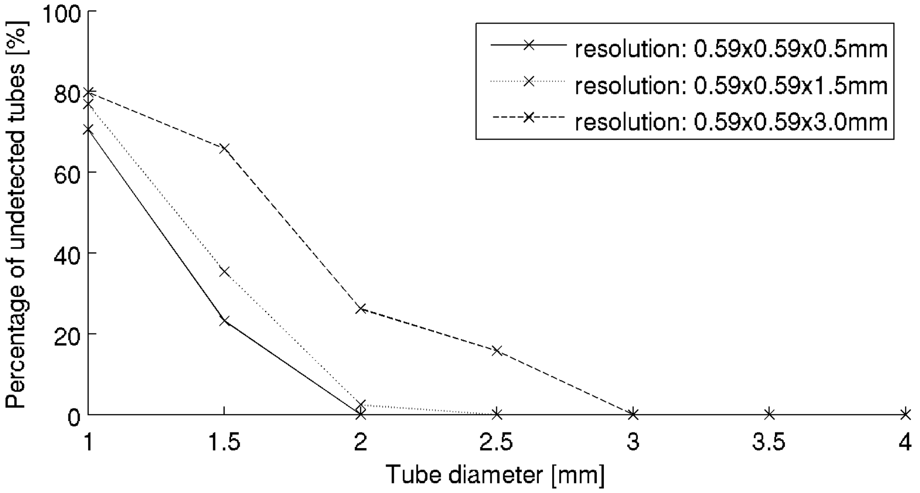

(b) Background: water & contrast agent.

Figure 5.3: Percentage of undetected tubes (false negatives) for varying contrast situations, scan resolutions, and tube diameters.

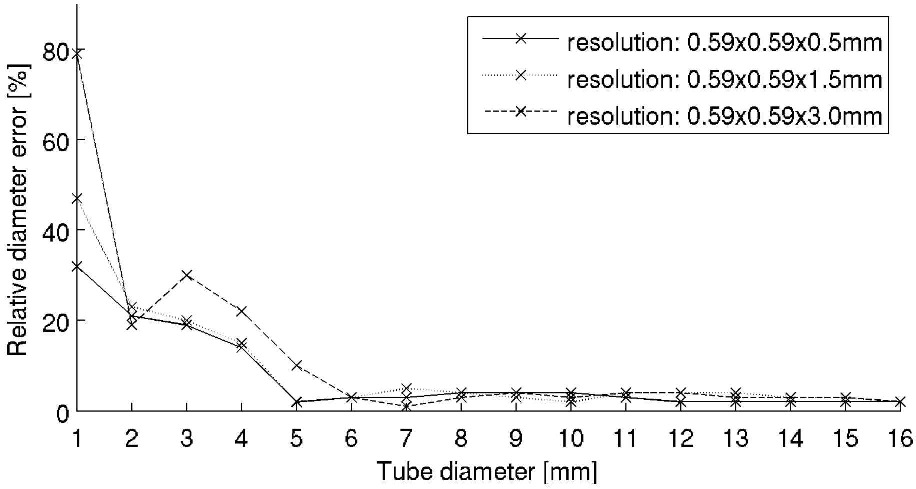

(a) Background: water.

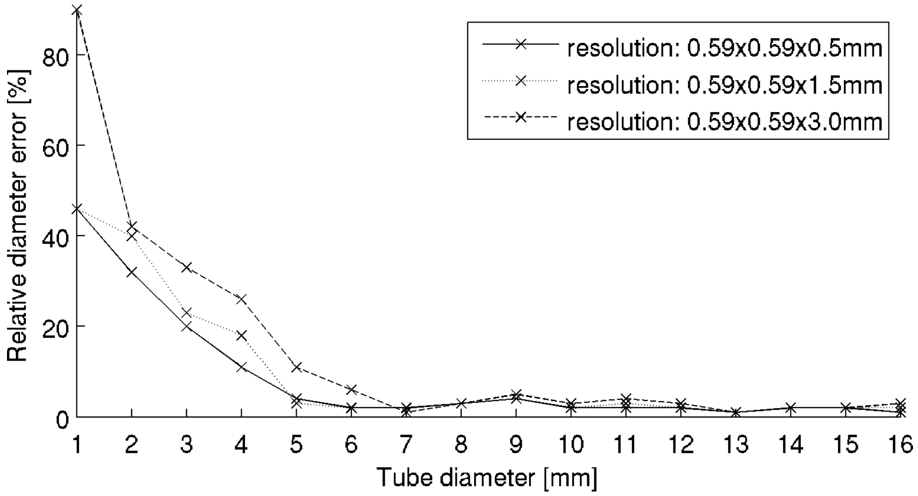

(b) Background: water & contrast agent.

Figure 5.4: Segmentation error (relative tube diameter error) for varying contrast situations, scan resolutions, and tube diameters.

lobe was resected. For segmentation, the same set of parameters as on the phantom data (Section 5.3.1) was used on all datasets. The root elements of the different vascular trees were selected manually.

For evaluation, an expert radiologist was asked to assess the above outlined evaluation criteria. To facilitate this process, we provided the radiologist an interactive visualization system. The user interface allows visualizing the CT datasets as MIPs (Fig. 5.5(a)) or cutting planes (Fig. 5.5(b)). In addition, the segmentation results of the different trees can be visualized as colorized skeletons (Fig. 5.5(c)), meshes (Fig. 5.5(e)), or as overlays on the cutting plane (Fig. 5.5(e)). The user interface also allows to: interactively change the visualization by moving the cutting plane, manipulate the display gray-value range as well as transparency, display the different vessel trees individually or together, and overlay different visualizations among each other. Such overlays provide an effective way to judge the correctness and quality of vessel segmentations. In the following paragraphs, we present the results of this assessment (Table 5.2).

Completeness/correctness of vessel branches: The radiologist was asked to identify false positive (non-existing vessel branches) or false negative (missing vessel branches) branches in the 15 segmented datasets. Note that we denote the vessel parts between bifurcations or the vessel parts at the end of the tree structures as branches. While no false positives were generated by our method, 11 (0.26%) vessel branches were identified as missing in the segmentation results (Table 5.2). Overall, 4159 vessel branches out of the 4170 true vessel branches were correctly identified. The majority of the missing vessel branches have a small diameter and low contrast. The largest missing vessel is shown in Fig. 5.6, and an example concerning the portal artery is shown in Fig. 5.7. Examples for the successful segmentation of poorly contrasted vessels and vessels in close proximity to a tumor are shown in Figs. 5.8 and 5.9, respectively.

Correctness of connections/tree separation: The ability to reconstruct and simultaneously separate different interwoven vessel systems is one of the key features of our method. For evaluation, all branch connections were assessed and judged as "correct" or "incorrect", similar to the work of Bullitt et al. [18]. In addition, we quantified the effect of each single misconnection by counting the number of affected branches as measure for the size of the affected subtree. Out of the 4159 branches that were assessed during the evaluation, only 3 (0.072%) connections were classified as incorrect, with a total number of 8 (0.19%) affected branches. An example is shown in Fig. 5.10. All errors affected distal

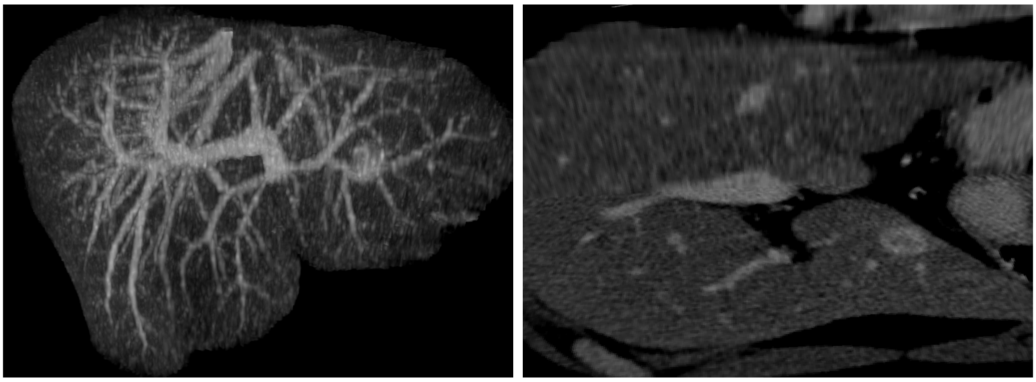

(a) 3D MIP.

(b) 2D cutting planes.

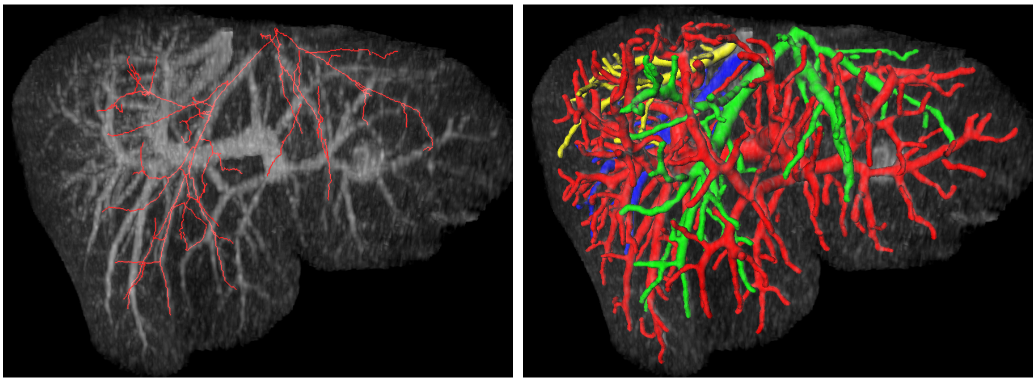

(c) Skeleton of a signle tree.

(d) All segmented trees as meshes.

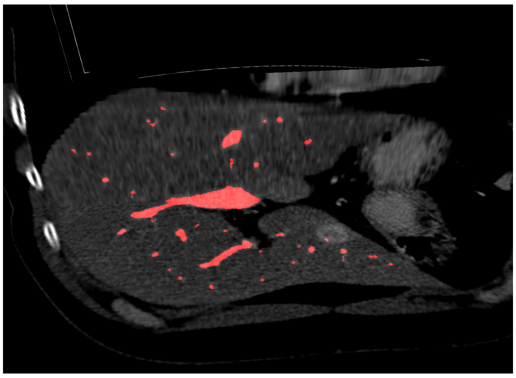

(e) Segmentation in 2D.

Figure 5.5: Interactive visualization system for evaluation of liver vasculature tree segmentation and separation with different visualization types.

Table 5.2: Summary of evaluation results on clinical liver CT datasets. The qualitative scores are on a scale of 1 to 3 with 1="poor", 2="ok", and 3="good". The "-" sign indicates that no vessels in these generations were visible.

dataset					**portal vein tree**					**hepatic vein tree**				
	# detected branches	# missing branches	# mis-connections	# affected branches	data quality	# visible generations	segmentation quality in generation			data quality	# visible generations	segmentation quality		
							0/1	2/3	4/5			proximal	medial	distal
d1	524	2(0.38%)	0	0	3	4	3	3	3	3	3	3	3	3
d2	210	0	0	0	2	2	3	2	-	3	3	3	3	3
d3	162	0	0	0	3	3	3	3	-	3	3	3	3	3
d4	625	0	0	0	3	5	3	3	3	3	3	3	3	3
d5	566	0	0	0	2	5	3	3	3	1	3	2	2	2
d6	224	0	1(0.45%)	3(1.34%)	3	4	3	3	3	3	3	3	3	3
d7	304	0	0	0	2	3	3	2	-	1	3	3	3	3
d8	212	3(1.40%)	0	0	2	3	3	2	-	1	3	3	3	3
d9	453	0	0	0	3	5	3	3	3	3	3	3	3	3
d10	138	0	0	0	2	4	3	3	2	1	2	3	3	-
d11	117	0	0	0	3	3	3	3	-	3	3	3	3	3
d12	102	0	2(1.96%)	5(4.90%)	3	3	3	3	3	3	3	3	3	3
d13	70	0	0	0	2	2	2	2	-	1	2	3	3	-
d14	380	3(0.78%)	0	0	2	4	3	3	3	2	3	3	3	3
d15	72	3(4.00%)	0	0	2	3	3	3	-	1	2	2	2	-
average	277.27	0.73 (0.26%)	0.2 (0.07%)	0.53 (0.19%)										

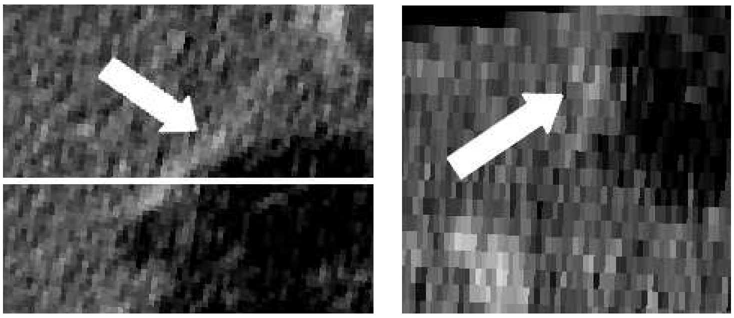

(a) Axial cutting plane through the dataset.

(b) Coronal cutting plane indicated by the white line in (a) showing anisotropy.

Figure 5.6: Unsegmented vessel (arrow) found by the radiologist.

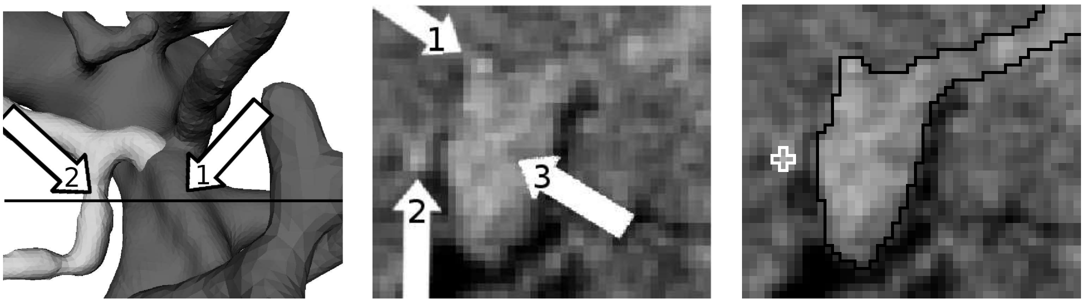

(a) Segmentation result showing the hepatic artery (bright) in proximity of the portal vein (dark).

(b) Cutting plane through the dataset indicated by the black line in (a), showing two hepatic arteries (1 & 2) close to the portal vein (3).

(c) While artery (2) was successfully detected, artery (1) was too close to the portal vein such that no tubular structure was detected/extracted. Instead, this part of the artery was segmented as part of the portal vein.

Figure 5.7: Unsuccessfully detected portal artery.

parts of the vessel trees and consisted of up to 3 branches. No misconnection of larger vessels was observed.

Data and segmentation quality: CT *data quality* and *segmentation quality* were assessed qualitatively by the radiologist, ranking them as “poor”, “ok”, or “good”. A summary of all scores is given in Table 5.2. For evaluation, results of several individual

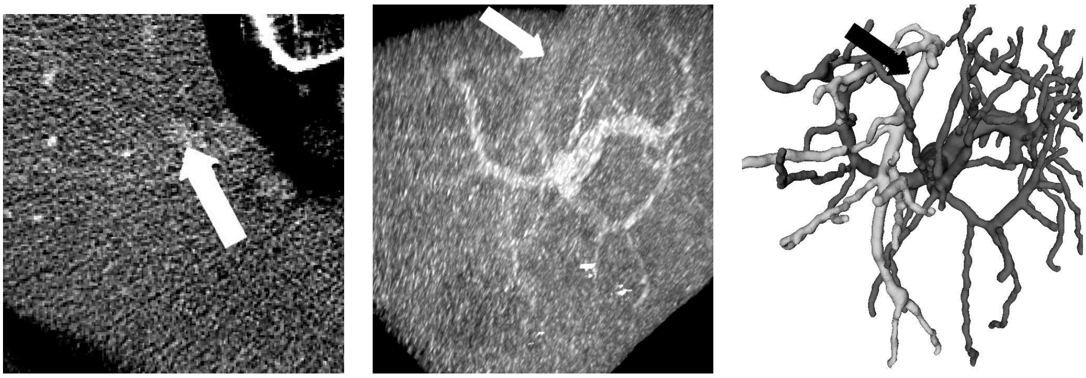

(a) Cutting plane through the dataset showing the trunk of the hepatic veins.

(b) MIP of the dataset.

(c) Segmentation result.

Figure 5.8: Successful segmentation of poorly contrasted hepatic vessels (arrow).

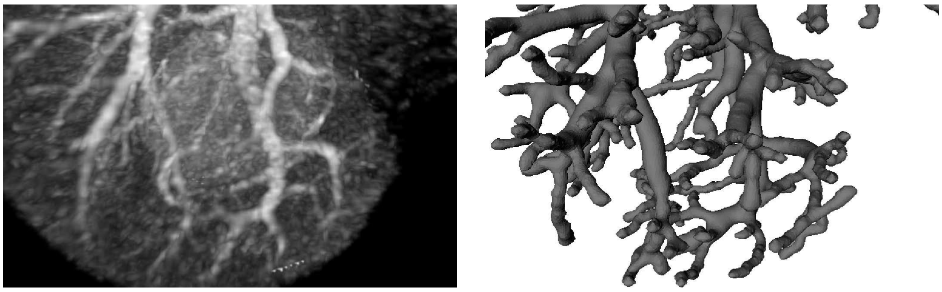

(a) MIP of dataset.

(b) Segmentation result.

Figure 5.9: Successful segmentation of vessels in close proximity of a bright tumor.

hepatic vessel trees of a liver were combined. Note that we excluded results for portal arteries, because they were only visible in 3 of the 15 utilized datasets (imaging protocol). *Data quality* is primarily related to the noise level, scan-resolution, and contrast between vessels and liver parenchyma. Note that different vascular systems can have a different score for the same dataset. The *segmentation quality* measure is utilized to evaluate the quality/accuracy of the identified vessel boundaries. As part of this evaluation, we took the non-uniform contrast agent distribution in different generations of the vessel systems into account. Consequently, we assessed the number of visible generations and the segmentation quality related to different vessel generations. In case of "good" *data quality* the segmentations were always scored as "good" in all generations, while in cases with

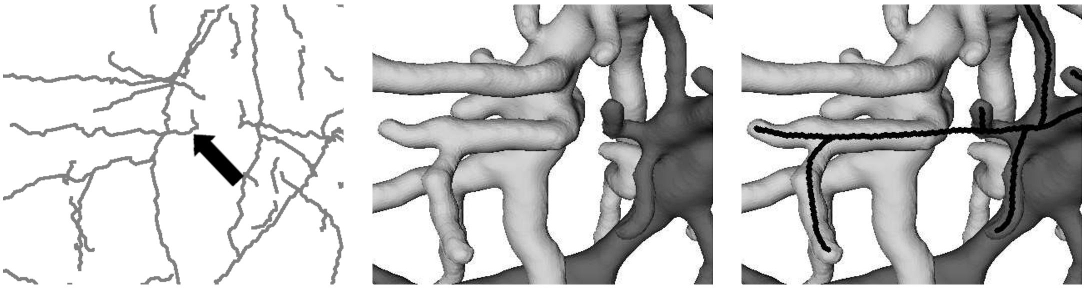

(a) Identified vessels; black arrow indicating vessel that was falsely connected to the wrong parent vessel.

(b) Segmentation result showing falsely reconstructed vessel trees.

(c) The black line indicates the correct vessel structure.

Figure 5.10: Wrong vessel connection identified by radiologist.

“poor” *data quality* and only a few visible generations, the segmentation quality tended to be scored as “ok”. This is in particular the case towards the distal parts of the portal vein tree where the contrast vanishes completely. None of the segmentations was scored as “poor”. A plot of the contrast of the main vessel trunk versus the combined centerline length for each dataset is shown in Fig. 5.11. As can be seen, the contrast varies considerably and has a strong influence (correlation) on the resulting centerline length.

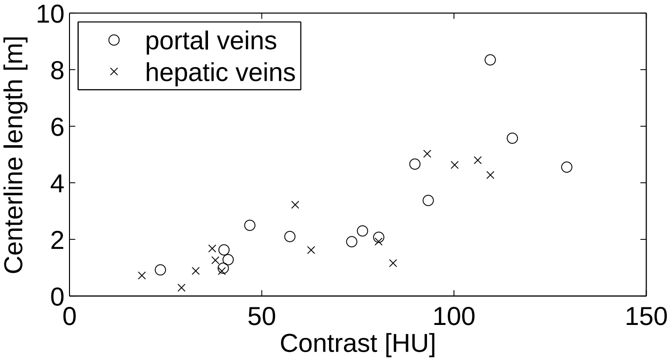

Figure 5.11: Relation between image contrast and length of the extracted portal veins and hepatic veins of the liver.

5.3.3 Comparison to Other Methods

We compare our method with two different vessel segmentation approaches proposed by Selle et al. [130] and Manniesing et al. [94]. The first method [130] was specifically designed for liver vessel separation and segmentation. The second method is a standard approach based on level sets ([94]). Both methods require a liver mask for preprocessing and the segmentation.

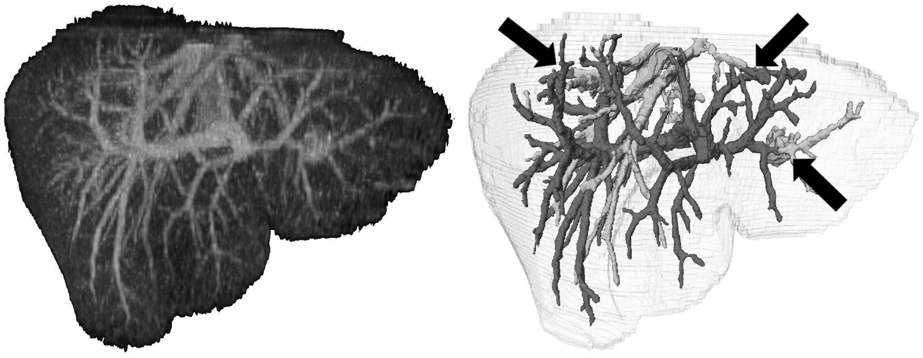

(a) MIP of the dataset using a liver mask.

(b) Segmentation results generated with Selle's approach [130] showing erroneous portal vein and hepatic vein separation.

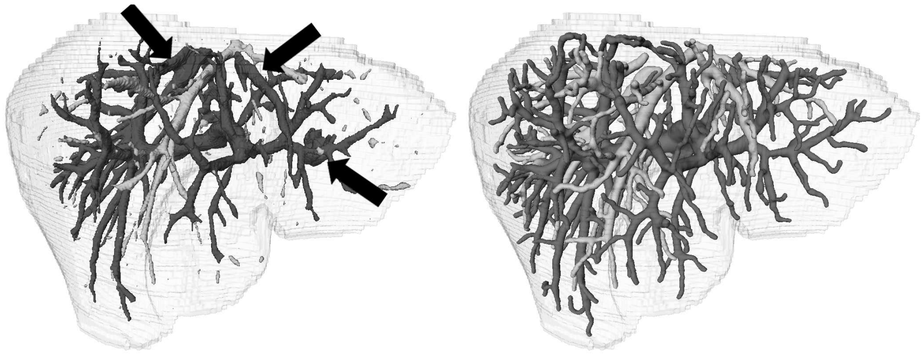

(c) Segmentation result of the level set based method [94] showing isolated vessel segments and leakage of the portal vein tree into hepatic veins and the tumor.

(d) Segmentation result of the proposed method.

Figure 5.12: Separation and segmentation of liver vessel trees in a contrast enhanced CT dataset with different methods (dark: portal veins, bright: remaining vessels). The dataset contains a tumor in close proximity to the portal vein tree and hepatic veins that overlap in the image with the portal vein tree due to partial volume effects.

Figs. 5.12(b) and (c) show segmentation results of these methods on a typical contrast enhanced liver CT dataset. Both methods utilize primarily gray-value information for segmentation. Consequently, the tumor shown in Fig. 5.12(a) is included in the segmentation results. Selle's approach to tree separation was able to remove major parts of the hepatic veins from the initial portal vein tree segmentation result. However, some errors still remain in the segmentation result (Fig. 5.12(b)). The result achieved with the algorithm of [94] contains some parts of the hepatic vein and the tumor is connected to the portal vein tree (Fig. 5.12(c)). In comparison, our approach resulted in a correct segmentation shown in Fig. 5.12(d). Our structural analysis step during the grouping an linkage of the tubular structures allows to resolve problems and a valid shape prior is generated such that leakage or undersegmentation is avoided. The ability to consider local disturbances in a more global context contributes to the robustness of our approach and is one of its major advantages.

5.4 Discussion

We have evaluated our method in Section 5.3 on several different datasets to assess the ability to: a) correctly obtain/separate different tree structures (e.g., vessel systems), b) accurately determine the surface of tubular tree structures (segmentation accuracy), and c) robustly handle noise and disturbances (e.g., tumors). In this section, we discuss different aspects of the evaluation.

Structural correctness: On experiments with phantom and clinical data, we demonstrated our method's ability to identify tubular objects (Section 5.3.1 and 5.3.2). In all experiments, no false positives were detected, demonstrating the robustness of our method to imaging artifacts and noise. With decreasing contrast and scan resolution, the detection of thin tubular objects becomes increasingly difficult, and at some point, tubes become indistinguishable from the image background. Using phantom datasets, we quantified the effect of contrast and resolution on the detectability of tubular objects. On clinical liver CT datasets, we showed the correlation between contrast and the centerline lengths of the extracted vessel trees (Fig. 5.11). For clinical liver datasets, the radiologist identified only a few missing vessel branches (11 (0.26%) out of 4170). On phantom data, far more missing tubes were identified (Fig. 5.3). In case of the phantom datasets, the location and number of tubular branches was known a priori, because of the available ground truth. Note that most of the unidentified tubes in the phantom datasets can not be visually detected in the image data by humans (Fig. 5.2). Clearly, for clinical data, no such ground truth was available. Overall, our method performed well even in case of poor data quality.

We demonstrated the ability of our method to separate and segment multiple interwoven vessel trees on clinical CT datasets (Section 5.3.2) and compared it to other methods with similar objectives (Section 5.3.3). The method performs well and produced only a few minor errors without clinical significance, contrary to the other methods. In particular, the structural grouping and linkage with the incorporated flow direction information was an important factor in obtaining the correct structure of multiple overlapping (vessel) trees (Sections 5.3.2, 5.3.3, and 3.4.1)

Segmentation accuracy: On phantom datasets we quantified the segmentation accuracy for tubular objects with different radius under varying imaging conditions (Section 5.3.1). Investigated contrasts and scan resolutions showed almost no effect on the accuracy in case of vessels with larger diameter. For thin tubular objects the statistics was not very meaningful, because only a few tube elements were detectable (about 90% undetected) due to low contrast, noise, and low resolution. For all successfully identified vessels, the absolute radius error stayed within an one voxel range (inter-slice resolution). Note that the used graph cut segmentation is only able to produce voxel accurate segmentations. We also scored the segmentation accuracy on liver CT datasets in terms of clinical usability for surgical planning (Section 5.3.2). The majority of segmented branches were scored as "good" and no branch was scored as "poor", even for datasets with "poor" *data quality.* For low quality datasets with only few visible generations, the segmentation tended to be scored as "ok" toward the distal parts of the vessel trees where the contrast almost vanishes.

Robustness: Our method performed robustly on the clinical datasets of the liver CT data as shown in our evaluation. For example, it produced correct results in disturbed regions caused by adjacent tumors (Figs. 5.9 and 5.12). All liver datasets utilized in our evaluation contained multiple overlapping vessel trees that had to be separated, and 11 out of the 15 datasets had pathological variations where other methods are likely to fail, as discussed in Section 5.3.3.

5.5 Conclusion

In this chapter, we presented and validated an approach for the segmentation and separation of the livers blood vessel trees. In contrast to other approaches, our method performs an identification of tubular objects followed by a a structural analysis to obtain the structure of the different vessel trees. This structure information is then utilized as a prior to constrain the intrinsic segmentation process. By using this strategy, problems like separation of different tubular trees/systems or handling of local disturbances are addressed on a global level by utilizing information about all identified tubular objects and the flow direction in the biological tree structures. Consequently, our approach outperforms other methods developed for this task. We evaluated our approach on phantom and clinical datasets. Results show a high robustness of our approach against disturbances, the methods ability to successfully reconstruct, separate, and accurately segment multiple interwoven tubular tree structures.

Chapter 6

Coronary Artery Tree Extraction

Contents

6.1 Introduction

Coronary artery disease is the first leading cause of death in the USA. For the assessment of coronary artery disease like plaques, aneurysms, or stenosis computer tomography angiography (CTA) has become an established method as with current multi-slice CT scanners the coronary arteries can be imaged with sufficient detail. For diagnosis, visual inspection of 2D slices of coronary CTA data is still common. However, to facilitate radiologists in this process and to raise the quality of the assessment from a pure qualitative level to a quantitative level, computer aided tools for this task are desired. An integral part for these tools is the identification of the coronary arteries and an extraction of their centerlines.

For coronary artery centerline extraction methods, the main difficulties are closely adjacent vessels or calcifications, the proximate heart chambers, changing gray value along the vessels, and regions where locally the vessels are partly indistinguishable from the background; due to occlusions or imaging artifacts for example. In the literature several techniques for the segmentation/centerline extraction of coronary arteries have been presented. For an overview, we refer to the work of Shaap et al. [124]. The methods typically follow a tracking paradigm, iteratively expanding already known coronary artery parts starting from a single seed. To the best of our knowledge, the only two exceptions are the work of Szymszack et al. [138] and Florin et al. [39]. Both identify candidate vessel locations using persistent maxima in single image slices and a normal MIP-raycasting technique, respectively. These candidate vessel locations are merged bottom-up into complete tree structures using a minimum spanning tree approach. The method of Florin et al. [39] requires a heart segmentation to limit the vessel candidate detection to a small region at the hearts surface and to avoid false candidates. The candidate selection approach of Szymszack et al. [138] is not very discriminative such that the method requires additional pruning steps and a selection of the coronary artery tree to remove false positives.

In this chapter, we present an automated approach for the extraction of coronary artery trees from cardiac CTA datasets obtaining curve skeletons for the two largest coronary trees. The approach has been evaluated on a publicly available database. Results as well as a comparison to the results achieved with other methods are presented and discussed.

6.2 Method

The method follows our general approach for segmentation of branched tubular networks as outlined in Section 1.2 to achieve a high robustness against disturbances. It combines tree main processing steps for extraction of the coronary artery trees centerlines: an extraction of all tubular structures, a grouping and linkage of the tubular structures, and discarding centerlines not belonging to the coronary arteries based on prior knowledge. The segmentation step of our general approach is skipped as accurate segmentations are not required. An exemplary dataset with intermediate processing results is shown in Fig. 6.1.

Extraction of tubular structures: For identification of tubular structures the GVF based TDF with the central medialness function as presented in Section 2.3.1 is utilized. The required initial vector field F^n is obtained from an edge potential image to be able to handle varying background conditions (e.g. calcifications) after median filtering of the original dataset (filter size $5 \times 5 \times 5$ voxels). Applying this approach for detection of coronary arteries on heart CTA datasets results in the response shown in Fig. 6.2(c), whereas applying Frangi's vesselness measure to the original vector field F^n results in the response shown in Fig. 6.2(b). The GVF based approach performs well in identifying major parts of the coronary arteries independent of their size and produces clean responses

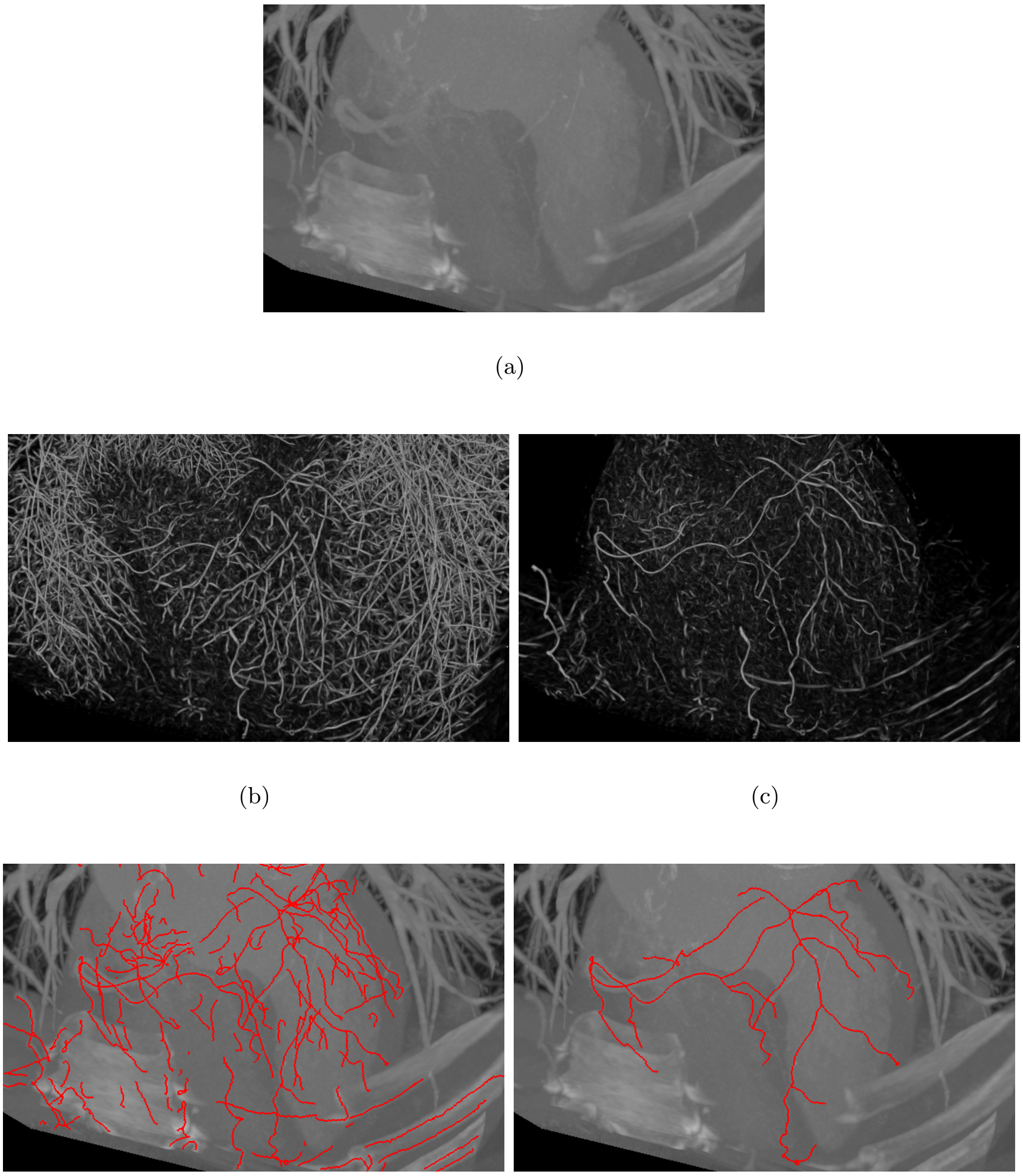

(a)

(b)

(c)

(d)

(e)

Figure 6.1: Centerline extraction and vascular tree reconstruction. (a) MIP of the original dataset (b) TDF response. (c) TDF response after suppression of responses inside the lung. (d) Extracted centerlines. (e) Identified coronary artery trees after grouping and linkage into tree structures.

at their centerlines, but for the very thin low-contrast vessels at the distal ends of the arteries the edge-information is not sufficiently strong and the response falls off completely. Compared to that, applying Frangi's vesselness measure to the original vector field F^n, the response for the thin low-contrast vessels just decreases, but it also produces responses of similar strength to some imaging artifacts/noise that locally may look similar to such thin vessels. Resolving this ambiguity in the tube detection filtering without a more sophisticated pre-processing for noise-suppression seems unrealistic. However, the usage of a hysteresis thresholding (see next paragraph) enables coping with this problem. Of course, applying Frangi's vesselness measure to F^n, does not allow detection of larger image structures. To enable an extraction of larger vessels and thin-low contrast vessels, the maximum of both filter responses – Frangi's vesselness measure applied to the initial vector field F^n and the GVF result V^n – is used which is in the remainder of this chapter considered as the TDF response T (see Figs. 6.2(d), 6.1(b) and 6.1(c)).

After the TDF step, centerlines for the individual tubular structures are extracted using the ridge traversal with hysteresis-thresholding as described in Section 2.4, and very short spurious responses are discarded by keeping only centerlines that have connected regions of a minimum length ($length > l_{min}$) above the upper threshold $T(\mathbf{x}) > t_{high}$. In Fig. 6.1(d) the extracted centerlines from the TDF response from Fig. 6.1(c) are shown. The outlined ridge traversal performs well in extracting the centerlines of the tubular objects also at the thin low-contrast ends of the vessels where the TDF response falls off considerably while still discarding short spurious responses. In this way major parts of the coronary artery centerline are already extracted, but the centerlines may break up in junction areas or regions where the vessels are partly indistinguishable from the background.

Grouping and linkage: To account for these cases and to reconstruct the complete vascular trees, the single centerlines are grouped and linked together. Therefor, possible connections (and connection costs) between the centerlines are identified based on distance, angle, and gray value difference similarly to the structure based tree reconstruction and separation method as described in Section 3.2. However, for coronary artery trees no separation of interwoven tubular tree structures is necessary and the coronary artery tree structures can be obtained by constructing a minimum spanning forest (see [25], Chapter 23). Similarly to the structure based tree reconstruction method from Section 3.2, connection costs are computed between complete centerlines and not all centerline points of all tubular structures. The endpoints of single centerlines are considered and the ap-

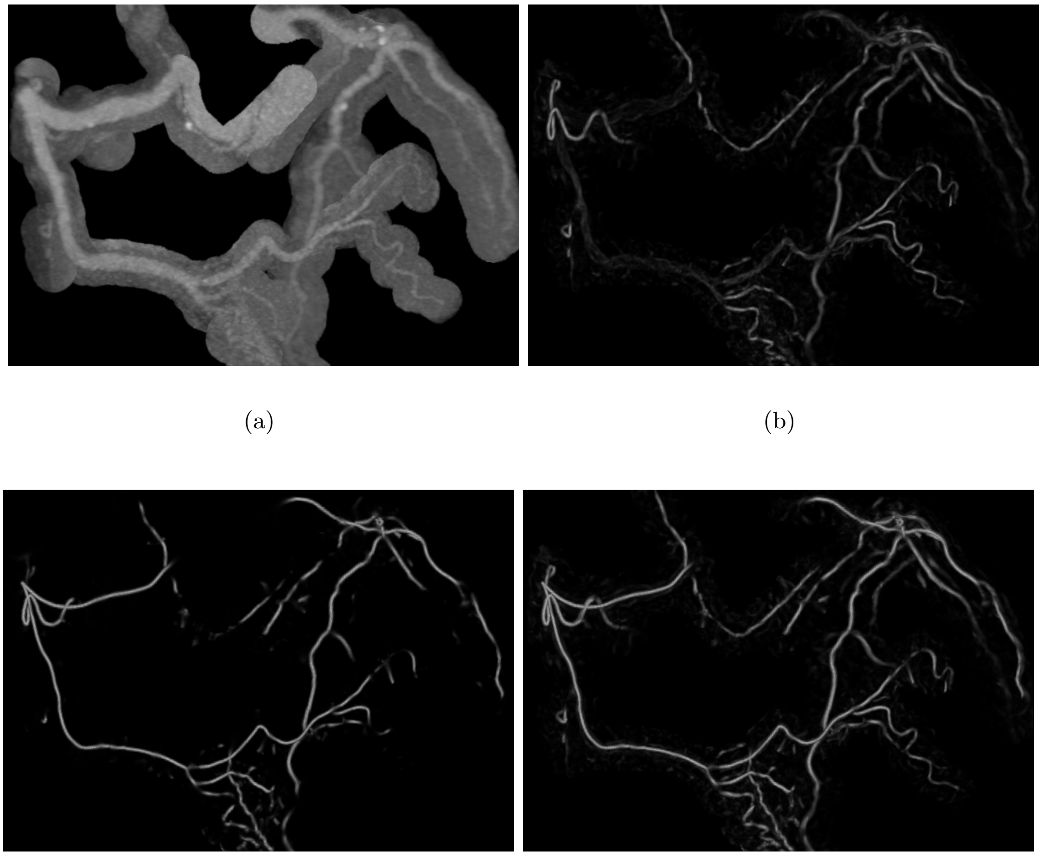
(a) (b)

(c) (d)

Figure 6.2: Tube detection step. For visualization only image regions in proximity of the coronary artery trees are shown. (a) MIP of the original dataset. (b) Tube detection result on the initial vector field F^n. (c) Tube detection result on the normalized GVF field V^n. (d) Combined tube detection result T.

proach searches in the outward pointing tangent-direction of the centerline for potential continuations. Based on the centerline points coordinate $\mathbf{x}_S$ and its tangent-direction $\mathbf{t}_S$ connection costs to other centerline points $\mathbf{x}_E$ are computed and used for the minimum spanning forest construction; possible connections with a too large gray value difference $|I(\mathbf{x}_S) - I(\mathbf{x}_E)| > d_{max}$ are immediately rejected. The connection costs $C(\mathbf{x}_S, \mathbf{t}_S, \mathbf{x}_E)$ represent a trade-off between distance and angle similarly to the formulation used in Section 3.2:

$$C(\mathbf{x}_S, \mathbf{t}_S, \mathbf{x}_E) = ||\mathbf{x}_S - \mathbf{x}_E||/exp(-\angle(\overrightarrow{\mathbf{x}_S\mathbf{x}_E}, \mathbf{t}_S)/(2\rho^2)) \tag{6.1}$$

what forms a kind of coned region (with an opening angle specified by ρ) pointing away from the centerline where the method searches for continuations; potential connections with too large costs $C > c_{max}$ are discarded. The final reconstructed trees (after removal of the non-coronary artery trees; see next paragraph) is shown in Fig. 6.1(e).

Coronary artery tree identification: The method as described above also extracts the centerlines of other tubular objects (see Fig. 6.1). Thus, not just the coronary arteries are identified, but also other structures such as blood vessels in the lung and chest area, the aorta and also some of the bones and an identification of the coronary artery trees is necessary. The lung tissue is identified and removed based on thresholding ($I(\mathbf{x}) < -700$ HU) and morphological closing using a spherical structuring element with a radius of 10 voxels; see Fig. 6.1(c) for the TDF response after removal of the lung tissue. Other tree structures not belonging to the coronary artery trees are typically isolated and relatively small. Thus, the coronary artery trees can be identified as the two largest connected components (regarding their centerline length). An example of the identified coronary artery trees is shown in Fig. 6.1(e).

Parameters: Following set of parameters is used to process the datasets. $F_{max} = 100$, $t_{high} = 0.5$, $t_{low} = 0.1$, and $l_{min} = 10$ voxels for the extraction of tubular structures with $\mu = 5$ and 500 iterations for the GVF computation [168] and $\rho = 0.7$, $d_{max} = 200$ HU, and $c_{max} = 20$ for the grouping and linkage.

6.3 Evaluation and Results

Our approach was evaluated on 32 coronary CTA datasets from the "Rotterdam Coronary Artery Algorithm Evaluation Framework" (`http://coronary.bigr.nl`), whose goal is the quantitative evaluation and comparison of methods for the coronary artery centerline extraction based on a set of well defined performance measures. The datasets are split in two groups of 8 training datasets with provided reference where the parameters have been adapted and 24 testing datasets with undisclosed reference centerlines. For each of the datasets, reference centerlines of four vessels are available that were obtained based on manual annotation and reference points that unambiguously identify the corresponding vessels. In Fig. 6.3 the coronary artery trees and provided reference centerlines are shown. Based on these provided reference points the centerlines of the associated arteries were selected from the coronary artery trees – which are extracted completely with our approach

– by following the centerline into both directions, at junctions of multiple vessels choosing the centerline with the smaller branching angle.

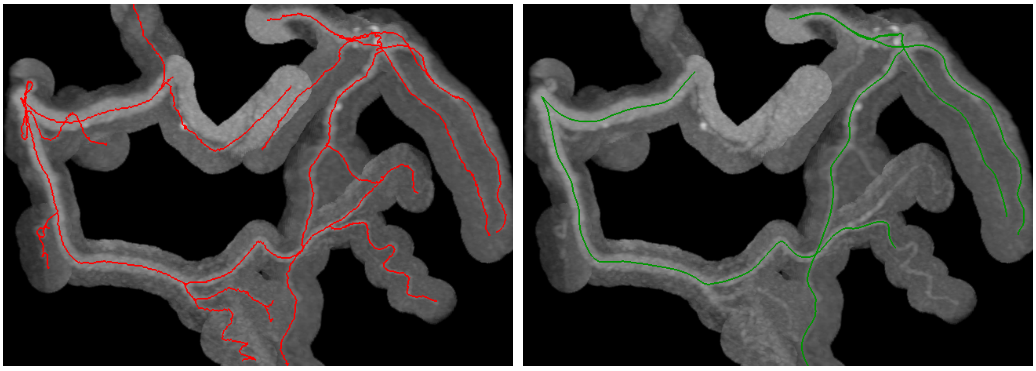

(a) Extracted coronary artery trees.

(b) Reference centerlines.

Figure 6.3: Extracted coronary artery trees and provided reference centerlines. For visualizations just the image regions in proximity to the coronary artery trees are shown.

At the proximal ends of the coronary arteries – the transition to the aorta – the centerlines extracted with our approach are sometimes slightly shorter than the reference centerlines (see Fig. 6.4). This is due to properties of the tube detection filter as these regions are not really tubular any more. To account for this issue (see the "overlap until first error" measure in Section 6.3.1), the proximal ends of the centerlines are extrapolated along a straight line, solving this issue in most datasets, but not all of them.

In the next two sections, we present quantitative results achieved with our method on the 24 testing datasets. For comparison, results achieved with other methods are summarized and discussed as well. The quantative measures were obtained by the “Rotterdam Coronary Artery Algorithm Evaluation Framework” and are available online at `http://coronary.bigr.nl`.

6.3.1 Results of Proposed Method

The performance measures are grouped into overlap measures and an accuracy measure. For the exact description of the performance evaluation and the used measures we refer to the paper of Shaap et al. [124]. The results are summarized in Table. 6.1.

Overlap: The overlap measures are used to assess the ability of the approach to identify the structures of interest. Measures are the overlap OV, the overlap until first error

Table 6.1: Summary of performance measures for proposed coronary artery centerline extraction method.

Measure	**% / mm**		
	min.	max.	avg.
OV	70.70%	100.00%	92.70%
OF	6.10%	100.00%	71.90%
OT	72.80%	100.00%	95.30%
AI	0.25 mm	0.59 mm	0.37 mm

OF, and the overlap with clinically relevant parts of the vessels OT (vessel parts with a diameter above 1.5 mm). Summarizing, our approach shows a high overlap with the provided reference centerlines: $OV = 92.70\%$, $OF = 71.90\%$, and $OT = 95.30\%$ on average; performing better than a human user on most datasets [124]. The average OF of 71.7% seems quite low. For some vessels the overlap until first error is 6.90%, while the overlap is still very high ($OV > 96.5\%$), meaning that just the first few centerline points at the proximal end are assumed to be incorrect. This behavior is related to properties of the TDF as discussed in Section 6.2. The strategy for performance evaluation just tolerates too long centerlines at the proximal end leading into the aorta (see “Clipping the proximal part” in [124]), but it does not tolerate slightly too short centerlines as delivered by our approach. However, we think that in practice this behavior of our approach is acceptable.

Accuracy: The used accuracy measure is the average distance inside the vessel AI, as the accuracy can only be evaluated when the extraction succeeded (as discussed in Section 1.0.3). On average an accuracy of $AI = 0.37mm$ is achieved, which is about the resolution of one voxel in the datasets.

6.3.2 Comparison to Other Methods

A larger set of other methods [20, 30, 49, 56, 63, 67, 102, 137, 142, 157, 176, 177] has been evaluated on the “Rotterdam Coronary Artery Algorithm Evaluation Framework”. The results achieved with these methods are summarized in Table 6.2. We refrain from a detailed discussions of all other methods and refer to the work of Shaap et al. [124]. Instead, a short comparison of our proposed method with the other methods is provided.

Degree of automation: The different methods range range from automatic extraction methods, to extraction methods with minimal user interaction, to interactive methods. Automatic extraction methods are those that do not require any user interaction, extrac-

Table 6.2: Summary of performance measures for different coronary artery centerline extraction methods.

	OV %	**OF** %	**OT** %	**AI** mm
automated methods				
Tek et al. [142]	84.7	59.5	86.2	0.34
Kitslaar et al. [63]	78.8	64.4	81.2	0.29
Zambal et al. [176]	84.7	65.3	87	0.28
proposed	**92.7**	**71.9**	**95.3**	**0.37**
VirtualContrast [157]	75.6	56.1	78.7	0.39
minimal user interaction methods				
Wang and Smedby [30]	90.8	48.9	91.7	0.46
Castro et al. [20]	67	36.3	69.1	0.59
Krissian et al.[67]	88	74.2	88.5	0.39
interactive methods				
Zhang et al. [177]	89.6	49.9	90.6	0.51
Hernandez et al. [56]	77	52.1	79	0.4
Friman et al. [49]	98.5	83.1	98.7	0.23
Szymczak [137]	95.1	63.5	95.5	0.26
Metz et al. [102]	91.9	56.4	92.5	0.46

tion methods with minimal user interaction are assumed to be those that require only one user-provided reference point per vessel, and interactive methods may use as many reference points as required. Arguably, the task at hand is easier to address with more user interaction. In particular, for the interactive methods the exact start and endpoints as well as two additional reference points along each vessel are provided by the database making it easier for the methods to achieve a high overlap.

Overlap: All other methods that have been evaluated on this database have in common is that they follow a tracking paradigm for extraction of the coronary artery centerlines. Starting from the root of the vessels the coronary arteries are tracked in an iterative fashion by consecutively expanding the already found coronary arteries. The methods of Szymszack et al. [138] and Florin et. al. [39] we mentioned in the introduction that follow a bottom-up approach have not been evaluated on this database, instead Szymszack evaluated another interactive approach [137] on this database. The results vary significantly between the different methods. Methods with more user interaction (more provided reference points) generally perform better. Compared to the other automated methods, our approach achieves a high overlap with the references, comparable to some interactive methods. However, the best performing method (Friman et al.[49]) still performs significantly better, but it utilizes information about the exact endpoint of the reference centerline.

Accuracy: Regarding centerline accuracy, our method is about average compared to the other methods. Many of the other automated methods show a higher centerline accuracy.

6.4 Discussion

In the previous section, we presented results achieved with our method on a publicly available database and presented a comparison to other approaches.

Contrary to other methods, our presented approach performed a bottom-up extraction of tubular structures with a consecutive grouping/linkage of these structures to become more robust against local disturbances. As the results show, this allows achieving a high overlap with the provided references, comparable to that achieved with interactive methods. Only methods utilizing information about the exact endpoint of the reference centerlines showed a higher overlap. However, in practice these exact endpoints of the vessels are not known and their position may vary depending on the observer when selected by a human user. This point was also shown by Schaap et al. [124] who compared the performance of different observers. Compared to the performance of different human observers, our method even performed slightly better regarding the achieved overlap with the reference centerlines.

Another issue with required reference points is, that obtaining such a set of reference points for each vessel in case the complete coronary artery trees are of relevance may be a laborious task and the result may also vary between observers. Our presented method on the other hand obtains the complete coronary artery trees without the need to specify such reference points (e.g. Fig. 6.3(a)). However, an evaluation about the completeness/correctness of the complete coronary artery tree structures has not been performed because of limitations of the database.

Compared to most other automated methods, our method shows a slightly larger average centerline distance. There are two possible reasons for this. First, the ridge traversal used for the centerline extraction as described in Section 2.4 is at most voxel-accurate. Second, the linkage strategy that is applied in regions where our TDF does not respond (e.g. at junctions) does not guarantee centered paths. However, in case a higher accuracy is required, a further refinement of the centerline point positions as a post-processing step can be applied.

The use of the used TDF allows identification of blood vessels also in proximity of calcifications or other image structures with a similar gray value (e.g. Fig. 6.4).

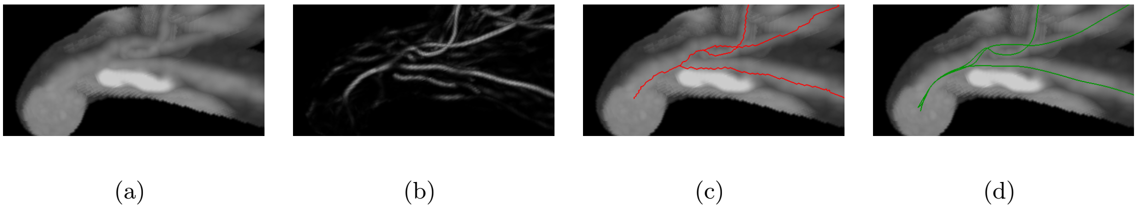
(a) (b) (c) (d)

Figure 6.4: Centerline extraction at the proximal end of the coronary artery containing a calcification. (a) Original dataset. (b) Tube detection response T. (c) Extracted centerlines. (d) Provided reference centerlines.

6.5 Conclusion

We presented an approach for the extraction of the centerlines of the coronary artery trees from CTA datasets (Fig. 6.3(a)). The approach builds on an extraction of tubular structures followed by a grouping and linkage of these structures into complete tree structures. The use of the presented TDF proofed beneficial in proximity of calcifications or nearby image structures with a similar gray value (Fig. 6.4). In combination with the presented ridge traversal that incorporates a hysteresis thresholding, centerlines of the coronary arteries can be extracted also in proximity of calcifications and in case of thin low-contrast vessels. The grouping and linkage accounts for situations where locally parts of the vessels are indistinguishable from the background; e.g. due to occlusions or imaging artifacts. Thus, our approach enables a reliable extraction of the coronary artery trees centerlines without the need for any user specified seed points. We think that the results obtained with the presented approach are a good starting point for a refinement of centerline point positions in case a higher centerline accuracy is required and for other clinically relevant measurements such as tube diameter measurement for assessment of aneurysms/stenosis or severity of adjacent calcifications.

Chapter 7

Airway Tree Segmentation

Contents

7.1 Introduction

Segmentation of airway trees in lung CT data is a prerequisite for several clinical applications including diagnosis and monitoring of lung disease or surgical planning. To facilitate such applications, it is highly desirable to have an automated and robust airway segmentation method.

In the literature, several airway tree segmentation methods have been presented. An overview is given in the survey of Sluimer et al. [132], newer approaches are discussed in [50], and a larger set of algorithms has been evaluated on the EXACT'09 database [88]. Frequently, region growing or front propagation methods [34, 128, 153] are utilized that make assumptions about the density (gray-values) of airways in CT data. More sophisticated variants of front propagation methods try to avoid segmentation errors by constantly analyzing local segmentation results and by adapting parameters accordingly. Therefor different approaches have been proposed [128, 146, 153] that utilize local information like radius or branching angle. To enhance robustness, compared to methods that solely rely on density/gray-value information for airway segmentation, some approaches focus on airway candidate detection using mathematical morphology [37], template matching techniques [136], or voxel classification based on different image descriptors [86, 122]. Many of the available approaches have problems in dealing with local disturbances (e.g., motion artifacts) or pathology (e.g., obstructed airway) which may result in incomplete airway segmentations. Graham et al. [50] addressed this problem using a different approach by building an airway tree from candidate airway branch segments by computing connection costs between branches and using graph theoretic approaches to extract the airway tree [50].

In this chapter, we present two different methods for the extraction of airways trees from CT datasets with different properties. The first method performs a segmentation of the airway tree based on the GVF, while the second method performs a reconstruction of the airway tree from detected/extracted tubular objects based on structural properties. Both approaches have been evaluated on a public database. Results as well as a comparison to the results achieved with other methods are presented and discussed.

7.2 Methods

7.2.1 Airway Tree Segmentation Based on Gradient Vector Flow

In this section, we present an automated approach for segmentation of airway trees based on the GVF. The method produces accurate segmentations of the airway lumen and the obtained GVF field may be directly utilized to obtain a high-quality skeleton. The method follows the general approach for segmentation of branched tubular networks as outlined in Section 1.2. However, the grouping step is skipped as it is not necessary for this task. The method consists of four processing steps: deriving an appropriate initial vector field and applying the GVF, extraction of tubular structures from the GVF field, segmentation of the identified tubular structures using the GVF field, and post processing for identification of the airway tree. Intermediate processing results are depicted in Figs. 7.1, 7.2, and 7.3.

Gradient Vector Flow: The extraction of the tubular objects as well as the segmentation parts utilize the GVF field $V(\mathbf{x})$ resulting from the following initial vector field that is required if one is interested in dark structures as explained in Section 2.3: $F^n(\mathbf{x}) = \frac{F(\mathbf{x})}{|F(\mathbf{x})|} \frac{min(|F(\mathbf{x})|, F_{max})}{F_{max}}$ with $F = -\nabla(G_\sigma \star I)$, where I is the original image and G_σ is a Gaussian filter kernel at scale σ. An example of applying it to a thorax CT dataset is shown in Fig. 7.1.

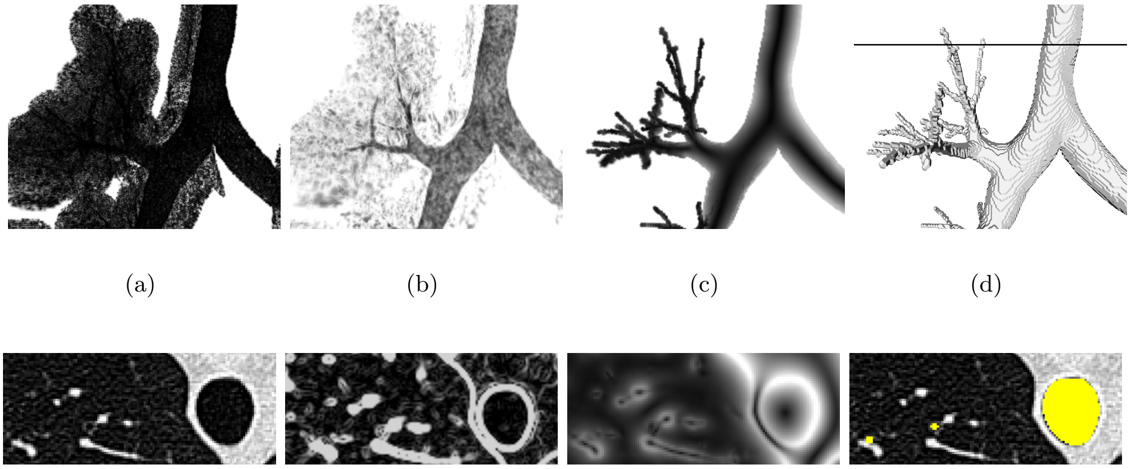

(a) (b) (c) (d)

(e) (f) (g) (h)

Figure 7.1: Example of initial vector field and GVF field on a thorax CT dataset. (a) Minimum Intensity Projection (MinIP) of the dataset. (b) MinIP showing the Gauss-smoothed dataset with $\sigma = 0.5$ that was used to calculate the initial gradient $F(\mathbf{x})$. (c) MinIP of the GVF magnitude $M(\mathbf{x})$ inside the segmentation result. (d) Segmentation result; the axial cutting plane used in (e)-(h) is indicated by a black line. (e) Axial slice of the dataset showing part of the trachea and some thin low contrast airways. (f) Magnitude of initial vector field $|F^n(\mathbf{x})|$ before applying the GVF. (g) Magnitude of the GVF field $|V(\mathbf{x})|$. (h) Segmentation result.

Extraction of tubular structures: In this GVF field, the tubular structures are identified using the offset medialness function based method as described in Section 2.3.2. This results in a tube-likeliness measure at the centerlines, as shown in Fig. 7.2(a). This information can be used for detection and centerline extraction of tubular objects. However, for thin low contrast airways, the response may fall off strongly, if their gradient-magnitude is too low so that they are not completely preserved in the GVF result (Figs. 7.1(f) and (g)). Applying the same procedure with a radius of 0.5 mm on the initial vector field $F^n(\mathbf{x})$ allows identification of these structures as shown in Fig. 7.2(b), and therefore, the maximum of both responses is utilized to produce a combined tube-likeliness volume. From this combined tube-likeliness image the centerlines of tubular structures are extracted using the hysteresis thresholding as described in Section 2.4. From these initial centerlines, short spurious centerlines with a length (below t_s) are discarded. In addition, centerlines with a mean tube-likeliness below t_m are removed. The resulting centerlines of the tubular objects are shown in Fig. 7.2(c).

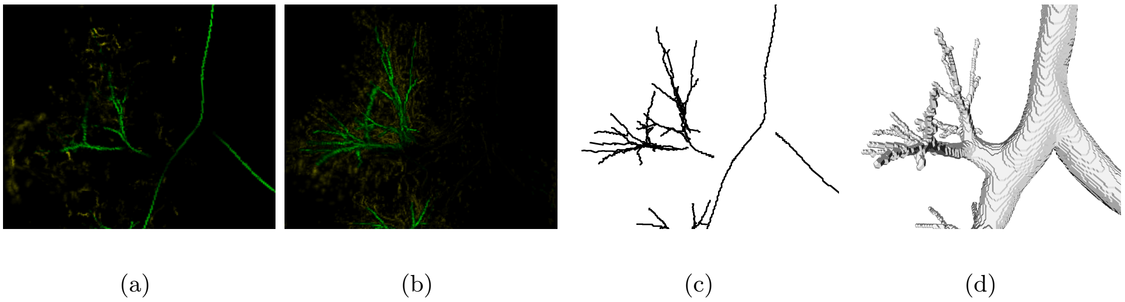
(a) (b) (c) (d)

Figure 7.2: Intermediate results of the tube centerline extraction method. The tube likeliness for the computed centerline points is shown as intensity value, and the extracted centerlines are drawn in green. (a) Tube-likeliness for larger structures. (b) Tube-likeliness for thin low contrast structures. (c) Extracted tube centerlines. (d) Segmentation result showing the size of the airways.

Tube segmentation: After identification of the tubular structures, they are segmented using the method as described in Section 4.2. The segmentation results for individual tubular structures are shown in Fig. 7.3. Note that the combination of all individually segmented airway branches provides a valid segmentation of the complete airway tree although the centerlines are not necessarily connected.

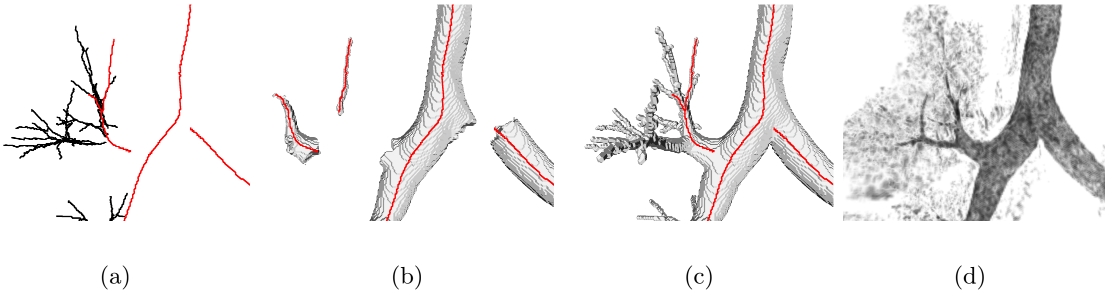
(a) (b) (c) (d)

Figure 7.3: Inverse gradient flow tracking tube segmentation applied to extracted tubular structures. (a) Extracted centerlines showing 4 selected centerlines. (b) Segmentations associated with the selected centerlines. (c) Combined results of all tubular structures. (d) MinIP of smoothed dataset for comparison.

Post processing: For the actual identification of the airway tree, the largest connected segmented component is extracted and other segmented tubular structures are discarded.

Additionally, the extracted centerlines are dilated and added to the segmentation result to assure 6-connected segmentation results.

Parameters: The following set of parameters is used for segmentation of the datasets: $\sigma = 0.5mm$, $F_{max} = 200$, $\mu = 5$ for the GVF using 500 iterations, $t_{high} = 0.5$, $t_{low} = 0.1$, $t_s = 5$, and $t_m = 0.5$.

7.2.2 Airway Tree Reconstruction Based on Multi-Scale Tube Detection

In this section, we present an automated approach for the reconstruction of airway trees. It is based no our general approach for segmentation of branched tubular networks as outlined in Section 1.2 to achieve a high robust against local disturbances which can result from disease or imaging artifacts, for example. The method consists of three main processing steps: preprocessing, extraction of tubular objects, and a grouping and linkage of the identified tubular objects to reconstruct the airway tree. Fig. 7.4 illustrates the individual processing steps by showing intermediate results.

Preprocessing: To fully automate the approach for airway detection, the input CT dataset is preprocessed to discard non lung tissue and to restrict the search area for tubular structures. Therefor, a rough lung mask is generated by using thresholding ($< -700HU$), connected component analysis, and morphological closing with a ball structuring element with a radius of 10 voxels. All voxels outside this lung mask or with a value larger than $-700HU$ in the original dataset are set to $-700HU$. The resulting dataset (Fig. 7.4(a)) was used as input for the later steps of the method.

Extraction of tubular structures: For extraction of tubular structures, the tube detection filter of Pock et al. [113] as described in Section 2.2.2 is utilized in combination with the height-ridge traversal with hysteresis-thresholding for centerline extraction as described in Section 2.4. The method of Pock et al. was slightly adapted as for thin airways the surrounding is not necessarily symmetric and the utilized symmetry criterion adversely influences the tube detection. Therefore, for these structures (radius $\leq 0.5mm$), the variance-based symmetry criterion is discarded. The tube detection filter response is shown in Fig. 7.4(b). To discard short spurious responses of the tube detection filter (noise), all centerlines with an accumulated tube detection filter response below t_{conf} are discarded. Figs. 7.4(c) and (d) depict the resulting descriptions of the identified tubular structures. Fig. 7.4(c) shows only the centerline information, while in Fig. 7.4(d) also the

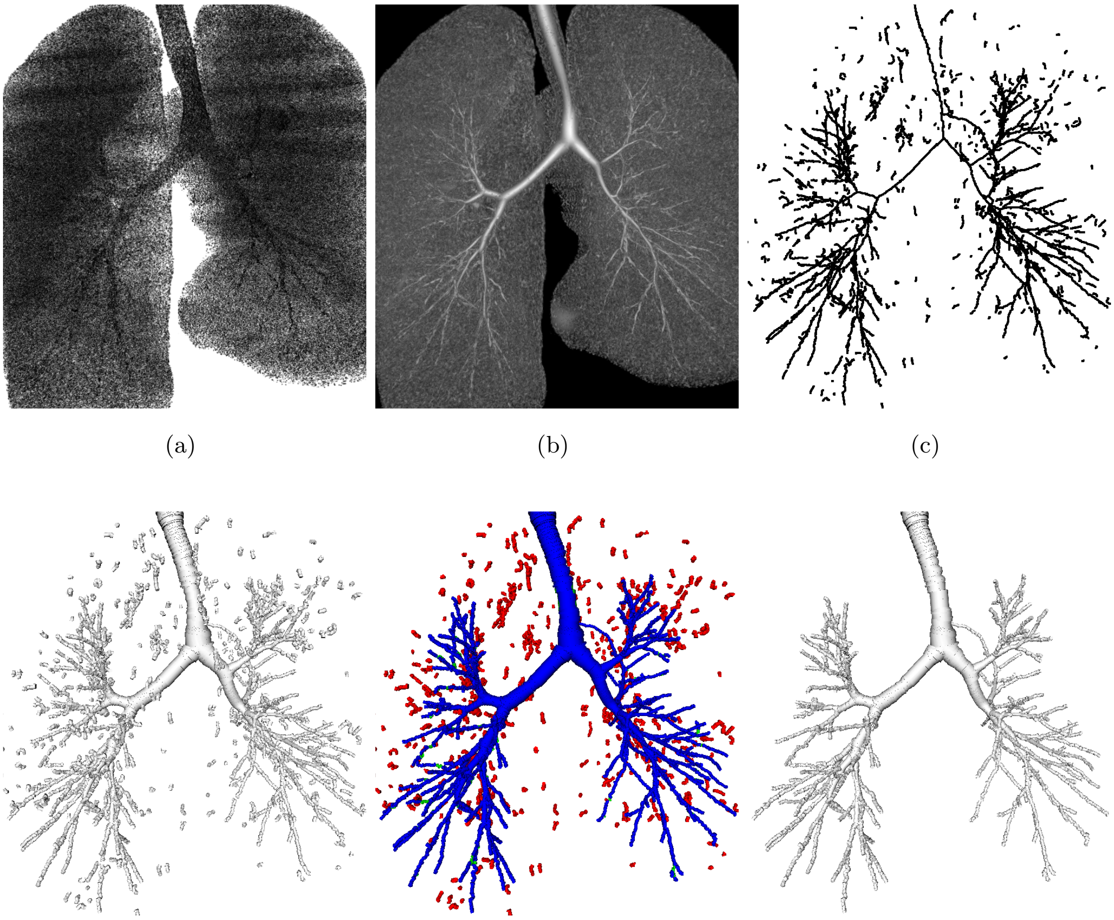

(a) (b) (c)

(d) (e) (f)

Figure 7.4: Illustration of the processing steps of the airway tree reconstruction approach. (a) Volume rendering of the utilized dataset. (b) Tube detection filter response. (c) Centerlines of initially extracted tubular structures. (d) Initially extracted tubular structures with associated radii/tangent directions. (e) Grouping and linkage step showing the identified tubular structures belonging the airway tree (blue), the discarded tubular structures (red), and the closed gaps (green). (f) Reconstructed airway tree.

associated radius and tangent direction are indicated using a cylinder with appropriate orientation and radius. As can be seen, major parts of the airway tree can be extracted with this approach. However, two problems remain that have to be addressed. First, the centerlines of the tubular structures may break up at junctions or in disturbed regions (e.g., motion artifacts). Second, some false positive responses caused by other low density (dark) tube-like structures that are not airways are also present.

Grouping and linkage: For reconstruction of the airway tree the structure base approach as presented in Section 3.2 is utilized that is used to identify the tubular structures that are part of the actual airway tree and to discard all other unrelated tubular structures. The method requires information about the root of the tree and the flow direction inside this root element. Therefore, the trachea is identified automatically by searching for the largest tubular structure, it's flow direction is determined as pointing towards the center of the volume. The result of the tree reconstruction process is shown in Figs. 7.4(e) and (f).

Parameters: Following set of parameters is used to process the datasets. The tube detection is performed on 15 radius steps on a logarithmic scale between radii 0.25 mm and 10 mm with $\eta = 0.7$ (the variance term of the boundariness samples in the offset medialness function was omitted for radii ≤ 0.5 mm); $t_{high} = 35$, $t_{low} = 25$, and $t_{conf} = 150$ for the centerline extraction; $\rho = 0.5$, $\gamma_a = 90°$, $\gamma_r = 1.3$, $\gamma_d = 40$ mm, and $\gamma_c = 0.1$ for the tree reconstruction.

7.3 Evaluation and Results

Both approaches were applied to 40 clinical datasets (with undisclosed gold standard) which were provided by the "Extraction of Airways from CT 2009 (EXACT09)" database (`http://image.diku.dk/exact`), whose objective is the quantitative evaluation and comparison of airway tree extraction methods. The focus of the database is on the methods ability to successfully extract the structure of the airway trees, while surface accuracy is not considered. The datasets are split in two groups of 20 training datasets, where the parameters are adapted and 20 testing datasets. For information about how the reference segmentations were obtained and the exact definition of the used performance measures we refer to Lo et al. [88].

For evaluation, binary volume datasets are required that contain a single 6-connected airway structure. While the GVF based method (Section 7.2.1) already provides such a segmentation, the airway tree reconstruction method (Section 7.2.2) only produces a 26-connected airway tree skeleton with corresponding radius information. Thus, to obtain a binary volume dataset for the airway tree reconstruction method, we performed an inverse distance transformation to obtain a rough segmentation and dilated the so obtained reconstruction to assure 6-connectivity.

In the next two sections, we present quantitative results achieved with our two presented methods on the 20 testing datasets and for comparison results achieved with other methods. The quantitative measures were provided by the “Extraction of Airways from CT 2009 (EXACT09)” database and are available online at `http://image.diku.dk/exact`.

7.3.1 Results of Proposed Methods

Tables 7.1 and 7.2 summarize the evaluation results for the 20 testing datasets of both methods. For the GVF based method (Table 7.1), on average 63.0% of airway branches were detected with an average detected tree length of 58.4%. The mean leakage count was 5.0, and the mean false positive rate was 1.44% (median: 0.61%). For the airway tree reconstruction method (Table 7.2), on average, 57.9% of airway branches were detected with an average detected tree length of 55.2%. The mean leakage count was 6.5, and the mean false positive rate was 2.44% (median: 1.41%).

7.3.2 Comparison to Other Methods

A larger set of other methods [13, 35, 36, 38, 57, 76, 87, 100, 112, 147, 154, 158, 160] has been evaluated on the “Extraction of Airways from CT 2009 (EXACT09)” database. The results achieved with these methods are summarized in Table 7.3 and Fig. 7.5. We refrain from detailed discussions of all other methods referring for this purpose to the work of Lo et al. [88] and only provide a short comparison of our proposed method with the other methods.

Most methods for airway tree segmentation are fully automated methods, or they are semi-automated methods that require only minimal user interaction such as selecting initial seed points inside the trachea or adaption of parameters. An exception is the method of Tschirren et al. [147] that is part of a clinical product. Their software allows for extensive editing of an initial segmentation result. What all other methods have in common, is that they use region-growing or wave propagation approaches for extraction of the airway trees. The methods evolve starting from a seed inside trachea and recursively merge potential airway regions, usually combined with a method for leakage prevention.

A large variation between the performance of the different methods can be observed as well as a general trade-off between extraction capability and leakage as shown in Fig. 7.5. Methods with higher branch count also show a higher leakage volume and vice versa. The better methods show an ability to extract about 55-60% of the airway tree with a false positive rate of below 5%. The method with the highest extraction capability also allows extraction of only about 75%. However, to the cost of a false positive rate of more than

Table 7.1: Evaluation results for the GVF based method (Section 7.2.1) on the twenty test cases.

	Branch count	Branch detected (%)	Tree length (cm)	Tree length detected (%)	Leakage count	Leakage volume (mm^3)	False positive rate (%)
CASE21	114	57.3	68.5	62.0	3	35.2	0.31
CASE22	270	69.8	218.9	66.2	9	474.6	1.60
CASE23	187	65.8	134.0	51.5	5	43.5	0.20
CASE24	139	74.7	113.9	70.0	8	176.9	0.59
CASE25	158	67.5	123.1	48.8	4	98.6	0.32
CASE26	59	73.8	51.2	78.0	2	274.3	2.70
CASE27	77	76.2	58.1	71.7	4	353.5	3.06
CASE28	86	69.9	66.9	61.0	1	49.6	0.43
CASE29	120	65.2	81.2	58.8	4	118.9	0.85
CASE30	114	58.5	87.5	57.2	5	98.9	0.64
CASE31	96	44.9	70.5	40.2	1	59.8	0.34
CASE32	101	43.3	80.3	36.8	1	175.2	0.86
CASE33	117	69.6	90.4	61.5	1	32.0	0.29
CASE34	250	54.6	184.6	51.6	11	358.1	1.05
CASE35	168	48.8	110.9	35.9	5	69.8	0.30
CASE36	294	80.8	330.6	80.2	5	78.6	0.25
CASE37	112	60.5	87.9	49.5	2	102.9	0.48
CASE38	64	65.3	51.2	77.1	4	311.0	2.64
CASE39	291	56.0	250.6	61.2	13	3577.0	9.21
CASE40	225	57.8	187.7	48.5	11	959.0	2.65
Mean	152.1	63.0	122.4	58.4	5.0	372.4	1.44
Std. dev.	75.7	10.4	75.2	13.2	3.6	785.4	2.06
Min	59	43.3	51.2	35.9	1	32.0	0.20
1st quartile	96	56.0	68.5	48.8	2	59.8	0.31
Median	119	65.3	89.2	59.9	4	110.9	0.61
3rd quartile	250	73.8	187.7	71.7	9	358.1	2.65
Max	294	80.8	330.6	80.2	13	3577.0	9.21

15%. None of the methods comes close to obtaining the whole airway tree.

The method of Graham et al. [50] who also presented an airway tree extraction approach based on a bottom-up airway detection with a consecutive grouping into a complete tree structure as described in the introduction has not been evaluated on the database.

Table 7.2: Evaluation results for the airway tree reconstruction method (Section 7.2.2) on the twenty test cases.

	Branch count	Branch detected (%)	Tree length (cm)	Tree length detected (%)	Leakage count	Leakage volume (mm^3)	False positive rate (%)
CASE21	100	50.3	54.6	49.4	1	102.5	1.09
CASE22	296	76.5	258.7	78.3	23	1311.2	3.91
CASE23	232	81.7	201.0	77.2	14	700.5	2.81
CASE24	148	79.6	121.0	74.4	5	288.7	1.18
CASE25	157	67.1	134.0	53.2	9	1693.0	6.08
CASE26	39	48.8	29.4	44.7	4	254.1	5.13
CASE27	38	37.6	27.6	34.1	1	56.8	1.08
CASE28	70	56.9	50.9	46.5	2	8.6	0.09
CASE29	118	64.1	83.6	60.5	3	222.6	1.56
CASE30	91	46.7	70.2	46.0	1	47.6	0.32
CASE31	100	46.7	73.8	42.0	1	64.7	0.38
CASE32	125	53.6	118.6	54.4	2	34.8	0.14
CASE33	117	69.6	99.1	67.4	15	931.2	7.56
CASE34	296	64.6	233.5	65.3	6	167.3	0.49
CASE35	187	54.4	133.2	43.1	2	123.3	0.57
CASE36	239	65.7	283.0	68.7	8	661.1	2.12
CASE37	96	51.9	82.8	46.6	5	360.2	2.25
CASE38	40	40.8	30.8	46.3	2	79.6	1.25
CASE39	210	40.4	198.1	48.4	8	745.7	2.61
CASE40	237	60.9	219.6	56.7	17	3678.0	8.07
Mean	146.8	57.9	125.2	55.2	6.5	576.6	2.44
Std. dev.	81.8	13.0	80.3	12.8	6.3	864.9	2.46
Min	38	37.6	27.6	34.1	1	8.6	0.09
1st quartile	91	46.7	54.6	46.0	2	64.7	0.49
Median	122	55.6	108.8	51.3	5	238.3	1.41
3rd quartile	237	69.6	219.6	68.7	14	931.2	5.13
Max	296	81.7	283.0	78.3	23	3678.0	8.07

7.4 Discussion

Discussion of the GVF based method: The evaluation results show that this method achieves a good average airway branch count (63.0%) without any major leakage. One exception is CASE39, where some leakage occurred ($3577mm^3$), a dataset with emphysema. Examples of segmentation results are shown in Fig. 7.6 and Fig. 4.5(c). As can be seen, the segmented surface shows a good correspondence with the image data. The

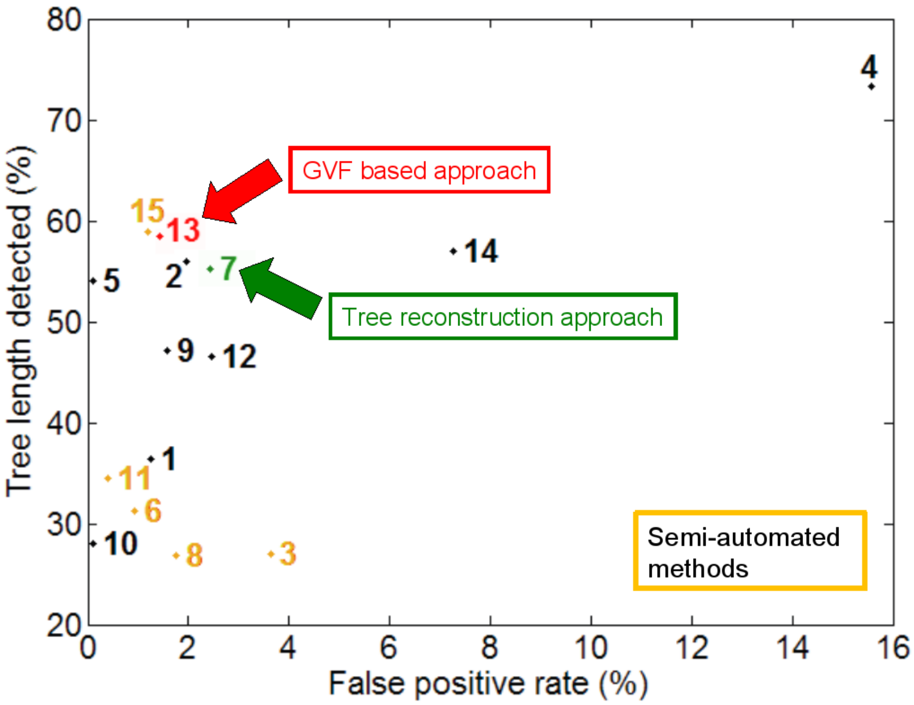

Figure 7.5: "Tree length detected" vs. "false positive rate" for different airway tree extraction methods based on [88]. To ascribe the individual methods numbers to the corresponding publication see Table 7.3.

method is also capable of handling cases where the airway shape deviates from a perfectly circular or purely convex shape (e.g., trachea of CASE18 in Figs. 7.6 and 4.5(c)). Leakage into non-tubular structures is uncommon. However, in case of emphysema some leakage was observed (e.g., CASE14 in Fig. 7.6).

Discussion of the airway tree reconstruction method: In this paragraph, we discuss properties of the tree reconstruction approach based on two examples. In Fig. 7.7, a case with emphysema is shown. Several structures that are similar to airways are present in the image data. They are hard to distinguish solely based on gray-value appearance. Without utilizing prior knowledge about the structure of airway trees, a correct segmentation is hard to achieve, and simple algorithms will likely show leakage. As shown in Fig. 7.7(b), our approach initially also identifies some of these structures as tubular structures. However, the constraints incorporated into the tree reconstruction step successfully prevent that such structures are added to the airway tree (Fig. 7.7(d)).

In the example shown in Fig. 3.4(a) and (b), a tumor infiltrates the airway wall and blocks one of the lower airway branches completely, such that the airway tree appears to be unconnected in the image data. Contrary to region growing or front propagation approaches, our approach identifies the unconnected airways and allows us to link them together (Fig. 3.4(e)). This ability enables our method to handle local disturbances robustly.

Compared to other methods, a slightly increased leakage volume can be observed; Fig. 7.8(a)-(c) depicts the three cases with the largest "leakage volume". Two points can be observed: first, the majority of the "leaks" detected by the evaluation framework are due to surface representation inaccuracies (Figs. 7.8(c) and (d)) and second, blobs are included in some airway segmentations (Figs. 7.8(a) and (b)). Our approach produces a description of the airway tree on a structural level (centerline points, radius, tangent direction), but not a voxel or sub-voxel accurate segmentation of the inner and/or outer airway wall(s). The first point can be explained as we performed a dilation of the segmentation results to assure 6-connectivity, which negatively influencs the performance evaluation. The second point was later found to be related to a bug in the software part that transforms the structural representation to a binary volume dataset.

Comparison between the two methods: We presented two approaches for airway tree extraction from CT datasets with different properties. Regarding the evaluation, both seem to perform comparably well on this database and the differences are more on the qualitative side. While with the GVF based method shows a higher "branch count", is the "tree length" larger for the airway tree reconstruction method. The "leakage volume" for the airway tree reconstruction method seems slightly larger. However, reasons for this statical conclusion were discussed.

The GVF based approach produces a voxel-accurate segmentation of the airway lumen while the airway tree reconstruction method only produces a structural representation roughly describing the airways surfaces. An additional advantage of the GVF based methods is that the presented centerline extraction method may be easily extended to extract a complete high quality curve skeleton of the airway tree. This can be achieved by obtaining connections between the individual centerlines based on the GVFs medialness property using the method presented in Section 3.3. However, the GVF based method can not cope with severe disturbances (e.g. the example with the tumor) and it does not avoid leakage in case of emphysema as no structural verification of the airway tree is performed. Contrary to that, the airway tree reconstruction method allows handling these disturbances successfully.

Comparison to other methods: Our two approaches show a good trade-off between airway extraction capability and leakage volume compared to the other methods (Fig. 7.5 and Table 7.3). Only the method of Tschirren et al. [147] that is based on extensive user interaction shows a larger amount of extracted airway branches and a lower leakage volume; the results achieved with this method also represent the performance of a human observer on this task. Tschirren et al. [147] note that with their method a human observer requires on average about one hour of work to produce results like these.

Although both proposed methods perform well compared to other presented methods, with both methods typically only less than 60% of the airway trees can be extracted, showing the need for further improvements of all methods known in the literature [88].

7.5 Conclusion

We presented and evaluated two different methods for extraction of airway trees in CT datasets. The main differences between both are in their general objectives. The GVF based method already produces accurate segmentations and allows for an additional extraction of the associated curve skeleton in a straight forward manner. On the other hand, the airway tree reconstruction methods allows handling of local disturbances and shows a higher robustness in case of disease as additional structural properties of the whole tree structure are incorporated into the approach. Thus, giving a general conclusion about the superiority of one of the methods can not be made as both approaches have different advantages. A combination of properties of both approaches would be beneficial.

Table 7.3: Summary of performance measures for different airway tree extraction methods.

Nr.	method	Branch count	Branch detected (%)	Tree length (cm)	Tree length detected (%)	Leakage count	Leakage volume (mm^3)	False positive rate (%)
	automated methods							
1	Irving et al. [57]	91.1	43.5	64.6	36.4	2.5	152.3	1.27
2	Fetita et al. [36]	157.8	62.8	122.4	55.9	12.0	563.5	1.96
4	Feuerstein et al. [38]	186.8	76.5	158.7	73.3	35.5	5138.2	15.56
5	Lo et al. [87]	150.4	59.8	118.4	54.0	1.9	18.2	0.11
7	**proposed tree reconstruction approach (Section 7.2.2)**	**146.8**	**57.9**	**125.2**	**55.2**	**6.5**	**576.6**	**2.44**
9	Wiemker et al. [160]	139.0	56.0	100.6	47.1	13.5	368.9	1.58
10	Lee et al. [76]	79.3	32.4	57.8	28.1	0.4	14.3	0.11
12	Weinheimer et al. [158]	130.1	53.8	95.8	46.6	5.6	559.0	2.47
13	**proposed GVF based approach (Section 7.2.1)**	**152.1**	**63.0**	**122.4**	**58.4**	**5.0**	**372.4**	**1.44**
14	Rikxoort et al. [154]	161.4	67.2	115.4	57.0	44.1	1873.4	7.27
	semi-automated methods							
3	Pinho et al. [112]	74.2	32.1	51.9	26.9	4.2	430.4	3.63
6	Fabijanska [35]	77.5	36.7	54.4	31.3	2.3	116.3	0.92
8	Mendoza et al. [100]	71.5	30.9	52.0	26.9	0.9	126.8	1.75
11	Born et al. [13]	93.5	41.7	65.7	34.5	1.9	39.2	0.41
15	Tschirren et al. [147]	148.7	63.1	119.2	58.9	10.4	158.8	1.19

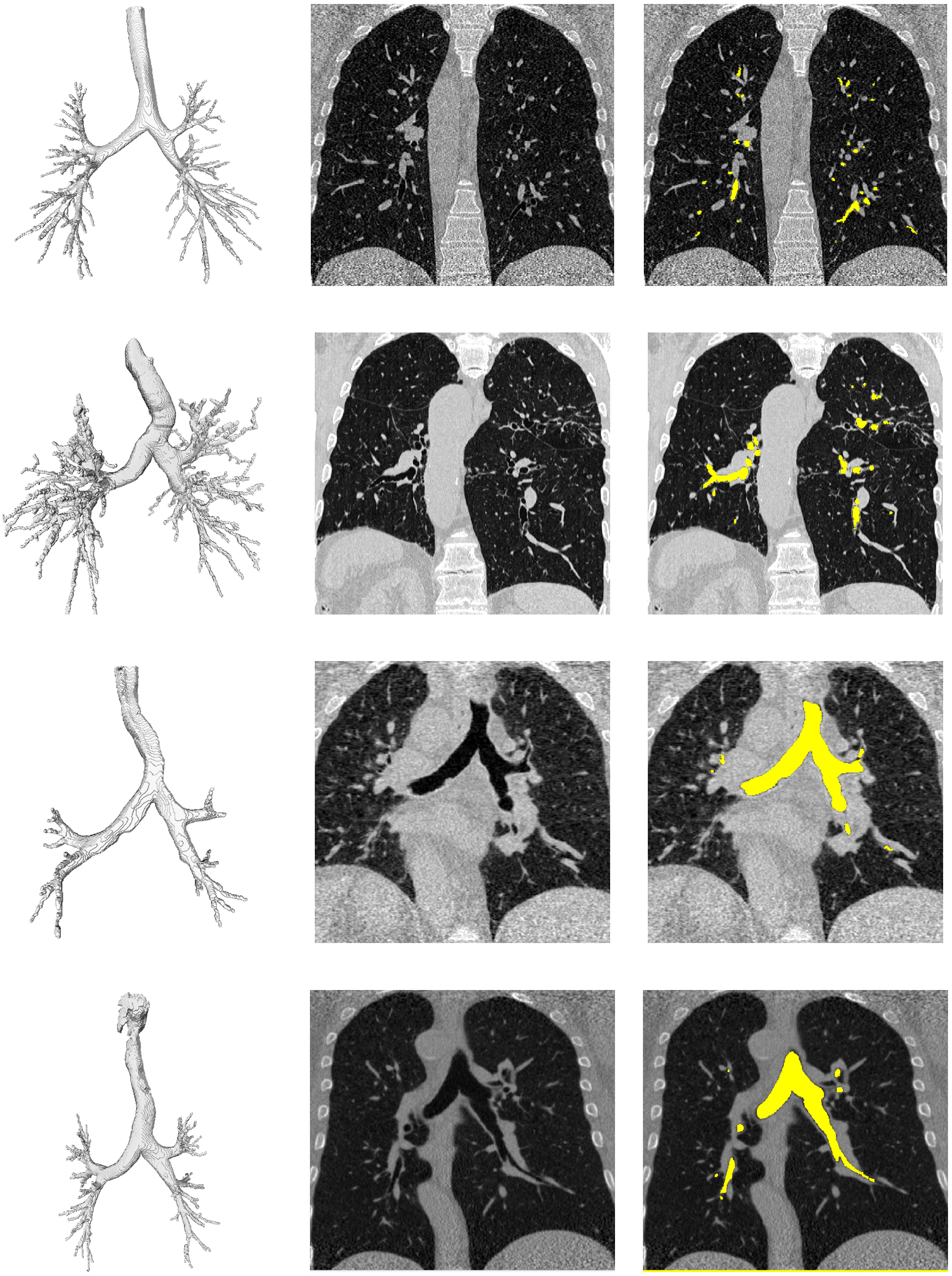

Figure 7.6: Examples of segmentation results on the EXACT09 database using the GVFG based method (Section 7.2.1). From top to bottom: CASE03, CASE14, CASE18, CASE24. From left to right: 3D visualization of result; coronal slice showing CT data; coronal slice showing the segmentation result.

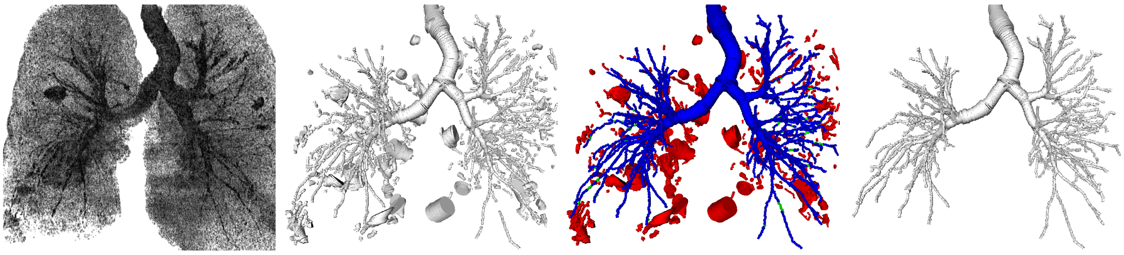

Figure 7.7: Emphysema lung CT data. (a) Volume rendering of the dataset. (b) Identified tubular structures. Note that some of the “pathological” structures have been detected as tubular structures. (c) Tree reconstruction step showing the identified tubular structures belonging to the airway tree (blue), the discarded tubular structures (red), and the closed gaps (green). (d) Reconstructed airway tree.

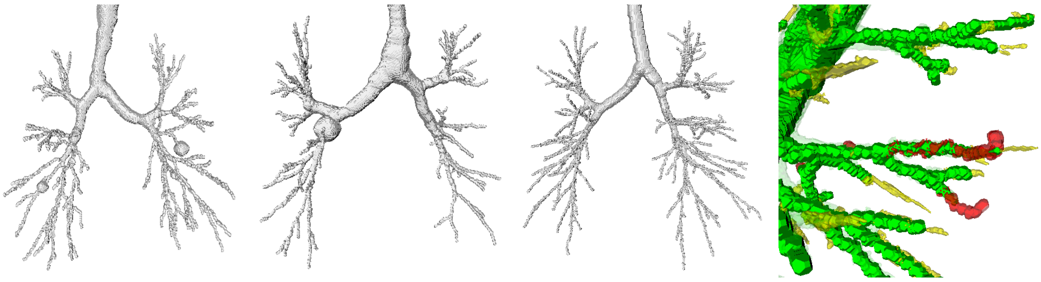

Figure 7.8: Examples of reconstructed airways with a high “leakage volume”. (a) CASE40: “leakage count”=17; “leakage volume”=3678.0 mm^3. (b) CASE25: “leakage count”=9; “leakage volume”=1693.0 mm^3. (c) CASE22: “leakage count”=23; “leakage volume”=1311.2 mm^3. (d) CASE22 comparison to gold standard: voxels classified as leakage (red), correct voxels (green), missed airways (yellow).

Chapter 8

Conclusion and Outlook

Contents

8.1 Conclusion

In this work we were dealing with the segmentation of 3D tubular tree structures in medical images. In the introduction, we outlined the general requirements and objectives for different applications in this field, emphasizing the importance of the structural correctness, and reviewed related work on vessel/airway segmentation. Based on that we presented a general approach for segmentation of branched tubular networks (Section 1.2) that puts a strong focus on the structural correctness of the segmentation results. The approach consists of a tube extraction step, a grouping and linkage step, and the actual tube segmentation step.

We developed and investigated methods for each of these processing steps, leading to a set of flexible methods that can be utilized in various applications. In particular, in Chapter 2 we developed a novel approach for detection of tubular objects based on the GVF that addresses limitations of these typically used Gaussian scale space based methods and compared it to promising TDFs known from the literature. In Chapter 3 we proposed two methods for grouping and linkage of unconnected tubular structures into tubular tree structures, one enabling an extraction of high quality centerlines in that deviate significantly from the typical tube shape, while the other one allows for a separation of interwoven tubular tree structures as well as handling of various kinds of disturbances.

In Chapter 4 we developed two methods to accurately segment the identified tubular tree structures, one solving the segmentation task in a globally optimal way, while the other one segments according to the first distinct edge closest to the centerline.

Based on these methods, different applications for segmentation of blood vessel trees (Chapter 5 and Chapter 6) and airway trees (Chapter 7) in CT datasets were developed. The methods were evaluated on larger sets of clinical datasets and comparisons to results achieved with other methods developed for the same task were presented.

In Chapter 5 we developed a system for the segmentation of the livers vascular trees in contrast CT datasets. The task requires a separation of multiple interwoven tubular tree structures, a robustness against disease such as tumorous regions, and the ability to cope with poor contrast agent distributions. In particular, the separation of interwoven tubular tree structures in case of unconnected tubular objects has not been addressed in this area before, while our newly developed grouping method (Section 3.2) allows coping with this case. For evaluation of the method CT datasets of a plastic phantom and clinical datasets were used. On the phantom datasets we presented quantitative results by comparison with the ground truth, while for the clinical datasets an experienced radiologist verified the correctness and accuracy of the segmentations. The results show a high robustness of our approach against disturbances, the methods ability to successfully reconstruct, separate, and accurately segment multiple interwoven tubular tree structures in this application domain. For comparison to other methods we reimplemented the methods of Selle et al. [130] and Manniesing et al. [94] in part and presented qualitative differences, showing that with our approach more of the thinner blood vessels can be segmented and that with the other methods additional user interaction would be necessary to achieve a valid separation of the different vascular trees.

In Chapter 6 we presented a system for the extraction of the coronary artery trees based on a centerline description. The main difficulties with this task are closely adjacent vessels or calcifications, the proximity of the heart chambers, and regions where locally the vessels are partly indistinguishable from the background (e.g. due to occlusions or imaging artifacts). Due to these difficulties, conventional TDFs were not applicable while our developed GVF-based TDF (Section 2.3) allows coping with these cases of varying backgrounds. As the evaluation on clinical datasets from a publicly available database with reference centerlines shows, our method allows for a reliable extraction of the coronary artery centerlines, comparable to the performance of a human observer [124]. Compared to other methods, only methods that utilized information about the endpoint of the coronary arteries – information not available in practice – performed better with respect to the extraction capability. Regarding centerline accuracy, an average centerline distance of about one voxel as achieved.

In Chapter 7 we presented two approaches for the segmentation of airway trees in CT datasets. With this task, one has to cope with the differentiation from the actual lung tissue, disease such as emphysema or stenosis due to tumorous regions, as well as with a large variation in data quality as the imaging protocols are not always adapted for the main purpose of airway segmentation. The two developed methods show different advantages. While one method produces immediately accurate segmentations and allows for an additional extraction of the associated curve skeleton in a straight forward manner, the other one allows handling of local disturbances and shows a higher robustness in case of disease. As the evaluation and comparison to other methods on clinical datasets of a publicly available showed [88], both methods perform about comparably well in practice, and are among the best performing methods known in the literature. Only one other approach allows for an extraction of more airway branches while having a lower leakage volume; however, to the cost of about one hour of manual user interaction.

The reasons for the robustness of the developed applications is related with the presented general approach for segmentation of branched tubular networks (Section 1.2), that puts a strong focus on the structural correctness of the segmentation results and considers handling of different kinds of disturbances directly as part of the approach. Considering other methods, as discussed in the related work part (Section 1.1), "practically all currently used vessel segmentation methods are based on a growth process emanating from an automatically- or user-defined start point; the differences between the methods lie in the constraints imposed on the growth process" [47]. Contrary to that, our approach does not proceed form a single seed but performs a bottom-up extraction of tubular structures with a grouping/linkage of these structures into a connected network. During the grouping additional prior knowledge about tubular tree structures is incorporated: The individual tubular structures of a branched tubular network are connected with each other and – from a biological perspective – they have to be supplied. Utilizing this information, cases can be resolved, where a typical vessel/airway model may be inadequate, such that the structure of the tubular tree structures can be obtained correctly and later on used for a more accurate segmentation.

In the literature only very few methods can be found that follow this paradigm of extraction and grouping of tubular structures. To the best of our knowledge, besides the seminal ideas of Beichel et al. [10, 113], only the works of Szymszack et al. [138], Florin et al. [39], and Graham et al. [50] presented applications using similar ideas. However, none of these methods has been evaluated on larger sets of clinical datasets or compared to other methods.

As seen from the applications summarized above, the objectives and problems that have to be addressed in such application areas for segmentation of tubular tree structures are very diverse and challenging. But with the proposed general approach for segmentation of branched tubular networks (Section 1.2) and the set of developed methods most of the problems occurring in such kinds of datasets can be addressed and the developed methods proofed to be suitable for different application domains.

8.2 Directions for Future Work

The general framework and the methods we have developed in this thesis provide a flexible basis for future work in the area of vessel/airway segmentation. It can be adapted to other applications or requirements by replacing or improving individual parts (of our three-step approach). Besides the application and evaluation of the already developed methods in other application areas, we see primarily two further directions for possible future work:

Improvement of the robustness of the tube extraction approach: The extraction of tubular structures is the first and most critical part of the overall approach. For larger tubular structures, the presented methods perform well and the developed methods also proofed sufficient for identification of thinner low-contrast vessels in liver and coronary CT datasets (Sections 5 and 6). However, in case of airways still about 1/3 of the airways remain undetected (Section 7). The reasons for this behavior are the complex background in lung CT datasets and the fact that even smaller local disturbances can lead to problems in combination with the used height-ridge traversal procedure and the hysteresis-thresholding (Section 2.4). One may consider to enhance the robustness of the tube extraction method for smaller airways either by appropriate pre-processing of the datasets, post-processing TDF results, or by incorporating additional airway-specific prior knowledge into the airway detection. Therefor, pre-processing techniques for noise suppression specifically developed for tubular structures such as “vessel enhancing diffusion” [95] or “flux-based anisotropic diffusion” [66] could be used. Possible TDF result post-processing methods could combine local evidence about candidate airways by taking their elongated structure into account. This could be based on “improved structure tensors” [65], “tensor voting” [139], “vessel enhancing diffusion” [95], or similar techniques. The last point is that airways can be characterized locally not only as a dark structure surrounded by brighter tissue as assumed by our methods in Section 7, but they are surrounded by an airway wall of a certain thickness. Incorporating properties of this airway wall would enhance the selective of the airway extraction.

Visualization and user interaction: Although a fully automated segmentation of the tubular tree structures without the need for any user interaction is desirable, there may still remain cases in clinical practice where fully automated methods may fail. Therefore, to be clinically applicable, a system also has to be able to cope with such cases in a semi-automated way. Our developed general approach performs a bottom-up identification of all tube-like structures in a given volume of interest, such that the overall system is aware of potential problems (e.g. identified but unconnected sub-trees). Combined with an appropriate 3D visualization this allows giving a user feedback about potential errors. The user could then easily verify such situations and in case of errors manual correction could be used as such cases occur only very rarely. This behavior of our general approach that allows handling of such errors (unconnected sub-trees) is in contrast to other conventional tubular tree structure segmentation approaches that simply discard the remaining tree parts, which is a severe drawback of conventional tube extraction schemes.

Appendix A

List of Publications

In this appendix we give a list of relevant publications that resulted from the work on this thesis [4–9, 105, 119, 124]. They are roughly sorted by importance:

- Bauer, C., Pock, T., Sorantin, E., Bischof, H., and Beichel, R. (2010). Segmentation of interwoven 3d tubular tree structures utilizing shape priors and graph cuts. Medical Image Analysis, vol. 14, pages 174–184.
- Bauer, C. and Bischof, H. (2008c). A novel approach for detection of tubular objects and its application to medical image analysis. In DAGM Symposium on Pattern Recognition, pages 163–172.
- Bauer, C. and Bischof, H. (2008b). Extracting curve skeletons from gray value images for virtual endoscopy. In Workshop on Medical Imaging and Augmented Reality, pages 393–402.
- Bauer, C., Bischof, H., and Beichel, R. (2009a). Segmentation of airways based on gradient vector flow. In International Workshop on Pulmonary Image Analysis, Medical Image Computing and Computer Assisted Intervention, pages 191–201.
- Bauer, C., Pock, T., Bischof, H., and Beichel, R. (2009b). Airway tree reconstruction based on tube detection. In International Workshop on Pulmonary Image Analysis, Medical Image Computing and Computer Assisted Intervention, pages 203–213.
- Bauer, C. and Bischof, H. (2008a). Edge based tube detection for coronary artery centerline extraction. The Midas Journal.

- Schaap, M. et al. (2009). Standardized evaluation methodology and reference database for evaluating coronary artery centerline extraction algorithms. Medical Image Analysis, vol. 13, pages 701–714.
- Muhl, J., Kainz, B., Portugaller, R., Stiegler, P., and Bauer, C. (2009). Computer oriented image acquisition of the liver: Toward a better numerical model for radiofrequency ablation. In IEEE Engineering in Medicine and Biology Society Annual Conference, pages 3755–3758.
- Reinbacher, C., Pock, T., Bauer, C., and Bischof, H. (2010). Variational segmentation of elongated volumetric structures. In Computer Vision and Pattern Recognition. (in print)

Appendix B

List of Acronyms

`a.k.a.`	also known as
`CS`	curve skeleton
`CT`	computer thomography
`CTA`	computer thomography angiography
`GPU`	graphics processing unit
`GVF`	Gradient Vector Flow
`MinIP`	minimum intensity projection
`MIP`	maximum intensity projection
`MR`	magnetic resonance
`MRI`	magnetic resonance imaging
`ROI`	region of interest
`SNR`	signal to noise ratio
`vs.`	versus

Bibliography

[1] Agam, G., Armato, S. G., and Wu, C. (2005). Vessel tree reconstruction in thoratic CT scans with application to nodule detection. *IEEE Trans. Med. Imag.*, 24(4):486–499.

[2] Aylward, S. and Bullit, E. (2002). Initialization, noise, singularities, and scale in height ridge traversal for tubular object centerline extraction. *IEEE Trans. Med. Imag.*, 21(2):61–75.

[3] Aylward, S., Bullitt, E., Pizer, S., and Eberly, D. (1996). Intensity ridge and widths for tubular object segmentation and description. *Proc. IEEE Math. Meth. Biomed. Image Anal.*, pages 131–138.

[4] Bauer, C. and Bischof, H. (2008a). Edge based tube detection for coronary artery centerline extraction. *The Midas Journal*.

[5] Bauer, C. and Bischof, H. (2008b). Extracting curve skeletons from gray value images for virtual endoscopy. In *Workshop on Medical Imaging and Augmented Reality*, pages 393–402.

[6] Bauer, C. and Bischof, H. (2008c). A novel approach for detection of tubular objects and its application to medical image analysis. In *DAGM Symposium on Pattern Recognition*, pages 163–172.

[7] Bauer, C., Bischof, H., and Beichel, R. (2009a). Segmentation of airways based on gradient vector flow. In *International Workshop on Pulmonary Image Analysis*, Medical Image Computing and Computer Assisted Intervention, pages 191–201.

[8] Bauer, C., Pock, T., Bischof, H., and Beichel, R. (2009b). Airway tree reconstruction based on tube detection. In *International Workshop on Pulmonary Image Analysis*, Medical Image Computing and Computer Assisted Intervention, pages 203–213.

[9] Bauer, C., Pock, T., Sorantin, E., Bischof, H., and Beichel, R. (2010). Segmentation of interwoven 3d tubular tree structures utilizing shape priors and graph cuts. *Medical Image Analysis*, 14:174–184.

[10] Beichel, R., Pock, T., Janko, C., Zotter, R., Reitinger, B., Bornik, A., Palágyi, K., Sorantin, E., Werkgartner, G., Bischof, H., and Sonka, M. (2004). Liver segment approximation in CT data for surgical resection planning. In *Medical Imaging 2004: Image Processing*, pages 1435–1446, San Diego, CA, USA.

[11] Bennink, H. E., van Assen, H. C., ter Wee, R., Spaan, J. A. E., and ter Haar Romeny, B. M. (2007). A novel 3D multi-scale lineness filter for vessel detection. In *Proc. of MICCAI*, pages 436–443, Brisbane, Australia.

[12] Blum, H. (1967). A transformation for extracting new descriptors of shape. In *Models Percept. Speech Visual Form*, pages 362–380.

[13] Born, S., Iwamaru, D., Pfeifle, M., and Bartz, D. (2009). Three-step segmentation of the lower airways with advanced leakage-control. In *International Workshop on Pulmonary Image Analysis*, Medical Image Computing and Computer Assisted Intervention, pages 239–250.

[14] Boskamp, T., Rinck, D., Link, F., Knmmerlen, B., Stamm, G., and Mildenberger, P. (2004). New vessel analysis tool for morphometric quantification and visualization of vessels in ct and mr imaging data sets. *Radiographics*, 24:287–297.

[15] Bouix, S., Siddiqi, K., and Tannenbaum, A. (2005). Flux driven automatic centerline extraction. *Medical Image Analysis*, 9(3):209–221.

[16] Bouix, S., Tannenbaum, A., Siddiqi, K., , and Zucker, S. (2002). Hamilton–jacobi skeletons. *Int. J. Comput. Vision*, 48(3):215–231.

[17] Boykov, Y. and Jolly, M.-P. (2001). Interactive graph cuts for optimal boundary & region segmentation of objects in n-d images. In *Proc. of ICCV*, pages 105–112, Vancouver, Canada.

[18] Bullitt, E., Aylward, S., Smith, K., Jukherji, S., Jiroutek, M., and Muller, K. (2001). Symbolic description of intracerebral vessels segmented from magnetic resonance angiograms and evaluation by comparision with x-ray angiograms. *Medical Image Analysis*, 5(2):157–169.

[19] Cai, W., Dachille, F., Harris, G., and Yoshida, H. (2006). Vesselness propagation: a fast interactive vessel segmentation method. In *Proc. SPIE Med. Imaging*, pages 1343–1351.

[20] Castro, C., Luengo-Oroz, M. A., Santos, A., and Ledesma-Carbayo, M. J. (2008). Coronary artery tracking in 3D cardiac CT images using local morphological reconstruction operators. *The Midas Journal.*

[21] Choyke, P., Yim, P., Marcos, H., Ho, V., Mullick, R., and Summers, R. (2001). Hepatic MR angiography: a multiobserver comparison of visualization methods. *Am. J. Roentgenolog.*, 176(2):465–570.

[22] Chuang, C.-H. and Lie, W.-N. (2004). A downstream algorithm based on extended gradient vector flow field for object segmentation. *IEEE Trans. Med. Imag.*, 13(10):1379–1392.

[23] Chung, A., Noble, J., and Summers, P. (2004). Vascular segmentation of phase contrast magnetic resonance angiograms based on statistical mixture modeling and local phase coherence. *IEEE Trans. Med. Imaging*, 23(12):1490–1507.

[24] Cohen, L. D. and Deschamps, T. (2001). Grouping connected components using minimal path techniques. In *Comput Vision and Pattern Recognition 2001*, pages 102–109.

[25] Cormen, T. H., Leiserson, C., and Rivest, R. L. (1990). *Introduction to Algorithms (MIT Electrical Engineering and Computer Science)*. The MIT Press.

[26] de Bruijne, M., van Ginneken, B., Niessen, W., Loog, M., and Viergever, M. (2003a). Model-based segmentation of abdominal aortic aneurysms in CTA images. In *Proc. SPIE Med. Imaging*, pages 1560–1571.

[27] de Bruijne, M., van Ginneken, B., Niessen, W., and Viergever, M. (2003b). Adapting active shape models for 3D segmentation of tubular structures in medical images. In *Proc. Inf. Process. Med. Imaging*, pages 136–147.

[28] Delingette, H. and Montagnat, J. (2001). Shape and topology constraints on parametric active contours. *Comput. Vision Image Understan.*, 83(2):140–171.

[29] Deschamps, T. and Cohen, L. (2002). Grouping connected components using minimal path techniques. In *Mathematics and Visualization*, pages 102–109.

[30] Dikici, E., OâDonnell, T., Grady, L., Setser, R., and White, R. D. (2008). Coronary artery centerline tracking using axial symmetries. *The Midas Journal.*

[31] Dokládal, P., Lohou, C., Perroton, L., and Bertrand, G. (1999). Liver blood vessels extraction by a 3-D topological approach. In *Proc. of MICCAI*, pages 98–105, London, UK.

[32] Dou, X., Wu, X., Wahle, A., and Sonka, M. (2009). Globally optimal surface segmentation using regional properties of segmented objects. In *Proc. of SPIE*, Lake Buena Vista, FL, USA.

[33] Erdt, M., Raspe, M., and Suehling, M. (2008). Automatic hepatic vessel segmentation using graphics hardware. In *Workshop on Medical Imaging and Augmented Reality*, pages 403–412.

[34] Fabianska, A. (2009). Two-pass region growing algorithm for segmenting airway trees from MDCT chest scans. *Comput. Med. Imaging Graphics*, 23(11):1353–1364.

[35] Fabijanska, A. (2009). Results of applying two-pass region growing algorithm for airway tree segmentation to MDCT chest scans from EXACT database. In *International Workshop on Pulmonary Image Analysis*, Medical Image Computing and Computer Assisted Intervention, pages 251–260.

[36] Fetita, C., Ortner, M., Brillet, P.-Y., Preteux, F., and Grenier, P. (2009). A morphological-aggregative approach for 3D segmentation of pulmonary airways from generic MSCT acquisitions. In *International Workshop on Pulmonary Image Analysis*, Medical Image Computing and Computer Assisted Intervention, pages 215–226.

[37] Fetita, C. I., Preteux, F., Beigelman-Aubry, C., and Grenier, P. (2004). Pulmonary airways: 3-D reconstruction from multiscale CT and clinical investigation. *IEEE Trans. Med. Imag.*, 23(11):1353–1364.

[38] Feuerstein, M., Kitasaka, T., and Mori, K. (2009). Adaptive branch tracing and image sharpening for airway tree extraction in 3-d chest ct. In *International Workshop on Pulmonary Image Analysis*, Medical Image Computing and Computer Assisted Intervention, pages 273–284.

[39] Florin, C., Moreau-Gobard, R., and Williams, J. (2004). Automatic heart peripheral vessel segmentation based on a normal MIP raycasting technique. In *Proc. of MICCAI*, pages 483–490.

[40] Florin, C., Paragios, N., and Williams, J. (2005). Particle filters, a quasi-monte carlo solution for segmentation of coronaries. In *Proc. Med. Image Comput. Assist. Interv.*, pages 246–253.

[41] Florin, C., Paragios, N., and Williams, J. (2006). Globally optimal active contours, sequential monte carlo and on-line learning for vessel segmentation. In *Proc. of ECCV*, pages 476–489, Graz, Austria.

[42] Frangi, A., Niessen, W., Nederkoorn, P., Elgersma, O., and Viergever, M. (2000). Three-dimensional model-based stenosis quantification of the carotid arteries from contrast-enhance MR angiography. In *Proc. IEEE Math. Meth. Biomed. Image Anal.*, pages 110–118.

[43] Frangi, A. F., Niessen, W. J., Hoogeveen, R. M., van Walsum, T., and Virgever, M. A. (1999). Model-based quantitation of 3-d magnetic resonance angiography images. *IEEE Trans. Med. Imag.*, 18(10):946–956.

[44] Frangi, A. F., Niessen, W. J., Vincken, K. L., and Viergever, M. A. (1998). Multiscale vessel enhancement filtering. In *Medical Image Computing and Computer-Assisted Interventation â MICCAI 1998*, pages 130–137.

[45] Fridman, Y., Pizer, S., Aylward, S., and Bullitt, E. (2003). Segmenting 3D branching tubular structures using cores. In *Proc. Med. Image Comput. Assist. Interv.*, pages 570–577.

[46] Fridman, Y., Pizer, S. M., Aylward, S., and Bullitt, E. (2004). Extracting branching tubular objects geometry via cores. *Medical Image Analysis*, 8(3):169–176.

[47] Friman, O., Hindennach, M., Kuehnel, C., and Peitgen, H.-O. (2010). Multi hypothesis template tracking of small 3D vessel structures. *IEEE Trans. Med. Imag.*, 14:160–171.

[48] Friman, O., Hindennach, M., and Peitgen, H.-O. (2008a). Template-based multiple hypotheses tracking of small vessels. In *Proc. IEEE Int. Symp. Biomed. Imaging*, pages 1047–1050.

[49] Friman, O., Kuhnel, C., and Peitgen, H.-O. (2008b). Coronary centerline extraction using multiple hypothesis tracking and minimal paths. *The Midas Journal.*

[50] Graham, M. W., Gibbs, J. D., and Higgins, W. E. (2008). Robust system for human airway-tree segmentation. In *Proc. of SPIE Med. Imag.*

[51] Gulsun, M. and Tek, H. (2008). Robust vessel tree modeling. In *Proc. Med. Image Comput. Assist. Interv*, pages 602–611.

[52] Hassouna, M., Farag, A., Hushek, S., and Moriarty, T. (2003). Statistical-based approach for extracting 3d blood vessels from TOF-myra data. In *Proc. Med. Image Comput. Assist. Interv*, pages 680–687.

[53] Hassouna, M. S. and Farag, A. A. (2007). On the extraction of curve skeletons using gradient vector flow. In *Proc. of ICCV*, pages 1–8, Rio de Janeiro, Brazil.

[54] Hassouna, M. S. and Farag, A. A. (2009). Variational curve skeletons using gradient vector flow. *IEEE Transactions on Pattern Analysis and Machine Intelligence*, 31(12):2257–2274.

[55] Hassouna, M. S., Farag, A. A., and Falk, R. (2005). Differential fly-throughs (DFT): A general framework for computing flight paths. In *Proc. of MICCAI*, pages 654–661, London, UK.

[56] Hoyos, M. H., Zuluaga, M. A., Lozano, M., Prieto, J. C., Douek, P. C., Magnin, I. E., and Orkisz, M. (2008). Coronary centerline tracking in CT images with use of an elastic model and image moments. *The Midas Journal*.

[57] Irving, B., Taylor, P., and Todd-Pokropek, A. (2009). 3D segmentation of the airway tree using a morphology based method. In *International Workshop on Pulmonary Image Analysis*, Medical Image Computing and Computer Assisted Intervention, pages 297–307.

[58] Jomir, J., LeDigarcher, V., and Aylward, S. (2005). Automatic vascular tree formulation using the mahalanobis distance. In *Proc. of MICCAI*, pages 806–812.

[59] Kass, M., Witkin, A., and Terzopoulos, D. (1987). Snakes: Active contour models. *Int. J. Comput. Vision*, 1:321–331.

[60] Kimmel, R. and Bruckstein, A. (2003). Regularized laplacian zero crossings as optimal edge integrators. *Int. J. Comput. Vision*, 53(3):225–243.

[61] Kimmel, R., Peled, N., Holtzman-Gazit, M., and Goldsher, D. (2006). Segmentation of thin structures in volumetric medical images. *IEEE Trans. Image Process.*, 15(2):354–363.

[62] Kirbas, C. and Quek, F. (2003). A review of vessel extraction techniques and algorithms. *IEEE Trans. Med. Imag.*, 20(2):117–131.

[63] Kitslaar, P. H., Frenay, M., Oost, E., Dijkstra, J., Stoel, B., and Reiber, J. H. (2008). Connected component and morpholgy based extraction of arterial centerlines of the heart (CocomoBeach). *The Midas Journal*.

[64] Koller, T., Gerig, G., Székely, G., and Dettwiler, D. (1995). Multiscale detection of curvilinear structures in 2D and 3D image data. In *Proc. IEEE Int. Conf. Comput. Vision*, pages 864–869.

[65] Köthe, U. (2003). Edge and junction detection with an improved structure tensor. In *Deutsche Arbeitsgemeinschaft für Mustererkennung-Symposium*, pages 25–32.

[66] Krissian, K. (2002). Flux-based anisotropic diffusion applied to enhancement of 3-D angiogram. *IEEE Trans. Med. Imaging*, 21(11):1440–1442.

[67] Krissian, K., Bogunovi, H., Pozo, J., Villa-Uriol, M., and Frangi, A. (2008). Minimally interactive knowledge-based coronary tracking in CTA using a minimal cost path. *The Midas Journal*.

[68] Krissian, K., Ellsmere, J., Vosburgh, K., Kikinis, R., and Westin, C.-F. (2003). Multiscale segmentation of the aorta in 3d ultrasound images. In *Engineering in Medicine and Biology Society, 2003. Proceedings of the 25th Annual International Conference of the IEEE*, pages 1720–1729, Cancun, Mexico.

[69] Krissian, K. and Farneback, G. (2005). Building reliable clients and servers. In Leondes, C. T., editor, *Medical Imaging Systems Technology: Methods in Cardiovascular and Brain Systems*. Singapore: World Scientific Publishing Co.

[70] Krissian, K., Malandain, G., Ayache, N., Vaillant, R., and Trousset, Y. (2000a). Model-based detection of tubular structures in 3D images. *Computer Vision and Image Understanding*, 2(80):130–171.

[71] Krissian, K., Malandain, G., Ayache, N., Vaillant, R., and Trousset, Y. (2000b). Model-based detection of tubular structures in 3D images. *Computer Vision and Image Understanding*, 80(2):130–171.

[72] Lacoste, C., Finet, G., and Magnin, I. (2006). Coronary tree extraction from X-ray angiograms using marked point processes. In *IEEE Int. Symp. Biomed. Imaging*, pages 157–160.

[73] Law, M. and Chung, A. (2008). Three dimensional curvilinear structure detection using optimally oriented flux. In *Eur. Conf. Comput. Vision*, pages 368–382.

[74] Law, M. and Chung, A. (2009). Efficient implementation for spherical flux computation and its application to vascular segmentation. *IEEE Trans. Image Process*, 18(3):596–612.

[75] Lee, J., Beighley, P., Ritman, E., and Smith, N. (2007). Automatic segmentation of 3d micro-ct coronary vasular images. *Medical Image Analysis*, 11(4):630–647.

[76] Lee, J. and Reeves, A. P. (2009). Segmentation of the airway tree from chest CT using local volume of interest. In *International Workshop on Pulmonary Image Analysis*, Medical Image Computing and Computer Assisted Intervention, pages 333–340.

[77] Lei, T., Uduapa, J. K., Saha, P. K., and Odhner, D. (2001). Artery-vein separation via MRA – an image processing approach. *IEEE Trans. Med. Imag.*, 20(8):689–703.

[78] Lesage, D., Angelini, E., Bloch, I., and Funka-Lea, G. (2008). Medial-based bayesian tracking for vascular segmentation: Application to coronary arteries in 3d CT angiography. In *Proc. IEEE Int. Symp. Biomed. Imaging*, pages 268–271.

[79] Lesage, D., Angelini, E. D., Bloch, I., and Funka-Lea, G. (2009). A review of 3d vessel lumen segmentation techniques: Models, features and extraction schemes. *Medical Image Analysis*, 13:819–845.

[80] Li, G., Liu, T., Tarokh, A., Nie, J., Guo, L., Mara, A., Holley, S., and Wong, S. (2007). 3D cell nuclei segmentation based on gradient flow tracking. *BMC Cell Biology*, 8(40).

[81] Li, H. and Yezzi, A. (2006). Vessels as 4D curves: global minimal 4D paths to extract 3D tubular surfaces. In *Proc. IEEE Conf. Comput. Vision Pattern Recognit.*, pages 1213–1223.

[82] Li, H. and Yezzi, A. (2007). Vessels as 4-d curves: Global minimal 4-d paths to extract 3-d tubular surfaces and centerlines. *IEEE Trans. Med. Imag.*, 26(9):1213–1223.

[83] Lin, Q. (2003). *Enhancement, Detection, and Visualization of 3D Volume Data.* PhD thesis, Dept. EE, Linköping University.

[84] Lindeberg, T. (1994). *Scale-Space Theory in Computer Vision.* Kluwer Academic Publishers.

[85] Lindeberg, T. (1998). Edge detection and ridge detection with automatic scale selection. *International Journal of Computer Vision*, 30(2):117–156.

[86] Lo, P. and de Brujine, M. (2008). Voxel classification based airway tree segmentation. In *Proc. of SPIE Med. Imag.*

[87] Lo, P., Sporring, J., and de Bruijne, M. (2009). Multiscale vessel-guided airway tree segmentation. In *International Workshop on Pulmonary Image Analysis*, Medical Image Computing and Computer Assisted Intervention, pages 323–332.

[88] Lo, P., van Ginneken, B., Reinhardt, J. M., and de Bruijne, M. (2010). Extraction of airways from CT (EXACT'09). In *International Workshop on Pulmonary Image Analysis*, volume 14 of *Medical Image Computing and Computer Assisted Intervention*, pages 175–189.

[89] Lorenz, C., Carlsen, I.-C., Buzug, T. M., Fassnacht, C., and Weese, J. (1997). Multiscale line segmentation with automatic estimation of width, contrast and tangential direction in 2d and 3d medical images. In *CVRMed-MRCAS '97*, pages 233–242, London, UK. Springer-Verlag.

[90] Lorigo, L., Faugerasa, O., Grimsona, W., Kerivenc, R., Kikinisd, R., Nabavid, A., and Westin, C. (2001). Curves: Curve evolution for vessel segmentation. *Medical Image Analysis*, 5(3):195–206.

[91] Luboz, V., Wu, X., Krissian, K., Westin, C.-F., Kikinis, R., Cotin, S., and Dawson, S. (2005). A segmentation and reconstruction technique for 3d vascular structures. In *Proc. Med. Image Comput. Assist. Interv.*, pages 43–50.

[92] Malandain, G., Bertrand, G., and Ayache, N. (1993). Toplogical segmentation of discrete surfaces. *Int. J. Comput. Vision*, 2:183–197.

[93] Manniesing, R. and Niessen, W. (2004). Local speed functions in level set based vessel segmentation. In *Proc. Med. Image Comput. Assist. Interv.*, pages 475–482.

[94] Manniesing, R., Velthuis, B., M.S., van Leeuwen, van der Schaaf, I., van Laar, P., and Niessen, W. (2006a). Level set based cerebral vasculature segmentation and diameter quantification in CT angiography. *Medical Image Analysis*, 10(2):200–214.

[95] Manniesing, R., Viergever, M., and Niessen, W. (2006b). Vessel enhancing diffusion: A scale space representation of vessel structures. *Medical Image Analysis*, 19:815–825.

[96] McInerney, T. and Terzopoulos, D. (1996). Deformable models in medical image analysis: a survey. *Med. Image Anal.*, 1:91–108.

[97] McInerney, T. and Terzopoulos, D. (1999). Topology adaptive deformable surfaces for medical image volume segmentation. *IEEE Trans. Med. Imaging*, 18:840–850.

[98] McInerney, T. and Terzopoulos, D. (2000). T-snakes: topology adaptive snakes. *Med. Image Anal.*, 4(2):73–91.

[99] Meinzer, H.-P., Thorn, M., and Cardenas, C. (2002). Computerized planning of liver surgery - an overview. *Computers & Graphics*, 24(6):569–576.

[100] Mendoza, C. S., Acha, B., and Serrano, C. (2009). Maximal contrast adaptive region growing for CT airway tree segmentation. In *International Workshop on Pulmonary Image Analysis*, Medical Image Computing and Computer Assisted Intervention, pages 285–295.

[101] Metz, C., Schaap, M., van der Giessen, A., van Walsum, T., and Niessen, W. (2007). Semi-automatic coronary artery centerline extraction in computed tomography angiography data. In *Proc. IEEE Int. Symp. Biomed. Imaging*, pages 856–859.

[102] Metz, C., Schaap, M., van Walsum, T., and Niessen, W. (2008). Two point minimum cost path approach for CTA coronary centerline extraction. *The Midas Journal.*

[103] Mille, J. and Cohen, L. (2009). Deformable tree models for 2D and 3D braching structures extraction. In *Poc. IEEE Math. Methods Biomed. Image Anal.*

[104] Montagnat, J. (1999). *Deformable Modeling for 3D and 4D Medical Image Segmentation.* PhD thesis, Nice - Sohpia Antipolis University, Nice, France.

[105] Mühl, J., Kainz, B., Portugaller, R., Stiegler, P., and Bauer, C. (2009). Computer oriented image acquisition of the liver: Toward a better numerical model for radiofrequency ablation. In *IEEE Engineering in Medicine and Biology Society Annual Conference*, pages 3755–3758.

[106] Nain, D., Yezzi, A., and Turk, G. (2004). Vessel segmentation using a shape driven flow. In *Proc. of MICCAI*, pages 51–59.

[107] O'Donnell, T., Boult, T., Fang, X., and Gupta, A. (1994). The extruded generalized cylinder: a deformable model for object recovery. In *Proc. IEEE Conf. Comput. Vision Pattern Recognit.*, pages 174–181.

[108] O'Donnell, T., Dubuisson-Jolly, M.-P., and Gupta, A. (1998). A cooperative framework for segmentation using 2D active contours and 3D hybrid models as applied to branching cylindrical structures. In *IEEE Int. Conf. Comput. Vision*, pages 454–459.

[109] Palagyi, K. and Kuba, A. (1998). A 3D 6-subiteration thinning algorithm for extracting medial lines. *Pattern Recognit. Lett.*, 19:613–627.

[110] Palágyi, K., Sorantin, E., Balogh, E., Kuba, A., Halmai, C., Erdohelyi, B., and Hausegger, K. (2001). A sequential 3D thinning algorithm and its medical applications. In *IPMI 2001*, pages 409–415. Springer-Verlag Heidelberg.

[111] Passat, N., Ronse, C., Baruthio, J., Armspach, J.-P., and Maillot, C. (2006). Magnetic resonance angiography: from anatomical knowledge modeling to vessel segmentation. *Med. Image Anal.*, 10(2):259–274.

[112] Pinho, R., Luyckx, S., and Sijbers, J. (2009). Robust region growing based intrathoracic airway tree segmentation. In *International Workshop on Pulmonary Image Analysis*, Medical Image Computing and Computer Assisted Intervention, pages 261–271.

[113] Pock, T. (2004). Robust segmentation of tubular structures in 3d volume data. Master's thesis, Graz University of Technology.

[114] Pock, T., Beichel, R., and Bischof, H. (2005). A novel robust tube detection filter for 3d centerline extraction. In *Proceedings of the 14th Scandinavian Conference on Image Analysis*, pages 481–490. Springer LNCS.

[115] Pudney, C. (1998). Distance-ordered homotopic thinning: a skeletonization algorithm for 3D digital images. *Comput. Vision Image Understan.*, 72(3):404–413.

[116] Puig, A., Tost, D., and Navazo, I. (1997). An interactive cerebral blood vessel exploration system. In *Proc. IEEE Visualization*, pages 433–436.

[117] Quek, F. K. H. and Kirbas, C. (2001). Vessel extraction in medical images by wave-propagation and traceback. *IEEE Trans. Med. Imag.*, 20(2):117–131.

[118] R., B. E. S., Aylward, E., Liu, A., Stone, J., Mukherji, S., Coffey, C., Gerig, G., and Pizer., S. (1999). 3D graph description of the intracerebral vasculature from segmented MRA and tests of accuracy by comparison with x-ray angiograms. In *Proc. Inf. Process. Med. Imaging*, pages 308–321.

[119] Reinbacher, C., Pock, T., Bauer, C., and Bischof, H. (2010). Variational segmentation of elongated volumetric structures. In *Computer Vision and Pattern Recognition.*

[120] Reitinger, B., Bornik, A., Beichel, R., and Schmalstieg, D. (2006). Liver surgery planning using virtual reality. *IEEE Comput. Graph. Appl.*, 26(6):36–47.

[121] Sato, Y., Araki, T., Hanayama, M., Naito, H., and Tamura, S. (1998a). A viewpoint determination system for stenosis diagnosis and quantification in coronary angiographic image acquisition. *IEEE Trans. Med. Imaging*, 17(1):121–137.

[122] Sato, Y., Nakajima, S., Atsumi, H., Koller, T., Gerig, G., Yoshida, S., and Kikinis, R. (1997). 3D multi-scale line filter for segmentation and visualization of curvilinear structures in medical images. In *CVRMed-MRCAS*, pages 213–222.

[123] Sato, Y., Nakajima, S., Shiraga, N., Atsumi, H., Yoshida, S., Koller, T., Gerig, G., and Kikinis, R. (1998b). Three-dimensional multi-scale line filter for segmentation and visualization of curvilinear structures in medical images. *Medical Image Analysis*, 2(2):143–168.

[124] Schaap, M. et al. (2009a). Standardized evaluation methodology and reference database for evaluating coronary artery centerline extraction algorithms. *Medical Image Analysis*, 13:701–714.

[125] Schaap, M., Manniesing, R., Smal, I., van Walsum, T., van der Lugt, A., and Niessen., W. (2007a). Bayesian tracking of tubular structures and its application to carotid arteries in CTA. In *Proc. Med. Image Comput. Assist. Interv.*, pages 562–570.

[126] Schaap, M., Smal, I., Metz, C., van Walsum, T., and Niessen, W. (2007b). Bayesian tracking of elongated structures in 3d images. In Karssemeijer, N. and Lelieveldt, B., editors, *Information Processing in Medical Imaging, 20th International Conference, IPMI 2007, Maastricht, NL, July 2-6, 2007*, pages 74–85.

[127] Schaap, M., Smal, I., Metz, C., van Walsum, T., and Niessen, W. (2009b). Coronary lumen segmentation using graph cuts and robust kernel regression. In *Proc. of Information Processing in Medical Imaging*, pages 528–539.

[128] Schlathalter, T., Lorenz, C., Carlsen, I., Reinisch, S., and Deschamps, T. (2002). Simultaneous segmentation and tree reconstruction of the airways for virtual bronchoscopy. In *Proc. of SPIE Med. Imag.*, pages 103–113.

[129] Schmugge, S. J., Keller, S., Nguyen, N., Souvenir, R., Huynh, T., Clemens, M., and Shin, M. C. (2008). Segmentation of vessels cluttered with cells using a physics based model. In *Proc. of MICCAI*, pages 127–134.

[130] Selle, D., Preim, B., and Peitgen, H. (2002). Analysis of vasculature for liver surgical planning. *IEEE Trans. Med. Imag.*, 21(11):1344–1357.

[131] Shikata, H., Hoffman, E., and Sonka, M. (2004). Automated segmentation of pulmonary vascular tree from 3D CT images. In *Proc. SPIE Med. Imaging*, pages 107–116.

[132] Sluimer, I., Schilham, A., Prokop, M., and van Ginneken, B. (2006). Computer analysis of computed tomography scans of the lung: A survey. *IEEE Trans. Med. Imag.*, 25(4):385–405.

[133] Soler, L., Delingette, H., Malandain, G., Montagnat, J., Ayache, N., Clement, J.-M., Koehl, C., Dourthe, O., Mutter, D., and Marescaux, J. (2000). A fully automatic anatomical, pathological and functional segmentation from ct-scans for hepatic surgery. In *Medical Imaging*, SPIE proceedings, pages 246–255.

[134] Soler, L., Delingette, H., Malandain, G., Montagnat, J., Ayache, N., Koehl, C., Dourthe, O., Malassagne, B., Smith, M., Mutter, D., and Marescaux, J. (2001). Fully automatic anatomical, pathological, and functional segmentation from CT scans for hepatic surgery. *Computer Aided Surgery*, 6(3):131–142.

[135] Steger, C. (1998). An unbiased detector of curvelinear structures. *IEEE Trans. Pattern Anal. Mach. Intell.*, 20(2):113–125.

[136] Swift, R. D., Kiraly, A. P., Sherbondy, A. J., Austin, A. L., Hoffman, E. A., McLennan, G., and Higgins, W. E. (2002). Automatic axis generation for virtual bronchoscopic assessment of major airway obstructions. *Comput. Med. Imaging Graphics*, 26(2):103–118.

[137] Szymczak, A. (2008). Vessel tracking by connecting the dots. *The Midas Journal.*

[138] Szymczak, A., Stillman, A., Tannenbaum, A., and Mischaikow, K. (2006). Coronary vessel trees from 3d imagery: A topological approach. *Medical Image Analysis*, 10(4):548–559.

[139] Tang, C.-K., Medioni, G., and Lee, M.-S. (2001). N-dimensional tensor voting and application to epipolar geometry estimation. *IEEE Trans. Pattern Anal. Mach. Intell.*, 23(8):829–844.

[140] Tankyevych, O., Talbot, H., and Dokladal, P. (2008). Curvilinear morpho-hessian filter. In *Proc. IEEE Int. Symp. Biomed. Imaging*, pages 1011–1014.

[141] Tek, H., Comaniciu, D., and Williams, J. (2001). Vessel detection by mean-shift based ray propagation. In *Proc. IEEE Math. Meth. Biomed. Image Anal.*, pages 228–235.

[142] Tek, H., Gulsun, M. A., Laguitton, S., Grady, L., Lesage, D., and Funka-Lea, G. (2008). Automatic coronary tree modeling. *The Midas Journal*.

[143] ter HaarRomeny, B. (2003). *Front-End Vision and Multi-Scale Image Analysis: Multi-scale Computer Vision Theory and Applications, Written in Mathematica*. Kluwer.

[144] Toledo, R., Orriols, X., Binefa, X., Radeva, P., Vitria, J., and Villanueva, J. (2000a). Tracking elongated structures using statistical snakes. In *Proc. IEEE Int. Conf. Pattern Recognit.*, pages 157–162.

[145] Toledo, R., Orriols, X., Radeva, P., Binefa, X., Vitria, J., Morales, C., and Villanueva, J. (2000b). Eigensnakes for vessel segmentation in angiograph. In *Proc. IEEE Int. Conf. Pattern Recognit.*, pages 340–343.

[146] Tschirren, J., McLennan, G., Palágyi, K., Hoffman, E. A., and Sonka, M. (2005). Matching and anatomical labeling of human airway tree. *IEEE Trans. Med. Imag.*, 24(12):1540–1547.

[147] Tschirren, J., Yavarna, T., and Reinhardt, J. M. (2009). Airway segmentation framework for clinical environments. In *International Workshop on Pulmonary Image Analysis*, Medical Image Computing and Computer Assisted Intervention, pages 227–238.

[148] Tyrrell, J. A., di Tomaso, E., Juja, D., Tong, R., Kozak, K., Jain, R. K., and Roysam, B. (2007). Robust 3-d modeling of vasculature imagery using superellipsoide. *IEEE Trans. Med. Imag.*, 26(2):223–237.

[149] Udupa, J., Saha, P., and Lotufo, R. (2002). Relative fuzzy connectedness and object definition: theory, algorithms, and applications in image segmentation. *IEEE Trans. Pattern Anal. Mach. Intell.*, 24(11):1485–1500.

[150] van Bemmel, C., Wink, O., Verdonck, B., Viergever, M., and Niessen, W. (2003a). Blood pool contrast-enhanced MRA: improved arterial visualization in the steady state. *IEEE Trans. Med. Imaging*, 22(5):645–652.

[151] van Bemmel, C., Wink, O., Verdonck, B., Viergewer, M., and Niessen, W. (2003b). Blood pool contrast-enhanced MRA: improved arterial visualization in the steady state. *IEEE Trans. Med. Imag.*, 22(5):645–652.

[152] van Bemmel, C. M., Spreeuwers, L. J., Viergever, M. A., and Niessen, W. J. (2003c). Level-set-based artery-vein separation in blood pool agent cr-mr angiograms. *IEEE Trans. Med. Imag.*, 22(10):1124–1234.

[153] van Ginneken, B., Baggerman, W., and van Rikxoort, E. M. (2008). Robust segmentation and anatomical labeling of the airway tree from thoracic CT scans. In *Proc. of MICCAI*, pages 219–226, New York, USA.

[154] van Rikxoort, E. M., Baggerman, W., and van Ginneken, B. (2009). Automatic segmentation of the airway tree from thoracic ct scans using a multi-threshold approach. In *International Workshop on Pulmonary Image Analysis*, Medical Image Computing and Computer Assisted Intervention, pages 341–349.

[155] Vasilevskiy, A. and Siddiqi, K. (2002). Flux maximizing geometric flows. *IEEE Trans. Pattern Anal. Mach. Intell.*, 24(12):1565–1578.

[156] Wan, S., Ritman, E., and Higgins, W. (2002). Multi-generational analysis and visualization of the vascular tree in 3D micro-CT images. *Comput. Biol. Med.*, 32(2):55–71.

[157] Wang, C. and Smedby, O. (2008). An automatic seeding method for coronary artery segmentation and skeletonization in CTA. *The Midas Journal.*

[158] Weinheimer, O., Achenbach, T., and Düber, C. (2009). Fully automated extraction of airways from CT scans based on self-adapting region growing. In *International Workshop on Pulmonary Image Analysis*, Medical Image Computing and Computer Assisted Intervention, pages 315–321.

[159] Wesarg, S. and Firle, E. (2004). Segmentation of vessels: the corkscrew algorithm. In *Proc. SPIE Med. Imaging*, pages 1609–1620.

[160] Wiemker, R., Bülow, T., and Lorenz, C. (2009). A simple centricity-based region growing algorithm for the extraction of airways. In *International Workshop on Pulmonary Image Analysis*, Medical Image Computing and Computer Assisted Intervention, pages 309–314.

[161] Wilson, D. and Noble, J. (1999). An adaptive segmentation algorithm for time-of-flight MRA data. *IEEE Trans. Med. Imaging*, 18(10):938–945.

[162] Wink, O., Niessen, W., and Viergever, M. (2000). Fast delineation and visualization of vessels in 3-d angiographic images. *IEEE Trans. Med. Imag.*, 19(4):337–346.

[163] Wink, O., Niessen, W., and Viergever, M. (2004). Multiscale vessel tracking. *IEEE Trans. Med. Imag.*, 23(1):130–133.

[164] Wong, W., Chung, A., and Yu, S. (2004). Local orientation smoothness prior for vascular segmentation of angiography. In *Proc. Eur. Conf. Comput. Vision*, pages 353–365.

[165] Wong, W. C. K. and Chung, A. C. S. (2006). Augmented vessels for quantitative analysis of vascular abnomalities and endovascular treatment planning. *IEEE Trans. Med. Imag.*, 25(6):665–684.

[166] Wörz, S. and Rohr, K. (2008). Cramér-Rao bounds for estimating the position and width of 3d tubular structures and analysis of thin structures with application to vascular images. *J. Math. Imaging Vision*, 30:167–180.

[167] Wu, C., Agam, G., Roy, A., and III, S. (2004). Regulated morphology approach to fuzzy shape analysis with application to blood vessel extraction in thoracic ct scans. In *Proc. SPIE Med. Imaging*, pages 1262–1270.

[168] Xu, C. and Prince, J. L. (1998). Snakes, shapes, and gradient vector flow. *IEEE Trans. on Image Processing*, 7(3):359–369.

[169] Yan, P. and Kassim, A. (2005). MRA image segmentation with capillary active contour. In *Proc. Med. Image Comput. Assist. Interv.*, pages 51–58.

[170] Yang, Y., Tannenbaum, A., and Giddens, D. (2004). Knowledge-based 3D segmentation and reconstruction of coronary arteries using CT images. In *Proc. IEEE Eng. Med. Biol. Soc.*, pages 1664–1666.

[171] Yi, J. and Ra, J. B. (2003). A locally adaptive region growing algorithm for vascular segmentation. *International Journal of Imaging Systems and Technology*, 13(4):208–215.

[172] Yim, P., Cebral, J., Mullick, R., Marcos, H., and Choyke, P. (2001). Vessel surface reconstruction with a tubular deformable model. *IEEE Trans. Med. Imag.*, 20(12):1411–1421.

[173] Yim, P., Kayton, M., Miller, W., Libutti, S., and Choyke, P. (2003). Automated detection of blood vessels using dynamic programming. *Pattern Recognit. Lett.*, 24(14):2471–2478.

[174] Yu, Z., Bajaj, C., and Bajaj, R. (2002). Normalized gradient vector diffusion and image segmentation. In *Proc. of ECCV*, pages 17–530.

[175] Zahlten, C., Jürgens, H., and Peitgen, H. (1995). Reconstruction of branching blood vessels from CT-data. *Visualization in Scientific Computing, Springer-Verlag Wien*, pages 41–52.

[176] Zambal, S., Hladuvka, J., Kanitsar, A., and Buhler, K. (2008). Shape and appearance models for automatic coronary artery tracking. *The Midas Journal*.

[177] Zhang, Y., Chen, K., and Wong, S. T. (2008). 3D interactive centerline extraction. *The Midas Journal*.